Eidgenössische Technische Hochschule Zürich
Swiss Federal Institute of Technology Zurich

Master's Thesis

Randomized Benchmarking of Two-Qubit Gates

Department of Physics
Laboratory for Solid State Physics
Quantum Device Lab

August 28, 2015

Author:
Samuel Haberthür

Supervisor:
Yves Salathé

Principal Investor:
Prof. Dr. Andreas Wallraff

Abstract

On the way to high-fidelity quantum gates, accurate estimation of the gate errors is essential. Randomized benchmarking (RB) provides a tool to classify and characterize the errors of multi-qubit gates. Here we implement RB to investigate the fidelity of single-qubit and two-qubit gates in the Clifford group realized on a superconducting transmon qubit system. This thesis provides an overview of the current randomized benchmarking methods and gives detailed discussions of how to estimate the gate error. For single-qubit gates an average gate fidelity of 99.6(1) % was obtained. Furthermore, it shows how two-qubit gates are realized and how they can be calibrated to achieve high fidelities. Here, the focus lies on the controlled phase gate and iSWAP gate, which are both implemented using fast magnetic flux pulses. For the former, fidelities above 92 % were estimated. Also a decreasing of average gate fidelity over time was observed. Finally, a method for achieving scalable iSwap gates is proposed.

Contents

1. Motivation

Alain Turing made a general model of classical computing in 1937 which was later called Turing machine [1]. A few years later the first computers based on electrical components were built. During the following years, the power of computers grew with a remarkable speed, whereas the space they use shrank. Amazed by this developments, Gordon Moore stated in 1965, exactly 28 years after Alain Turing had published his fiding that the amount of gates engineers can pack on integrated circuits grows exponentially [2]. Astonishingly, this statement, better known as *Moore's law*, still holds today. But when does it end? Our computer circuits today are already so small that we run up against quantum effects in fabrication. Therefore, with this technology we will not be able to hold Moore's law any longer in the next few decades. The only way is to investigate new computer models, such as quantum computers, where we make use of the quantum mechanisms instead of avoiding them [3].

What advantages does quantum computing have in comparison to classical computing? On one hand, certain tasks, easily accomplished in classical information theory, are not possible with quantum systems. Cloning, for example, a simple task for a modern computer, is not achievable in quantum mechanics [4]. Another drawback is the probabilistic nature of quantum processes. Quantum mechanics deals with probabilities and even if the error is negligible small, the unwanted case might still occur. But on the other hand, a quantum computer is capable to efficiently solve problems, which do not have a known efficient solution on a classical computer. The term *efficient* has a mathematical description in computational complexity, used to classify algorithms, where an algorithm which solves a problem in a time polynomial to its size is called efficient. In 1994, Peter Shor came up with two quantum algorithms solving the important problem of finding prime factors of big integer numbers and the discrete logarithm problem efficiently [5]. Therefore, it would be possible to break most cryptosystems used today, like the RSA cryptosystem. Another example is Lov Grover's search algorithm established in 1996 [6], which significantly speeds up searching objects in an unstructured space. In all of these cases, a quantum computer is more powerful than a classical computer. By today, only a few such quantum algorithms are known and there might be many more. Finding new algorithms for quantum computers that are faster than their classical counterpart, is one of the challenging tasks for the future.

However, in order to make use of such advantageous algorithms, it is necessary to coherently control large amounts of qubits and conduct many computational gates on them. Any quantum system capable of fulfilling these conditions is called *scalable*. One of the problems on our way to scalability is the loss of coherence, meaning the loss of information about the qubit state, providing an upper limit of the time window for operations. Furthermore, as mentioned above, working with a quantum system never leads to results with 100% certainty. But, due to quantum error-correction methods, developed to preserve quantum information in the presence of noise, quantum computation becomes fault tolerant. Yet, the probability of errors per unitary gate should still be well below the threshold of 10^{-2} [7]. The current goal is to reach error probabilities of below 10^{-4}.

While heading towards scalable quantum gates, it is of great importance to have methods able to identify low error probabilities of quantum operations implemented on a quantum system. A well known protocol, capable of fully characterizing any quantum process including the noise, is *quantum process tomography* (QPT) [8]. It has been successfully used on different qubit systems based on nuclear magnetic resonance (NMR) [9], linear optics [10], atomic ions [11] and superconducting circuits [12]. Unfortunately, QPT suffers from two major drawbacks. First, it is not scalable, since the number of required experiments grows exponentially with the number of qubits, which makes it unattractive for large-scale quantum processes. Secondly, QPT is sensitive to state preparation and measurement (SPAM) errors and therefore inappropriate to estimate the specific error of a quantum operation. Another method, recently developed, is *randomized benchmarking* (RB) [13–16]. RB provides a scalable and robust method for verifying gate errors, insensitive to SPAM errors. However, in contrast to QPT, it does not provide a complete description of a quantum process, which may be desirable in some cases. Since the first RB protocol was published in 2008 [13], many different versions and extensions [17–20] came up, all trying to further characterize the occuring gate errors.

The aim of the present thesis is to implement a randomized benchmarking method for one and two-qubit gates and to estimate the errors of gates calibrated in our lab. Besides the single-qubit gates, the focus lies on the two-qubit *controlled phase* and *i*SWAP gate, whose realization and calibration will be discussed in detail. Overall, this thesis is segmented in three parts, providing a full theoretical approach to the used methods, as well as a careful documentation of the experimental results. The following chapter includes the theoretical concept of superconducting quantum circuits and their realization in our lab. This is followed by a chapter about randomized benchmarking methods for single-qubit gates. Finally, the last chapter demonstrates the expansion of the methods to two-qubit gates.

2. Superconducting Quantum Circuits

This chapter provides an introduction into the basic principles and methods used in single qubit quantum computation today. In order to understand how the qubits used during this thesis work, the first two sections give a brief theoretical overview. It starts with the very basic oscillator circuits and continues until the most up to date qubit design, the *transmon*. Section 2.3 and 2.4 explain what happens when the qubit is connected to a resonator and why this is useful. At the end, we will give more specific details about the experimental setup (Section 2.6).

2.1. Electromagnetic Oscillators

One of the simplest electrical circuits, consisting solely of a inductor with inductance L and a capacitor with capacitance C, but no resistor, is the LC *oscillator* circuit (Figure 2.1). Its Lagrangian energy is completely described in terms of the time-dependent magnetic flux threading the coil [21]

$$\Phi(t) = \int_0^t V(\tau)\mathrm{d}\tau, \tag{2.1}$$

where $V(t) = \dot{\Phi}(t)$ is the voltage across the inductor element assuming $V(0) = 0$. Therefore, the energy saved in the capacitor represents the kinetic energy of the system, whereas the potential energy is stored in the inductor:

$$E_{kin} = \frac{1}{2}CV^2 = \frac{1}{2}C\dot{\Phi}^2 \qquad\qquad E_{pot} = \frac{1}{2}LI^2 = \frac{1}{2L}\Phi^2. \tag{2.2}$$

Both terms together lead to a Lagrangian given by

$$\mathcal{L} = \frac{1}{2}C\dot{\Phi}^2 - \frac{1}{2L}\Phi^2. \tag{2.3}$$

To receive the Hamiltonian describing the system, the conjugate momentum has to be calculated:

$$\frac{\delta L}{\delta \dot{\Phi}} = C\dot{\Phi} = CV = Q \tag{2.4}$$

We see that in this representation the conjugate momentum of the flux coordinate is just the charge Q stored in the capacitor. Using the Legendre transformation

$$\mathcal{H} = \dot{q}p - \mathcal{L}(q, \dot{q}; t), \tag{2.5}$$

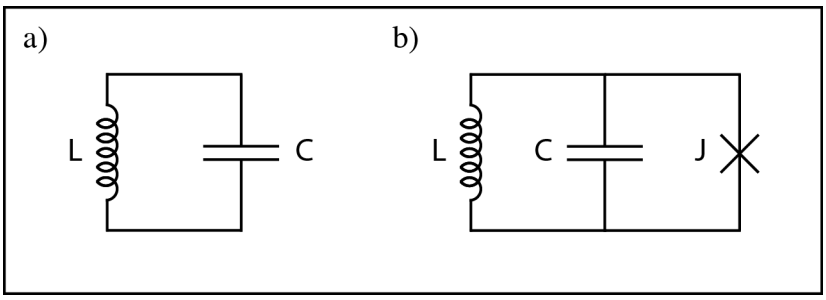

Figure 2.1.: Schematic circuit diagrams of basic oscillator loops. **(a)** LC Oscillator circuit consisting of a inductor with inductance L and a capacitor with capacitance C. **(b)** The circuit of an rf-SQUID loop is basically a LC oscillator circuit with an additional Josephson Junction connected in parallel.

where the generalized position and momentum are given by $q = \Phi$ and $p = Q$ respectively, leads us to a Hamiltonian

$$\mathcal{H}(Q, \Phi) = \frac{Q^2}{2C} + \frac{\Phi^2}{2L}, \tag{2.6}$$

which is the Hamiltonian of a harmonic oscillator. In this sense, the dynamics of the LC circuit can be seen as the harmonic movement of charged particles in-between the capacitor and the coil.

An expansion of the LC oscillator is the circuit shown in Figure 2.1(b). It is called *rf-SQUID* or radio frequency superconducting quantum interference device and is similar the *dc-SQUID* (direct current). Both are based on a superconducting loop containing Josephson junctions. The dynamics in such circuits can be described by the superconducting phase difference ϕ in the Josephson junction, which is often simply referred to as the *superconducting phase*. By the well-known relation

$$\phi = \frac{2e}{\hbar} \int_0^t V(\tau)\,\mathrm{d}\tau = \frac{2e}{\hbar}\Phi, \tag{2.7}$$

the superconducting phase is directly connected to the magnetic flux through the coil and the voltage drop across the junction. In terms of the superconducting phase, the potential energy stored in the Josephson junction is given by

$$\begin{aligned} E_{pot} &= \int_0^t I\,V(\tau)\,\mathrm{d}\tau \\ &= \int_0^t I_J\,sin(\phi)\,\dot{\Phi}\,\mathrm{d}\tau \\ &= \frac{\hbar}{2e}\int_0^\phi I_J\,sin(\phi)\dot{\phi}\,\mathrm{d}\tau \\ &= \frac{\hbar}{2e}\int_0^\phi I_J\,sin(\phi)\,\mathrm{d}\phi = \frac{\hbar}{2e}\,I_J\,(1 - cos\phi), \end{aligned} \tag{2.8}$$

where we have used the first Josephson relation [22], according to which the current I flowing through the junction is equal to $I_J\, sin\phi$ when I_J denotes the critical Josephson current. As in the preceding paragraph, the Lagrangian is given by the kinetic energy term Eq. 2.2 minus the potential ones Eq. 2.2 and 2.8,

$$\mathcal{L}(\phi) = \frac{\hbar^2}{4\,E_C}\dot{\phi}^2 - \frac{E_L}{2}\phi^2 - E_J\,(1 - cos\phi), \tag{2.9}$$

where $E_C = \frac{(2e)^2}{2C}$ is the charging energy of the capacitor charged with one electron pair, called *Cooper pair*, $E_L = \frac{\hbar^2}{4e^2\,L}$ the energy of the persistent current in the loop and $E_J = \frac{\hbar}{2e}I_J$ the Josephson energy denoting the energy stored in the Josephson junction. As in the harmonic case, the conjugate momentum is given in terms of the charge on the capacitor, but with the small difference that here it represents the number of Cooper pairs n on the capacitor,

$$\frac{\delta\mathcal{L}}{\delta\dot{\phi}} = \frac{\hbar^2}{2E_C}\dot{\phi} = \frac{\hbar^2}{4e^2}C\dot{\phi} = \frac{\hbar}{2e}CV = \hbar n, \tag{2.10}$$

since $CV = 2ne$. Thus, the Hamiltonian describing the rf-SQUID in terms of n and ϕ is

$$\mathcal{H}(n,\phi) = E_C\,n^2 + \frac{1}{2}E_L\,\phi^2 + E_J\,(1 - cos\phi). \tag{2.11}$$

Now clearly visible after a comparison with Eq. 2.6, the additional Josephson junction in the circuit changes the harmonic LC oscillator to a non-linear oscillator.

The question is now, how can these systems be used to build a qubit? In the interest of conducting operations, a qubit requires two clearly separable levels, 0 and 1. So far, the energy spectrum of our circuits is continuous, but after a quantization of the electromagnetic field, the energy spectrum splits up in specific energy levels serving as possible 0 and 1 states. Therefore, the classical variables are replaced with their corresponding operators $\hat{n}$ and $\hat{\phi}$, fulfilling the commutation relation

$$[\hat{n}, \hat{\phi}] = -i \tag{2.12}$$

Another, yet unanswered, question is the need for a non-linear Hamiltonian. A desirable property of two computational states is that the transition frequency between the 0 and the 1 state should not be in resonance with another transition frequency, in order to avoid unwanted transitions. Therefore, a non-equidistant energy spectrum is necessary. Moreover, the states should be well decoupled from the environment. As a consequence, one commonly chooses a low lying pair of levels, like the ground $|g\rangle$ and first excited state $|e\rangle$. The *anharmonicity* α, defined by the energy difference between transition from the ground to the first excited state ω_{ge} and the transition from the first to the second excited state ω_{ef}, gives a measure of non-linearity of the qubit energy spectrum.

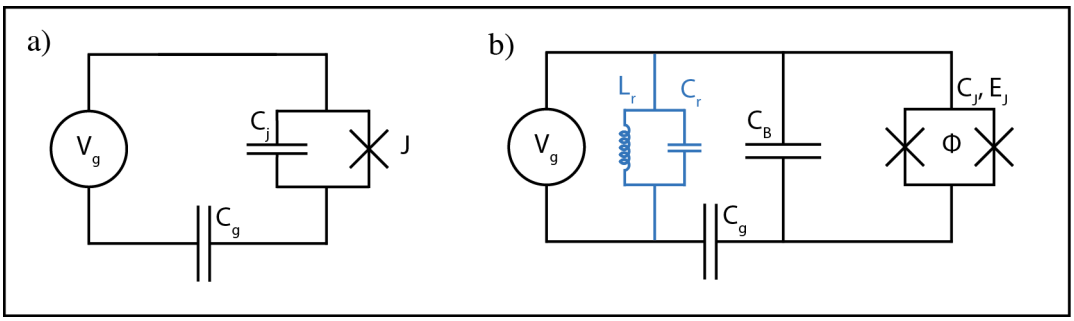

Figure 2.2.: Circuit diagrams of the Cooper pair box and the transmon qubit. **(a)** The CPB consists of an external gate voltage V_g which is connected to a superconducting island via the two capacitors C_g and C_j and the Josephson junction J. **(b)** Introducing a large shunt capacitance C_B brings us to the transmon design. The additional circuit in the middle (blue) shows the case when the transmon is connected to a harmonic resonator.

2.2. The Transmon Qubit

Over the last 20 years many qubit designs have been established based on the Josephson junction. Due to the different physical spectra used, they can be classified into charge, flux or phase qubits [21]. The first developed qubit system, the charge qubit or also called *Cooper Pair Box* (CPB) [23], is topologically distinct from the basic rf-SQUID circuit in the sense that in contains a superconducting island (Figure 2.2(a)). It is based on the number of Cooper pairs on the island, which is an integer number since the Josephson junction acts as a tunnel barrier, where only Josephson tunneling is allowed. If tunneling were forbidden, the Cooper pairs would be trapped on the island and n remains constant. Qubits belonging to the flux qubit class have computational states which are defined by the direction of current circulating in the loop, clockwise or counter-clockwise. One of the first flux qubit designs was made by Mooij et al. in 1999 [24]. Finally, the phase qubit, like its name says, uses the energy levels defined by the superconducting phase difference of the Josephson junction. It was first established in 2002 by Martinis et al. [25]. Of these three qubit designs, the charge qubit is the most used qubit type today and was also used in this thesis. Hence, we will discuss it in more detail.

The Hamiltonian of the CPB is similar to the one of the rf-SQUID given in Equation 2.11:

$$\hat{H} = E_C \left(\hat{n} - n_g\right)^2 - E_J \cos\hat{\phi} \tag{2.13}$$

Due to the gate voltage V_g, we have an additional means of external control of the qubit. Therefore, it is possible to set a bias charge on the gate capacitor $n_g = \frac{C_g V_g}{2e}$ expressed in terms of Cooper pairs. Moreover, since there is a gate capacitor involved, the charging energy constant is given by $E_C = \frac{(2e)^2}{2C_\Sigma}$, where $C_\Sigma = C_j + C_g$. For simplicity, the Hamiltonian can also

be represented in the Cooper pair number basis, that is $\hat{n}\,|n\rangle = n\,|n\rangle$ [23],

$$\hat{H} = \sum_N \left[E_C(n - n_g)^2\,|n\rangle\,\langle n| - \frac{E_J}{2}(|n\rangle\,\langle n+1| + |n+1\rangle\,\langle n|) \right] \tag{2.14}$$

This representation visualizes the fact that the number of Cooper pairs can only be changed by the last term, the Josephson coupling term. The energy eigenvalues of the CPB Hamiltonian are exactly determined in terms of Mathieu functions [26]

$$E_m(n_g) = E_C\, a_{2(n_g + k(m,n_g))}(-\frac{E_J}{2\,E_C}), \tag{2.15}$$

where $a_r(q)$ is Mathieu's characteristic value and $k(m, n_g)$ a function that sorts the eigenvalues correctly [27]. In Figure 2.3, the lowest three energy levels are plotted as a function of the bias Cooper pair number. The dashed lines correspond to the case without Josephson term or $E_J = 0$, the solid lines to the case $E_J/E_C = 1$. In this sense, the Josephson term lifts the degeneracy at the crossing about E_J. Usually, the CPB is operated at $n_g = 1/2$ also called charge *sweet spot*, in the interest of eliminating linear noise sensitivity. Thus, increasing the dephasing time T_2, which is the time until all information about the phase of the qubit is lost. However, just operating the qubit at the charge sweet spot is not enough. Even though, the sensitivity to linear charge noise can be successfully decreased, the system is still sensitive to $1/f$ noise. A way to further lower the sensitivity is to decrease the so called *charge dispersion* ϵ_m, which denotes the peak-to-peak value of an energy level:

$$\epsilon_m = E_m(n_g = 1/2) - E_m(n_g = 0) \tag{2.16}$$

This value depends on the ratio E_J/E_C. The higher the ratio between the Josephson energy and the charge energy, the smaller ϵ_m and the flatter the dependence on n_g. But the price we pay for decreasing the charge dispersion is an unwanted lowering of the anharmonicity.

A solution is given by a new design, established by Koch et al in 2007 [27] and called the transmission-line shunted plasma oscillation (*transmon*) qubit. Its design is shown schematically in Figure 2.2. Compared to the CPB circuit, the transmon consists of two Josephson junctions in a loop, allowing an external magnetic flux to induce an electrical current. With this new control parameter it is possible to periodically vary the Josephson energy according to [27]

$$E_J = E_{J,max} \left| cos(\frac{\pi\Phi}{\Phi_0}) \right|, \tag{2.17}$$

where $\Phi_0 = \hbar/2e$ denotes the superconducting flux quantum constant. Furthermore, what makes the transmon special is the property that by increasing the ratio E_J/E_C the charge dispersion decreases exponentially where in the same time, the anharmonicity reduces algebraically [27]. In that matter, the qubit can be operated at an E_J/E_C ratio much larger than the CPB. In

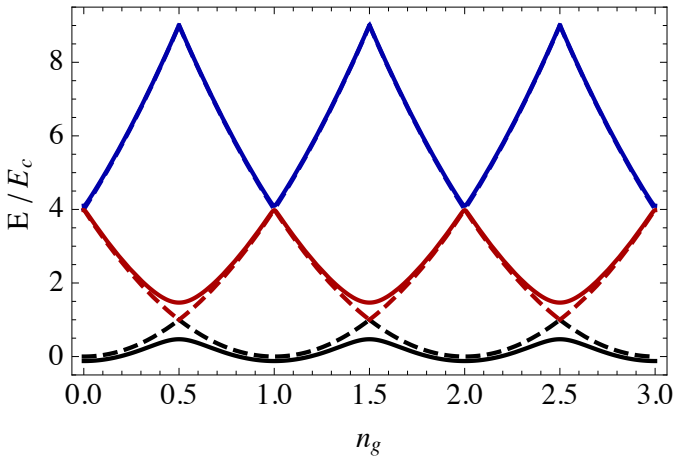

Figure 2.3.: The first three energy levels of the Cooper Pair Box (black, red and blue) as a function of gate bias voltage. The ratio between Josephson energy E_J and charging energy E_C is 1 (solid lines). In contrast to the harmonic case (dashed lines), where the Josephson energy is zero, the energy levels are non-degenerate.

Figure 2.4 the energy levels are plotted for the ratios $E_J/E_C = 5$ and $E_J/E_C = 50$. At this point the qubit is stable against charge fluctuations, even though we have lost a parameter to control the qubit.

Beside a few additional elements, the circuit of the transmon is similar to the CPB and so the Hamiltonian Eq. 2.13 still holds. The only difference is that the total capacitance has changed to $C_\Sigma = C_J + C_B + C_g$, yielding to a smaller charging energy E_C, which, on the other hand, gives the desired higher E_J/E_C ratio.

2.3. Circuit QED

Even a qubit with very high anharmonicity and charge insensitivity is useless, when it cannot be controlled. Controlled in the sense that there is a possibility to conduct quantum operations and state read-outs. A way to influence and read the states of a qubit is to couple the qubit to an LC oscillator as shown in Figure 2.2 (blue). This so called *circuit QED* setup is similar to cavity QED, where an atom, forming a dipole, is coupled to light in an optical cavity. In 2004 Blais et al. [28] proposed the idea to implement the principle with superconducting circuits replacing the atom and a coplanar waveguide resonator acting as microwave cavity. In the same year, Wallraff et al. [29] first realized it on a chip.

A necessary condition for a successful coupling is that the dipole coupling strength between qubit and resonator is strong enough for an energy exchange. In this regard, the transmon

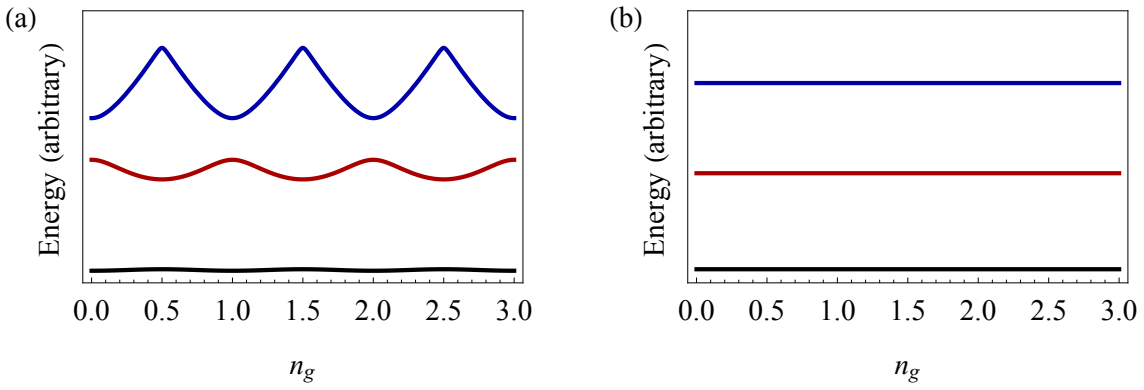

Figure 2.4.: First three energy levels of the CPB/transmon qubit with ratios $E_J/E_C = 5$ **(a)** and $E_J/E_C = 50$ **(b)** as a function of the gate bias voltage. Clearly visible, the transmon becomes change insensitive for a higher ratio of Josephson energy to charging energy.

qubit reveals another remarkable property when coupled to a superconducting transmission line resonator, since the coupling strength increases in a power-law with the ratio E_J/E_C [27]. As shown in Section 2.1, the resonator in form of an LC oscillator is described by a harmonic oscillator. For simplification, we assume that the resonator has only a single mode with resonance frequency ω_r, and that the qubit does not strongly perturb the resonator. Furthermore, assume that this frequency ω_r is solely determined by its geometric and dielectric properties [30]. By quantizing the harmonic Hamiltonian Eq. 2.6, the resonator system is described by

$$\hat{H}_r = \hbar\omega_r \hat{a}^\dagger \hat{a} \tag{2.18}$$

In this representation, the annihilation $\hat{a}$ and creation operator $\hat{a}^\dagger$ define the elimination and creation of a single photon in the resonator. Similar to cavity QED, the Hamiltonian of the whole system is given by the generalized *Jaynes-Cummings* Hamiltonian [27]

$$\hat{H} = \hbar \sum_j \omega_j \left|j\right\rangle \left\langle j\right| + \hbar\omega_r \hat{a}^\dagger \hat{a} + \hbar \sum_{i,j} g_{i,j} \left|i\right\rangle \left\langle j\right| (\hat{a} + \hat{a}^\dagger) \tag{2.19}$$

where $\hbar g_{i,j}$ represents the coupling strength of the atomic transition from level $|i\rangle$ to level $|j\rangle$ to the electric field in the cavity. In our system we can neglect simultaneous excitation of transmon and resonator by using a rotating-wave approximation [13], which leads to the effective Hamiltonian

$$\hat{H}_{eff} = \hbar \sum_j \omega_j \left|j\right\rangle \left\langle j\right| + \hbar\omega_r \hat{a}^\dagger \hat{a} + \hbar \sum_i \left[g_{i,i+1} \left|i\right\rangle \left\langle i+1\right| \hat{a}^\dagger + g_{i+1,i} \left|i+1\right\rangle \left\langle i\right| \hat{a} \right] \tag{2.20}$$

Here, we are most interested in the case where the qubit system is restricted to a two-state Hamiltonian, which gives us the usual Jaynes-Cummings form [21]

$$\hat{H} = \hbar \frac{\omega_q}{2} \sigma^z + \hbar\omega_r \hat{a}^\dagger \hat{a} + \hbar g_{ge} \left[\hat{a}\sigma^+ + \hat{a}^\dagger \sigma^- \right] \tag{2.21}$$

In contrast to the general form Eq. 2.20, the reduced Hamiltonian is analytically solvable and has the eigenvalues [31, 32]

$$E_0^{\pm} = -\hbar\frac{\omega_q}{2}, \qquad E_{n>0}^{\pm} = \hbar\omega_r\left(n+\frac{1}{2}\right) \pm \frac{\hbar}{2}\sqrt{\Delta^2 + 4g_{ge}^2(n+1)}, \tag{2.22}$$

with $\Delta = \omega_q - \omega_r$ being the difference between the qubit transition frequency and the resonance frequency of the resonator and $n = \langle \hat{a}^\dagger \hat{a} \rangle$ being the number of photons in the resonator. The generally entangled energy states of the qubit/resonator system are given by the ground state $|g, 0\rangle$ and

$$\begin{aligned} |+, n\rangle &= \cos(\frac{\theta_n}{2})\,|e, n\rangle + i\sin(\frac{\theta_n}{2})\,|g, n+1\rangle\,, \\ |-, n\rangle &= \sin(\frac{\theta_n}{2})\,|e, n\rangle - i\cos(\frac{\theta_n}{2})\,|g, n+1\rangle\,, \end{aligned} \tag{2.23}$$

which are called *dressed states*, are slightly shifted in comparison to the energy states of the two systems alone. Here, $\tan(\theta_n) = 2g_{ge}\sqrt{n+1}/\Delta$. Usually, one differentiates between two main cases in the proportion of the qubit and resonator frequency Δ, the *resonant limit* $\Delta \to 0$ and the *dispersive limit* $\Delta \gg g$. In the resonant limit, where the resonator and qubit frequency are tuned in resonance, the coupling of the two systems results in an avoided crossing with a minimum distance of $2\hbar g_{ge}\sqrt{n+1}$. This separation relates to a coherent exchange of single energy quanta between qubit and resonator leading to *Rabi Oscillations*. In the dispersive limit, where the two systems are almost uncoupled, the dressed states have only a small frequency shift of χ compared to the uncoupled states. This *dispersive shift* depends on the photon population in the resonator. If the resonator is empty, the effect arises from the qubit coupling with vacuum fluctuations, which is called Lamb shift $\delta_L \approx g_{ge}^2/\Delta$ [33,34]. In the other case, when the resonator is populated with n photons, the shift is caused by the Lamb shift and an additional ac Stark shift $\delta_S \approx 2ng_{ge}^2/\Delta$. Since the eigenstates in the dispersive limit are almost encoupled, there is no direct exchange of energy between qubit and resonator, thus direct coupling terms in Eq. 2.21 can be neglected. After eliminating off-diagonal terms up to second order in g/Δ by a unitary transformation the Hamiltonian takes the final form [27]

$$\hat{H}_{disp} = \frac{\hbar}{2}(\omega_q + \chi)\sigma^z + \hbar\omega_r\hat{a}^\dagger\hat{a} + \hbar\chi\hat{a}^\dagger\hat{a}\sigma^z, \tag{2.24}$$

where $\chi = g_{ge}^2/\Delta$ is called *dispersive shift*.

2.4. Readout and Single Quantum Gates

As demonstrated by Wallraff et al. [29], coherent control and readout of a CPB qubit is accomplished by moving to the dispersive limit. The so called *dispersive readout* allows a non-demolition measurement of the qubit state, because the frequency of the resonator is shifted by

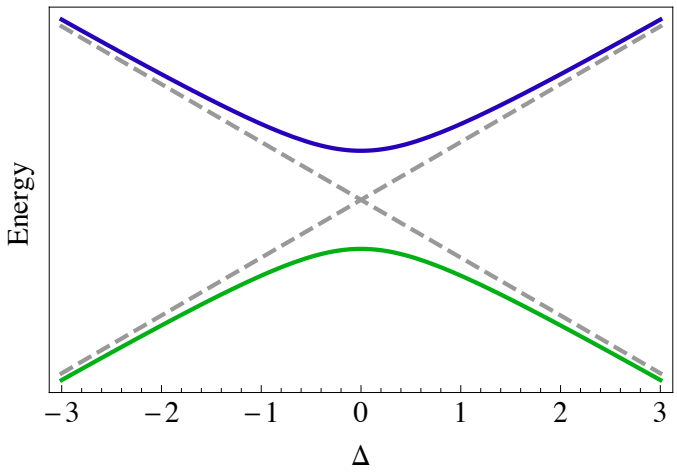

Figure 2.5.: Energy levels of a transmon qubit coupled to a resonator (solid lines) in comparison to the uncoupled system (dashed, grey). The x axis shows the dependency on the qubit-resonator detuning. A coupling in the resonant limit $\Delta \to 0$ leads to an energy splitting of $2\hbar g_{ge}\sqrt{n+1}$. Even in the off-resonant dispersive limit $\Delta \gg g$, a small deviation of χ from the uncoupled states is observable.

the qubit state-dependent dispersive shift. In order to make use of this property, a weak microwave measurement tone is switched on at the input port of the resonator. The Hamiltonian of the drive is given by [35]

$$H_D = \epsilon(t)\hat{a}^\dagger e^{-i\omega_d t} + \epsilon^*(t)\hat{a}e^{i\omega_d t} \tag{2.25}$$

where we have three variables to change the tone, the time-dependent amplitude $\epsilon(t)$, the frequency ω_d and the phase. According to Figure 2.6, which shows the dispersive shift of the resonator frequency in terms of the transmitted amplitude, a measurement frequency of $\omega_d = \omega_r - \chi$ will lead to a measured signal of an on-resonantly driven resonator without any phase shift when the qubit is in ground state. In the case, when the qubit is in the excited state, the transmitted phase is damped and the phase shifted.

The qubit drive can be used to perform single qubit quantum gates by sending strong microwave pulses into the resonator. Here, single quantum gates correspond to rotations on the Bloch sphere. In contrast to the measurement drive, which is switched on for a longer period of time (in our lab for 15 µs), the gate pulse is rather short (21 ns) and its frequency is on resonance with the qubit frequency ω_q. By adding the drive Hamiltonian Eq. 2.25 and moving into a frame rotating at the drive frequency ω_d, the Hamiltonian Eq. 2.24 is extended to [35]

$$\hat{H}_{disp} = \frac{\hbar}{2}(\omega_q + \chi - \omega_d)\sigma^z + \hbar(\omega_r + \chi\sigma^z - \omega_d)\hat{a}^\dagger\hat{a} + \frac{\Omega_R}{2}(\cos(\phi)\sigma^x + \sin(\phi)\sigma^y). \tag{2.26}$$

The term $\Omega = 2\epsilon g/(\omega_r - \omega_d)$, which is called Rabi frequency, represents the frequency with which the qubit oscillates between the ground and excited state. Thus, depending on the phase ϕ a

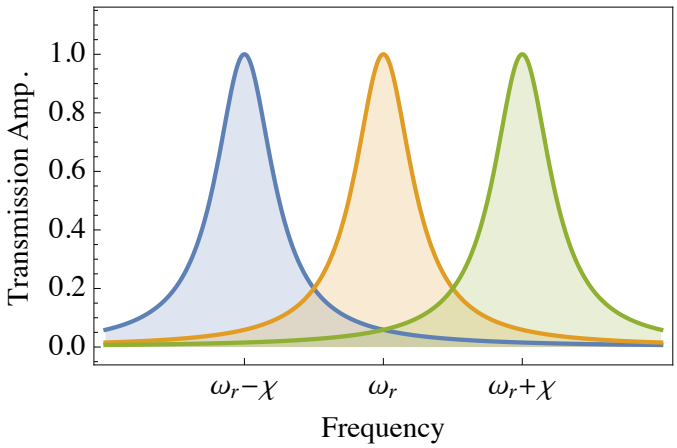

Figure 2.6.: Transmitted amplitude on the output port of a resonator for a uncoupled resonator (middle, orange) and a coupled qubit-resonator system when the qubit is in the ground state (blue, left) and in the excited state (green, right).

single pulse rotates the qubit around an axis of the XY-plane of the Bloch sphere. Any rotation around the z axis can be achieved by a combination of rotations around the x and y axis.

These readout and control methods methods were originally developed for the CPB, but they also hold for the transmon qubit [27]. The only disadvantage of the transmon qubit is its reduced anharmonicity. The time of a pulse is limited by the inverse of the maximal bandwidth in frequency space which is limited by the anharmonicity, since one has to avoid driving the transmon to the thrid level. On one hand, it is desirable to have as short gate times as possible, but on the other hand if the gate time is too short there will be leakage out of the qubit subspace. A way around of this trade-off is a pulse shape proposed by Motzoi et al. in 2009 [36] called *Derivative Removal by Adiabatic Gate* (DRAG).

2.5. Coherence Time

In general, the coherence of a qubit is characterized by the T_1, T_2 and T_2^* times, occurring due to weak coupling to the environment [37]. This coupling leads to quantum noise and further to fluctuations in the qubit transition frequencies. The time a qubit in the excited state needs to emit its energy and end up in the ground state is called *relaxation time* T_1. Then, the time until we have lost all information about the qubit phase is represented by the *dephasing time* T_2, which is also called transversal relaxation. The rate of the dephasing is is given by the relaxation time of the qubit and a second term [37]

$$\frac{1}{T_2} = \frac{1}{2T_1} + \frac{1}{\tau_\phi}, \tag{2.27}$$

where τ_ϕ is the *pure dephasing time*. The ensemble-average based dephasing time, called T_2^*, is obtained by averaging over several measurements of an observable such as the excited state probability after a sequence of two $\pi/2$ pulses, which is called *Ramsey experiment*. Typically there are parameters that fluctuate on a time-scale slower than the repetition rate of the measurements. Those fluctuating parameters cause decoherence in addition to the decoherence in each single experiment. Therefore, the ensemble-averaged dephasing time is smaller or equal to the T_2 time: $T_2^* \leq T_2$. Sources of low frequency or $1/f$ noise, which is a major reason of limited coherence times, are fluctuations in the transparency of the Josephson junction, charge fluctuations and magnetic-flux fluctuations. We will see later that these sources of noise cause a lower limit to the errors of quantum gates. Hence, it is one of the main goals of current research to increase coherence time of qubits by developing new designs.

2.6. Experimental Setup

The experiments for the current thesis were performed on a sapphire sample chip containing four transmon qubits (Q1-Q4) made of aluminum which are dispersively coupled to coplanar transmission line resonators (R1-R4) made of niobium, as shown in Figure 2.7. This sample was also used for digital quantum simulations of spin models [38]. In this chip design, each qubit has an individual microwave drive line (green) and flux line (blue). All resonators act as quantum bus enabling two qubit gates (Chapter 4), whereas only resonator R1 and R4 are used for readout and therefore possess an input and output port (red). By design, the resonators have fixed resonance frequencies of 7.1 GHz to 9.1 GHz. The frequencies of the different qubits can be varied by the flux through the SQUID loop according to Equation 2.17. With aid of a bias magnetic field originating from three superconducting coils underneath the chip, the qubit frequencies are held at parking positions between 4.8 GHz and 6 GHz. In Figure 2.8, the $g \leftrightarrow e$ and the $e \leftrightarrow f$ transitions of all four qubits are presented. Due to the high sensitivity of the transmon qubit towards magnetic field fluctuations, the coils are connected to isolated battery sources producing a low-noise dc current.

In the interest of performing accurate single-qubit gates, it is crucial to achieve accurate control of amplitude, frequency and phase of microwave pulses on nanosecond timescales. This is reached with an IQ-Mixer by modulation of a local oscillator (LO) signal from a phase locked microwave generator. The LO signal is therefore split into two signals, one of which is in-phase with the input signal and the other is shifted about $-\pi/2$. Then, the so called in-phase I and shifted quadrature Q signals are multiplied by ac voltages $I = A\cos(\omega_{IF}t + \phi)$ and $Q = B\cos(\omega_{IF}t + \phi_Q + \phi)$ respectively. Here, the I and Q voltage signals are produced by an 1.0 GS/s arbitrary waveform generator (AWG). With this *quadrature upconvention* method we are able to accurately modulate the amplitude, frequency and the phase of the LO microwave

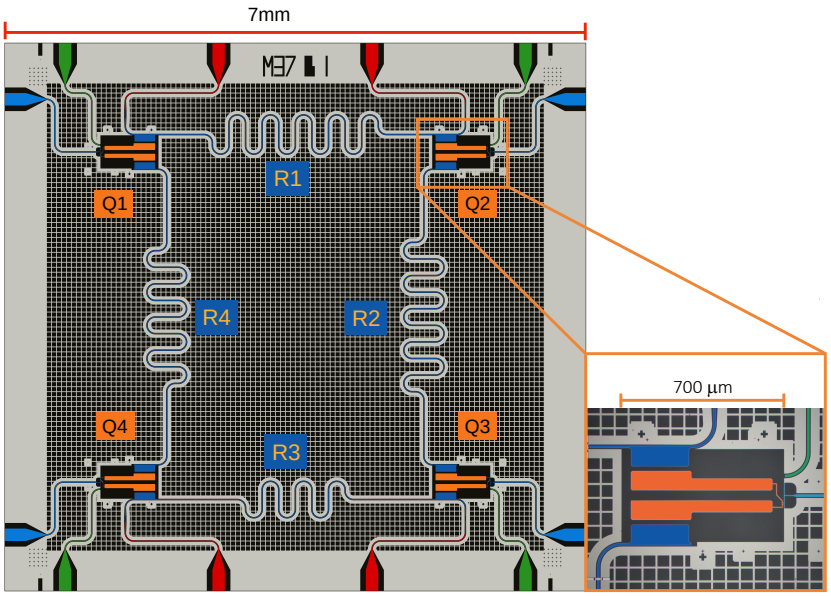

Figure 2.7.: Design of the sample chip used in this thesis. Each of the four qubits (Q1-Q4) has an individual qubit drive line (green) and a fluxline (blue) and is capacitively connected to two of the four transmission line resonators (R1-R4). Input and Output ports (red) of resonators R1 and R3 serve as readout line for all qubits. Image taken from [38]

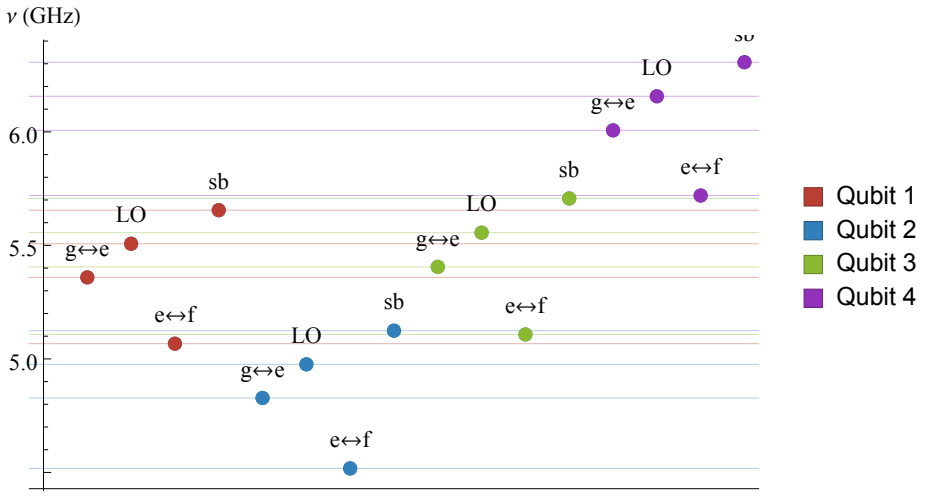

Figure 2.8.: Shows the frequencies of qubits 1 to 4, where $g \leftrightarrow e$ and $e \leftrightarrow f$ denotes the transition frequencies from the ground to the first excited state and first to second excited state respectively. Due to possible mixer leakage, also local oscillator (LO) and the other sideband (sb) frequency are important.

signal. In the special case of *single-sideband mixing*, where the phase shift between the AWG signals is $\phi_Q = \pm\pi/2$ and the amplitudes are equal $A = B$, the resulting microwave signal is

$$A\cos(\omega_{IF}t + \phi)\cos(\omega_{LO}t) \mp A\sin(\omega_{IF}t + \phi)\sin(\omega_{LO}) = A\cos\left((\omega_{LO} \pm \omega_{IF})t + \phi\right) \tag{2.28}$$

Hence, the local oscillator frequency is shifted by an intermediate frequency of $\pm\omega_{IF}$ according to the sign of ϕ_Q. Thereby, the gate becomes less sensitive to mixer imperfections, which, in the other case, would lead to leakage and unwanted qubit driving. However, due to imperfect I and Q splitting and combining or different cable lengths between the AWG and the I and Q port of the IQ-Mixer resulting in phase and amplitude imbalances of the final signal, also leakage at the sideband frequencies is possible. By sweeping the phase ϕ_Q and amplitude B of the Q quadrature signal, the values that minimize the power of the unwanted sideband can be estimated. In the same manner, the leakage at the carrier frequency (LO), which is caused by DC offset errors at the IQ ports, is minimized. There, the I and Q signal voltages are swept to find the optimal combination. These calibration methods are especially important for two-qubit gates, where leakage at the LO and cancelled sideband (sb) frequencies (Figure 2.8) have to be taken into consideration.

As mentioned above, the resonator input and output lines are used for dispersive readout of the qubit states. As soon as the AWG sends a measurement trigger to a microwave generator a measurement tone tuned in resonance with the resonator is switched on, while the transmitted signal at the output line is measured. Since there are only a few photons in the resonator on average, the power of the transmitted signal is very weak and has to amplified by a factor of more than 10^{10} to be detectable [39, Chpt. 4.3]. In a first step, this is done by a Josephson-parametric amplifier [40, 41]. Then, the signal is downconverted to an intermediate frequency of $\omega_{LO} = 25\,\text{MHz}$ (*heterodyne detection*) leading to I and Q quadrature signals. Both of these signals are then digitized and further, digitally, downconverted by Field Programmable Gate Array (FPGA) (*digital homodyne*). In the end, the qubit states are extracted from the resulting, time-dependent I and Q quadratures. This process will be explained in detail in Section 4.3. Due to the accumulated noise during the amplification the results are averaged 10^3 to 100×10^3 times.

To achieve typical qubit lifetimes of 4 µs to 6 µs the system has to be well isolated against environment noise. First of all, the chip is mounted to a baseplate of a $^3He/^4He$ dilution refrigerator, cooled down to 20 mK to 30 mK to prevent thermal excitation. In order to protect the qubits against thermal radiation caused by high-frequency electromagnetic fields (Johnson-Nyquist noise), the incoming signals are attenuated at each temperature stage in the fridge. Furthermore, there are two layers of a high-permeability nickel-iron alloy shields (Cryoperm$^{\text{TM}}$) around the sample, to shield it from external magnetic fields.

3. Single-Qubit Randomized Benchmarking

A key requirement for scalable quantum computing is to have independent low-error gates. Independent in the sense that the error of a gate does not depend on the initial state such that the gate works equally well in every context. In our system, the major sources of noise or error are interactions with the environment and imprecision in the classical control. To have a comparable measure of the error of quantum gates, quantum information theory uses the *gate fidelity*. It is based on the *fidelity*, which compares two quantum states with each other. Let us now introduce a formal definition of gate fidelity F_g we use to characterize a quantum gate described by an unitary evolution operator U. For pure states, it is an inner product of the theoretically expected state ϕ_{theor} and the experimentally measured state ϕ_{meas}

$$F_g = |\langle \phi_{theor} | \phi_{meas} \rangle| \tag{3.1}$$

When we assume gate imperfections to be a separate quantum operation represented by a Kraus superoperator (completely positive map) $\Lambda(\rho) = \sum_k A_k \rho A_k^*$, which we call noise operator, and average over all possible input states we get the *average gate fidelity* defined as the expectation value of all possible input states ϕ [42]

$$\bar{F}_g(\Lambda) = \mathbb{E}_\phi \left(F_g(U, \Lambda, \phi) \right) = \int \mathrm{d}\phi \, \langle \phi | \, U^{-1}[\Lambda(U \, |\phi\rangle \, \langle \phi | \, U^{-1})] U \, |\phi\rangle \tag{3.2}$$

Here, U does not introduce any loss in fidelity since it describes by definition the ideal gate evolution. Since the resulting fidelity of a gate with zero error is 1, the fidelity takes on values in between 0 and 1. Furthermore, the average gate fidelity is invariant of the initial state and depends only on the noise operator. Rewriting Equation 3.2 yields [43]

$$\bar{F}_g(\Lambda) = \frac{\sum_k |Tr(A_k)|^2 + d}{d^2 + d}, \tag{3.3}$$

where d is the dimension of the gate U. In other words, the fidelity of a gate can be estimated by only knowing the Kraus operators of the noise operation. As mentioned, a reliable method to exactly identify the imperfections of a gate is quantum process tomography. There, the gate is applied to each state of a set of states spanning the Hilbert space and then measured tomographically, leading to the probability to be in one of the possible output states. As a result, QPT allows a complete reconstruction of the superoperator and accordingly its noise

superoperator. Besides the disadvantage in scaling to a larger number of qubits, this method also suffers from the dependence on state preparation and measurement since the initial states and basis rotations are always the same.

In this chapter we will introduce a scalable method to measure the fidelity of single quantum gates, whose estimated average gate fidelity is not influenced by SPAM errors. First, the general concept behind randomization is explained in the following Section 3.1. Then, in Section 3.2 the first realized randomized benchmarking protocol is discussed. After that we will have a look at the Clifford method (Section 3.3), which is also used for two-qubit gates in Chapter 4. Finally, the interleaved randomized benchmarking (Section 3.4) provides an expansion of the Clifford method and allows to estimate the error of a specific gate in the Clifford group.

3.1. Randomized Noise Estimation

A method to bypass the problems of scalability and SPAM is given by randomized noise estimation [42]. Here, the key idea is to measure the fidelity of the "motion reversal" transformation UU^{-1} applied on a initial state represented by $\rho_\phi = |\phi\rangle\langle\phi|$. The gate fidelity of such a gate is, similarly to Equation 3.2, described by

$$F_g = Tr\left[\rho_\phi U^{-1}\Lambda(U\rho_\phi U^{-1})U\right], \tag{3.4}$$

with the difference that the error Λ now describes the error of both, the forward transformation and the reversed transformation. In order to randomize the process, the gate fidelity is integrated over the set of all unitary gates with dimension d instead of all possible input states.

$$\mathbb{E}_U(F_g) = \int_{U(d)} \mathrm{d}U Tr\left[\rho_\phi U^{-1}\Lambda(U\rho_\phi U^{-1})U\right] \tag{3.5}$$

Note that due to

$$\begin{aligned}
\mathbb{E}_\phi\left(F_g\right) &= \int \mathrm{d}\phi\, Tr\left[\rho_\phi U^{-1}\Lambda(U\rho_\phi U^{-1})U\right] \\
&= \int \mathrm{d}\phi\, Tr\left[M\rho_\phi M^{-1}U^{-1}\Lambda(UM\rho_\phi M^{-1}U^{-1})U\right] \\
&= \int \mathrm{d}U'\, Tr\left[\rho_\phi (U')^{-1}\Lambda(U'\rho_\phi (U')^{-1})U'\right] \\
&= \mathbb{E}_U(F_g),
\end{aligned} \tag{3.6}$$

where we have defined the new operator $U' = UM$, the expression Eq. 3.5 is equivalent to the average gate fidelity $\bar{F}_g(\Lambda)$. By writing Λ and U in the natural representation $\hat{\Lambda} = \sum_k A_k \otimes A_k^*$ and $\hat{U} = U \otimes U^*$, the U-averaged gate fidelity can be written as [42]

$$\bar{F}_g(\Lambda) = Tr\left(\rho\left[\int \mathrm{d}U \hat{U}\hat{\Lambda}\hat{U}^{-1}\right]\rho\right) = Tr\left(\rho\hat{\Lambda}^{ave}\rho\right) = F_g(\hat{\Lambda}^{ave}) \tag{3.7}$$

In this sense, the average gate fidelity of an operator U is estimated by the gate fidelity of an average error operator $\hat{\Lambda}^{ave} = \int \mathrm{d}U \hat{U}\hat{\Lambda}\hat{U}^{-1}$. Moreover, $\hat{\Lambda}^{ave}$ is independent of the set $U(d)$ [42]. Hence, it can be expressed as a simple depolarizing channel

$$\hat{\Lambda}^{ave}(\rho) = p\rho + (1-p)\frac{\mathbb{I}}{d} \tag{3.8}$$

where $p \in [0,1]$ is a parameter indicating the strength of the depolarization. Inserting this definition in Equation 3.7 yields

$$\bar{F}_g(\Lambda) = p + \frac{(1-p)}{d} \tag{3.9}$$

Therefore, the average gate fidelity only depends on the parameter p, which can be interpreted as intrinsic strength of the cumulative noise. As theoretically proposed by J. Emerson, R. Alicki and K. Zycykowski in 2005 [42], this paramter can be estimated experimentally. They suggested that p is the residual population of the intrinsic state after applying randomly chosen self-inverting sequences of gates.

The idea of determining the average gate fidelity from the sequence fidelity of random self-inverting sequences forms the fundamental concept of randomized benchmarking. In the next section we will discuss the method used during the first experimental demonstration of single-qubit RB on trapped atomic ion qubits by Knill et al. in 2008 [13].

3.2. Pauli Method

The Pauli method refers to the randomized benchmarking method introduced by Knill et al. in 2008 [13]. In order to distinguish conveniently between other methods, we introduced the name Pauli method. Beside slight differences in the practical realization, its core principles are based on the randomized noise estimation idea from the previous section. The idea of applying randomized self-inverting sequences of gates to an initial state and measuring the sequence fidelity as a function of sequence length stays the same. But in contrast to before, the gates are now taken from a subset of the single-qubit *Clifford group* $\mathcal{C}_1$ instead of the group containing all unitary gates. The Clifford group, also called the normalizer of the Pauli group, is per definition the group of operations that maps elements of the Pauli group $\mathcal{P}$ to itself under conjugation $CPC^\dagger \in \mathcal{P}$ for $C \in \mathcal{C}$ and $P \in \mathcal{P}$ [44]. In this sense, when starting in the ground or excited state of a qubit, Clifford rotations on the Bloch sphere always end up in an eigenstate of a Pauli operator. Moreover, since the noise for Clifford gates is already depolarized the estimations from Section 3.1 still hold [13]. This restriction simplifies the protocol remarkably, because all single-qubit gates of the Clifford group $\mathcal{C}_1$, which are basically combinations of π and $\pi/2$ pulses (see Appendix B), are simple to implement. Furthermore, to get an estimation of the error of Clifford gates is of great interest, since typical fault-tolerant algorithms are very sensitive

to errors of gates in this group. Finally, by only adding one additional single-qubit gate, for example the $\pi/8$ gate, to the Clifford group the whole unitary group can be generated [14].

The sequences of gates used in this method consist of alternating *computational gates* G_i and *Pauli gates* P_i in order to ensure the randomization of the measurement results. The group of computational gates contains $\pi/2$ pulses around the x and y axis of the Bloch sphere given by $e^{\pm i\sigma^{x,y}\pi/4}$, where σ^x and σ^y are the well-known Pauli-X and Pauli-Y operators (see Appendix A.1). From this group, N_G different sequences of length L are generated randomly and each of them is truncated into N_l pieces of length $l_1 < l_2 < ... < l_{N_l} = L$. As a result, one obtains N_G sequences for every length l_k and a total of $N_G N_l$ sequences. Yet, none of the sequences, except maybe a few by accident, are self-inverting. Hence, a last pulse R from the computational group is added at the end of every sequence (Figure 3.1), such that it brings the state of the qubit to an eigenstate of the σ^z operator ($|g\rangle$ *or* $|e\rangle$). Hence, strictly speaking, the sequences are not self-inverting as proposed in the randomized noise method. Therefore, the theoretical outcome has to be considered when plotting the expected state population in the end. As illustrated in Figure 3.1(b), the obtained sequences from Fig. 3.1(a) are randomized by applying Pauli randomization pulses P_i in between every operator G_i and the final gate R, such that each sequence starts and ends with a P pulse. This Pauli randomization group consists of the identity gate given by $e^{\pm i\mathbb{1}\pi/2}$ and π pulses around the x, y and z axis given by $e^{\pm i\sigma^{x,y,z}\pi/2}$. By interleaving every sequence with N_P randomly generated sequences of Pauli randomization gates, we ensure that the measurement result is uniformly distributed and that it is not biased by any combination of computational gates. Such an unwanted combination is, for example, three $(\pi/2)_x$ gates with an over-rotation error of 1/3 each, because this would be interpreted as two perfect π_x pulses. Theoretically, the sign of the π pulses does not matter, since it just leads to different global phases, but due to gate imperfections this may affect the error of the sequence. In total, a complete randomized benchmarking experiment counts $N_G N_l N_P$ sequences, in which the longest sequences have a length of $2(L+1)+1 = 2L+3$ gates. Note, that the index l refers to the number of computational gates in the sequence, since the pulses from the Pauli randomization group are viewed as rotations of the Bloch sphere axes in order to randomize the outcome.

The resulting probability of the incorrect measurement outcome, or error probability ϵ, of every sequence is used to estimate the average gate fidelity of the computational gates. Yet, as we will see in Section 3.3, it can be argued that the Pauli method not only depends on the errors of the computational gates but characterises the average gate fidelity of pairs of one computational gate and one Pauli gate. For every length l the $N_G N_P$ fidelities between expected and measured final state $F_l = 1 - \epsilon_l$ are averaged and plotted as a function of l. Assuming that the errors are independent and lead to a depolarized (completely mixed) state, every randomized computational gate A, consisting of a Pauli randomization gate and a computational gate (Figure 3.1),

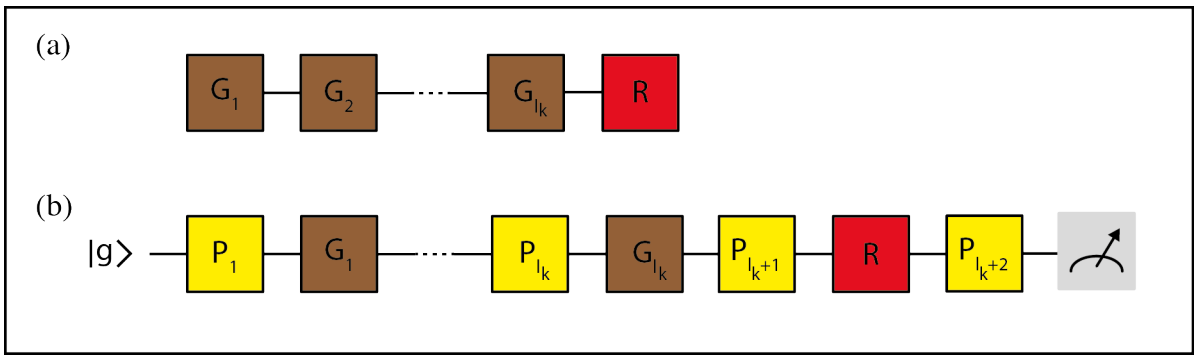

Figure 3.1.: Schematic sketch of how to obtain a randomized sequence for the Pauli method. **(a)** Every randomly chosen sequence with computational gates is truncated into different lengths l_k. The theoretically calculated state after gates G_1 to G_{l_k} is used to estimate the final gate R that rotates the state onto the z axis in the Bloch sphere. **(b)** To reach a randomized outcome, the sequence from (a) is interleaved with randomly generated sequences of Pauli randomization gates P_1 to P_{l_k+2}. Each of the randomized sequences is then applied to the ground state $|g\rangle$. The Fidelity between the resulting state and the expected state is used to estimate the average gate error $\bar{\epsilon}$.

can be given a probability p_A of not being depolarized. Thus, the probability that the state after a sequence of $2l+3$ gates has not been depolarized is $\Pi_{j=0}^{2l+3} p_{A_j}$. Expressed in terms of p_A the probability to be in the correct state after a sequence, assuming random errors, takes the form [13]

$$\begin{aligned} F_l &= \mathbb{E}\left(\frac{1}{2}\left[1 - \Pi_{j=0}^{2l+3}\, p_{A_j}\right]\right) \\ &= \frac{1}{2}\left[1 - \mathbb{E}\left(\Pi_{j=0}^{2l+3}\, p_{A_j}\right)\right] \\ &= \frac{1}{2}\left[1 - \mathbb{E}\left(p_{\text{if}}\, p^l\right)\right] \\ &= \frac{1}{2}\left[1 - p_{\text{if}}\, p^l\right], \end{aligned} \tag{3.10}$$

where p denotes the average probability of being not depolarized and p_{if} is the probability that the prepared state, the first Pauli pulse and the measurement are not depolarized. As a result, it is expected that the fidelity decreases exponentially with the sequence length. Note that the fidelity converges to $1/2$ since the completely mixed state is with 50 % probability in one of the two σ^z eigenstates when measured. Assuming that the average error is represented by a unitary dephasing error as given in Eq. 3.8 with dephasing probability $1-p$, the average gate fidelity is estimated by Equation 3.9. Hence, the average gate fidelity is solely derived from the base of the exponential fit to the data.

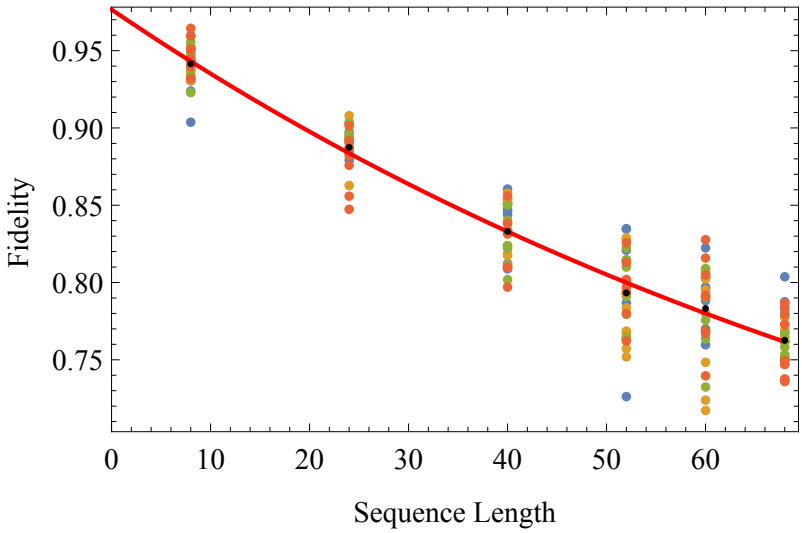

Figure 3.2.: Randomized benchmarking measurement with the Pauli method. The fidelity of of every sequence is plotted as a function of sequence length (coloured points). For every sequence length the sequence fidelities are averaged (black points). An exponential curve defined in Eq. 3.10 with parameters p_{if} and p is fitted to the averaged data (red line). Information about the average gate fidelity or the average gate error can then be extracted from the fitting parameter p.

This method of randomized benchmarking was first demonstrated on superconducting qubits by Chow et al. in 2009 [12]. In our lab it was implemented by L. Steffen [45] and L.Ciorciaro [46]. With the standard values of $N_G = 4$ randomly generated sequences truncated into $N_l = 6$ different lengths $(8, 24, 40, 52, 60, 68)$ and randomized with $N_P = 8$ different Pauli sequences, we get an average gate fidelity of approximately 99.5 % for single-qubit gates. The resulting plot is shown in Figure 3.2.

In this section we have discussed a possible method of estimating the average gate fidelity of single-qubit gates. However, there are several drawbacks concerning the Pauli method. First of all, a problem that also occurs in the randomized noise estimation is the assumption of gate-independent errors. In reality also time and gate dependent errors have to be taken into account. The derived estimation for an exponentially decaying fidelity only holds for independent errors and it is therefore not clear if all errors behave similarly. Since, there are no conditions for a reliable estimation of the error, it is unclear how the parameters have to be chosen to get an accurate result. A simple, although unlikely example occurs when the error is gate-dependent and is equal to the inverse of the gate. In this case the Pauli method will always lead to a average gate fidelity of 100 % with no error, which is obviously not true. Moreover, the protocol is limited to the single-qubit case and it is ambiguous how to expand it to the multi-qubit case.

3.3. Clifford Method

In 2011, E. Magesan, J. M. Gambetta and J. Emerson [14,15] proposed a provably scalable and expandable method for randomly estimating the average gate fidelity. In principle, this method, which I will refer to as Clifford method, works like the two methods discussed before. After preparing the qubit in the ground state a self-inverting sequence of Clifford gates is applied and from the fidelity of the resulting states compared to the ground state the desired gate fidelity is calculated. Its name arises from the restriction to the full Clifford group $\mathcal{C}_n$ and not just a subgroup as in the Pauli method. Besides the several reasons for using the Clifford group mentioned in the previous section, a protocol based on this group has the advantage that it can be expanded to multi-qubit gates. In the single-qubit case, the cost of implementing a randomized computational gate with the Pauli method is two pulses, since it consists of a Pauli randomization pulse and a computational pulse (see Section 3.2). By expanding the group of computational gates to the full Clifford group which has 1.875 pulses per gate (Appendix B), we will not have to use longer pulse sequences.

3.3.1. Derivation of the Expected Fidelity Decay

Here we derive the formulas that describe the decay in sequence fidelity, which is later used as a fit function for extracting the average gate fidelity. Similar to before, K sequences of length m of randomly chosen Clifford gates $C \in \mathcal{C}_n$ are generated. To make the sequences equal to the unity operator, a last uniquely determined gate C_{m+1} is added, which is the inverse of the whole sequence (see Figure 3.3(a)). Since all gates of the sequence belong to the Clifford group, this last gate has also to be an element of the group. We define the gate and time dependent error for every Clifford gate to be represented by the superoperators $\Lambda_{i_j,j}$. With this definition of the error operator each of the K_m sequences is given by [14], [15]

$$\begin{aligned} S_{i_m} &= \bigcirc_{j=1}^{m+1} \left(\Lambda_{i_j,j} \circ C_{i_j}\right) \\ &= \Lambda_{i_{m+1},m+1} \circ C_{i_{m+1}} \circ \Lambda_{i_m,m} \circ C_{i_m} \circ ... \circ \Lambda_{i_1,1} \circ C_{i_1} \end{aligned} \tag{3.11}$$

where the index $i = 1, 2, 3, ..., K$ indicates the sequence number and $j = 1, 2, 3, ..., m+1$ the position of a gate in a sequence with length $m+1$. We define the new random gate D as $D_{i_j} = C_{i_{j+1}} \circ ... \circ C_{i_1}$, which is useful for the derivation of the expected decrease in sequence fidelity. The superoperator D has the property that $C_{i_j} = D_{i_j} \circ D^{\dagger}_{i_{j-1}}$ since $C_{i_j} \circ C^{\dagger}_{i_j} = \mathbb{I}$. Furthermore $D_{i_{m+1}} = \mathbb{I}$, because the full sequence is strictly self-inverting. Therefore, the sequence can be rewritten as

$$\begin{aligned} S_{i_m} &= \Lambda_{i_{m+1},m+1} \circ D_{i_{m+1}} \circ D^{\dagger}_{i_m} \circ \Lambda_{i_m,m} \circ D_{i_m} \circ D^{\dagger}_{i_{m-1}} \circ ... \circ D^{\dagger}_{i_1} \circ \Lambda_{i_1,1} \circ D_{i_1} \\ &= \Lambda_{i_{m+1},m+1} \circ \bigcirc_{j=1}^{m} \left(D^{\dagger}_{i_j} \circ \Lambda_{i_j,j} \circ D_{i_j}\right) \end{aligned} \tag{3.12}$$

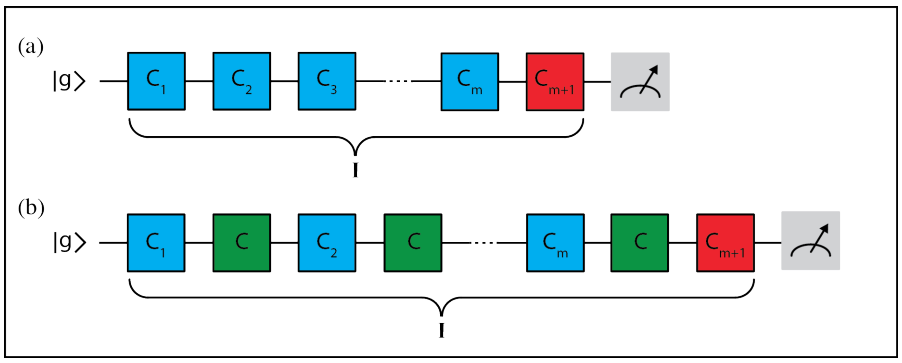

Figure 3.3.: Sketch of the sequence constellation of the standard and interleaved Clifford method. **(a)** In the standard randomized benchmarking protocol sequences of gates from the Clifford group C_1 to C_m (blue boxes) are randomly generated. With an exactly determined final gate C_{m+1} (red box), which is also part of the Clifford group, the whole sequence is inverted. **(b)** In order to determine the fidelity of a specific gate C, the randomly generated sequences of Clifford gates are interleaved with the respective gate C (green box). Since this gate changes the behaviour of the sequence the final gate C_{m+1} is calculated after the interleaving process.

Note that up to now, we have only made the assumption that the error $\Lambda_{i_j,j}$ does not depend on operations before C_{i_j}. Since we are interested in the average of all sequences, it is convenient to introduce the *average sequence operation*

$$S_m = \frac{1}{K_m} \sum_{i_m}^{K_m} S_{i_m}. \tag{3.13}$$

In order to find the fitting model of the fidelity versus sequence length, we assume that the errors $\Lambda_{i_j,j}$ only differ by a small amount $\delta\Lambda_{i_j,j}$ from the mean value Λ and use a *pertubative expansion* method for

$$\Lambda_{i_j,j} = \Lambda + \delta\Lambda_{i_j,j}. \tag{3.14}$$

Therefore, an approximation to zeroth order corresponds to gate and time independent errors, whereas an approximation to first order considers the case where one gate in the sequence of $m+1$ gates is gate and time dependent or none of them. Every order of approximation till $k = m+1$ brings the calculated model closer to reality. In this sense, it is reasonable to write $\bar{F}_g = F_g^{(m+1)}$. When starting in state $|\phi\rangle$ the fidelity of a single sequence is given by $Tr[\mathbb{E}_\phi\, S_{i_m}(\rho_\phi)]$, where $\mathbb{E}_\phi$ is a POVM element. Hence, the *averaged sequence fidelity* to k-th order is described by [14], [15]

$$F_{seq}^{(k)}(m,\phi) = Tr\left[\left(\sum_{k=0}^{m+1} S_m^{(k)}\right)(\rho_\phi)\mathbb{E}_\phi\right] \tag{3.15}$$

If we assume to have gate and time independent errors $\Lambda_{i_j,j} = \Lambda$, as in the Pauli method, each of the independent elements $\left(D_{i_j}^{\dagger} \circ \Lambda \circ D_{i_j}\right)$ from Equation 3.12 corresponds to the average error operation $\hat{\Lambda}$ introduced in Eq. 3.7. Consequently, the average sequence operation given in Eq. 3.13 reduces to [14], [15]

$$S_m^{(0)} = \Lambda \circ \hat{\Lambda}^{ave} \circ ... \circ \hat{\Lambda}^{ave} \tag{3.16}$$

According to Equation 3.15 derived before the fit function of the average sequence fidelity is then given by [14], [15]

$$\begin{aligned} F_{seq}^{(0)}(m,\phi) &= Tr\left[S_m^{(0)}(\rho_\phi)\mathbb{E}_\phi\right] \\ &= Tr\left[\Lambda \circ (\hat{\Lambda}^{ave})^{\circ m}(\rho_\phi)\mathbb{E}_\phi\right] \\ &= Tr\left[\Lambda\left(p\rho_\phi + (1-p)\frac{\mathbb{I}}{d}\right)^{\circ m}\mathbb{E}_\phi\right] \\ &= Tr\left[\Lambda\left(\rho_\phi - \frac{\mathbb{I}}{d}\right)\mathbb{E}_\phi\right]\, p^m \;+\; Tr\left[\Lambda\left(\frac{\mathbb{I}}{d}\right)\mathbb{E}_\phi\right] \\ &= A_0\, p^m \;+\; B_0 \end{aligned} \tag{3.17}$$

where the two new defined constants A_0 and B_0 absorb the preparation and measurement errors. Thus, gate and time-independent errors lead to an exponential decay of the fidelity, as already proven in the Pauli method.

Much more interesting is the case where we add a gate and time-dependent error to the sequence to first order. Due to the time dependence of the error there are $m+1$ first order pertubation terms that differ from each other by the position of the dependent gate. I will not conduct the calculations for this case, since they are very long and time consuming. They are shown in detail in Ref. [15]. The approach of a single time and gate dependent error leads to the fitting model

$$F_{seq}^{(1)}(m,\phi) = A_1\, p^m \;+\; B_1 \;+\; C_1\,(m-1)(q-p^2)\,p^{m-2} \tag{3.18}$$

Again the preparation and measurement errors are absorbed by the constants A_1, B_1 and C_1. In contrast to the zeroth order, the fit is not perfectly exponential anymore due to the term $C_1\,(m-1)(q-p^2)\,p^{m-2}$. In this way, $q-p^2$ is a measure of the gate-dependence of the errors. Additionally, if the error is time dependent the parameters $A_1(m), B_1(m)$ and $q(m)$ get a slight dependence on m.

So far we know how the fidelity decreases for zeroth and first order in the pertubation expansion of time and gate dependent errors, but is it necessary to calculate the behavior up to the $(m+1)$-th order? With help of the $(1\to1)$-norm the difference of the average sequence fidelity function between k-th and $(k+1)$-th order can be estimated [15]

$$\left|F_g^{(k+1)}(m,\phi) - F_g^{(k)}(m,\phi)\right| \leq \sum_{j_k>...>j_1} \gamma_{j_k}...\gamma_{j_1} \tag{3.19}$$

where j_1 to j_k are the positions of the time-dependent errors in the sequence and

$$\gamma_j = \frac{1}{|\mathcal{C}_n|} \sum_i \|\Lambda_{i_j,j} - \Lambda\|_{1\to 1}^H \tag{3.20}$$

is the time-dependent variation in the noise. In the event of time-independent errors the estimation reduces to

$$\left| F_g^{(k+1)}(m,\phi) - F_g^{(k)}(m,\phi) \right| \leq \begin{pmatrix} m+1 \\ k \end{pmatrix} \gamma^k \tag{3.21}$$

where

$$\gamma = \frac{1}{|\mathcal{C}_n|} \sum_i \|\Lambda_i - \Lambda\|_{1\to 1}^H \tag{3.22}$$

From these two estimations we conclude that second order terms can be neglected if the variation in the noise γ is much smaller than $1/(m+1)$. However, for the sake of having enough data points also $m \gg 1$ needs to be fulfilled.

The average gate fidelity is determined from p through Equation 3.9. If p is extracted from a fit to $F_{seq}^{(0)}$ (gate and time-independent errors) we call the resulting average gate fidelity $F_{ave}^{(0)}$, otherwise we call it $F_{ave}^{(1)}$. This approach is still correct, since the average error of Clifford gates is depolarizing and can be viewed as a depolarizing channel with depolarization probability $1-p$. Beside the characteristic average gate fidelity, there is another, often used value, the *average gate error* $\epsilon_{ave} = 1 - F_{ave}$.

3.3.2. Experimental Results

In our lab, the Clifford randomized benchmarking method for single-qubit gates was first tested with 20 randomly generated sequences, which were then truncated into lengths of 2, 3, 4, 6, 8, 11, 14, 18, 22, 27, 32, 38, 44, 51, 58, 66 and 70. The restriction in the length of the sequences came from the set fixpoint at 4.1 µs in our measurement setup, which means that there is a 4.1 µs duration reserved for applying the pulses that implement the sequence before the final state is read out. From this usable duration one has to subtract the offset between the AWG channels which is typically on the order of 500 ns. Each one of our calibrated and DRAG-corrected single-qubit pulses has a length of 21 ns (see Section 2.4 for details on the single qubit pulses). Therefore, the number of possible pulses is roughly 190. In the worst case, every element of the randomly generated Clifford sequences contains 3 microwave pulses leading to a maximally allowed number of 63 Clifford gates in each sequence. On average there are 1.875 physical pulses per Clifford gate which allows sequence lengths of up to 101 gates. To be on the safe side, a sequence length of 70 was chosen. The resulting fidelity curve of such a measurement is shown in Figure 3.4(a). For this specific measurement the average gate fidelities were $F_{ave}^{(0)} = 99.533(37)\,\%$ assuming gate-independent errors and $F_{ave}^{(1)} = 99.898(449)\,\%$ in the first approximation for gate

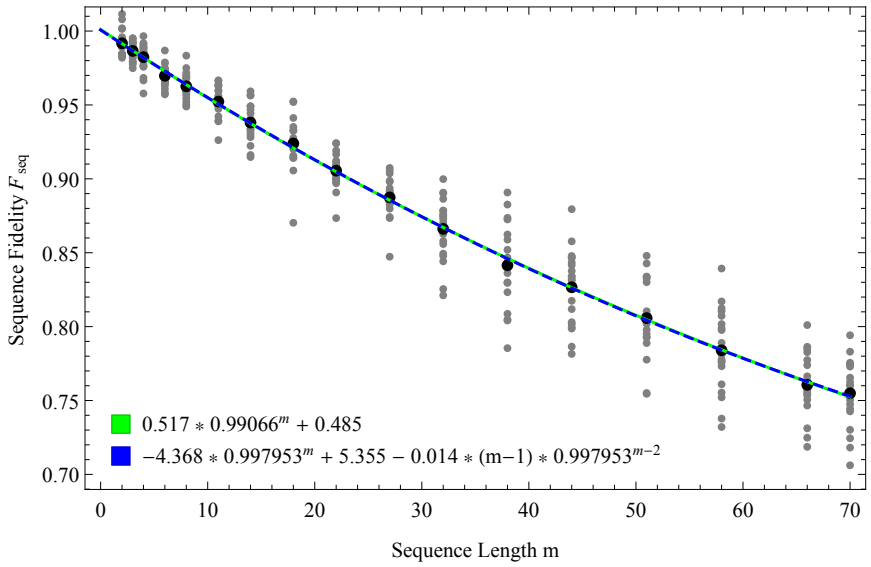

(a) With sequences up to 70 Clifford gates and 20 data points for every length, the fitted parameter $p = 0.99066$ assuming independent errors leads to an average gate fidelity of $F_{ave}^{(0)} = 99.533(37)\,\%$, whereas in the gate and time-dependent case $p = 0.997953$ gives a fidelity $F_{ave}^{(1)} = 99.898(449)\,\%$ (see text for a derivation)

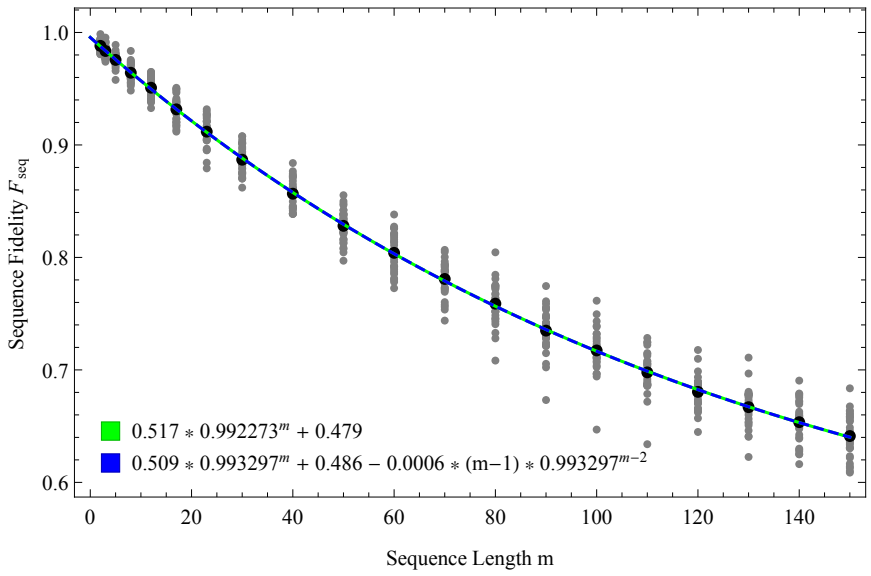

(b) A more accurate estimation of the average gate fidelity is made for sequence lengths up to 150 and 30 randomly generated sequences. This yields to a fidelity of $F_{ave}^{(0)} = 99.614(6)\,\%$ in the gate and time-independent and $F_{ave}^{(1)} = 99.665(250)\,\%$ in the dependent case

Figure 3.4.: Randomized benchmarking measurement for single-qubit Clifford gates with the estimated sequence fidelity decay fits for gate and time-independent (green) and gate and time-dependent (dashed, blue) through the mean (black) of all data points (grey).

and time-dependent errors. The errors are derived from the error propagation of the fit errors of the parameter p. In general, the measured independent average gate fidelities fluctuated between $F_{ave}^{(0)} = 99.497(42)\,\%$ to $99.871(381)\,\%$, even though all data points were averaged 18×10^3 times. These fluctuations may arise from the low number of 20 data points for each length and the restrictions on the maximal length of the sequence discussed above.

In order to achieve longer sequences, the fixpoint of the setup had to be changed. By setting the fixpoint to 10.1 µs sequences, up to 150 Clifford gates are possible. Furthermore, to get better averaged fidelities for each length the number of randomly generated sequences was increased to 30. With this number, the limits in the standard settings of the measurement setup are reached, due to the finite memory of the FPGA. The maximal number of sample points for the readout is 2^{19}. Thus, taking 850 sample points every 10 ns for each sequence, restricts the maximal number of sequences to $2^{19}/850 \approx 616$. However, since the resulting fitting errors are at the order of magnitude 10^{-3}, there is no need to further increase the number randomized sequences. Moreover, it is close to the commonly used number in research [13], [12] and [16]. The fidelity-sequence plot for 30 randomized sequences truncated to lengths of 2, 3, 5, 8, 12, 17, 23, 30, 40, 50, 60, 70, 80, 90, 100, 110, 120, 130, 140 and 150 is shown in Figure 3.4(b). Again, all measurements were averaged 18×10^3 times. For this specific measurement average gate fidelities of $F_{ave}^{(0)} = 99.614(6)\,\%$ (gate/time independent errors) and $F_{ave}^{(1)} = 99.665(250)\,\%$ (first order gate/time dependent errors) were reached. Despite the improved parameters, small fluctuations in the range of $\pm 0.05\,\%$ were observable. After repeating the measurement 10 times, where each time 30 new randomized sequences were generated, a mean average gate fidelity of $F_{ave}^{(0)} = 99.6465(277)\,\%$ and $F_{ave}^{(1)} = 99.6871(324)\,\%$ in the dependent case was measured. The small deviation of the estimated fidelity in the first-order correction of gate and time-dependent errors, and the fact that both models can be accurately fitted to the data, shows that the occurring errors are mostly due to a general, gate and time-independent gate error.

Since we now know that the errors are generally gate and time-dependent, it is an interesting question how much of this error is due to dephasing. Assuming only dephasing errors, the error probability saturates towards 100 % exponentially over time t by $1 - e^{-(t/T_2)}$ where T_2 is the dephasing time. Hence, the probability to end up in the ground state after a random sequence of gates decreases with sequence length. Each Clifford gate has on average 1.875 single microwave pulses, of which each has a length of 21 ns. The fidelity as a function of sequence length is then given by

$$F_{seq}(m, T_2) = e^{-\frac{1}{T_2}(m \cdot 1.875 \cdot 21)} \tag{3.23}$$

After a sequence with zero gates the fidelity is equal to one, thus the curve can be expressed in the form p^m with $p = e^{-(1.875 \cdot 21)/T_2}$. With Equation 3.9, this leads us to the average gate fidelity. In Figure 3.5, the average gate fidelity is plotted as a function of dephasing time T_2. The plotted curve can be interpreted as maximal reachable gate fidelity in the presence of dephasing

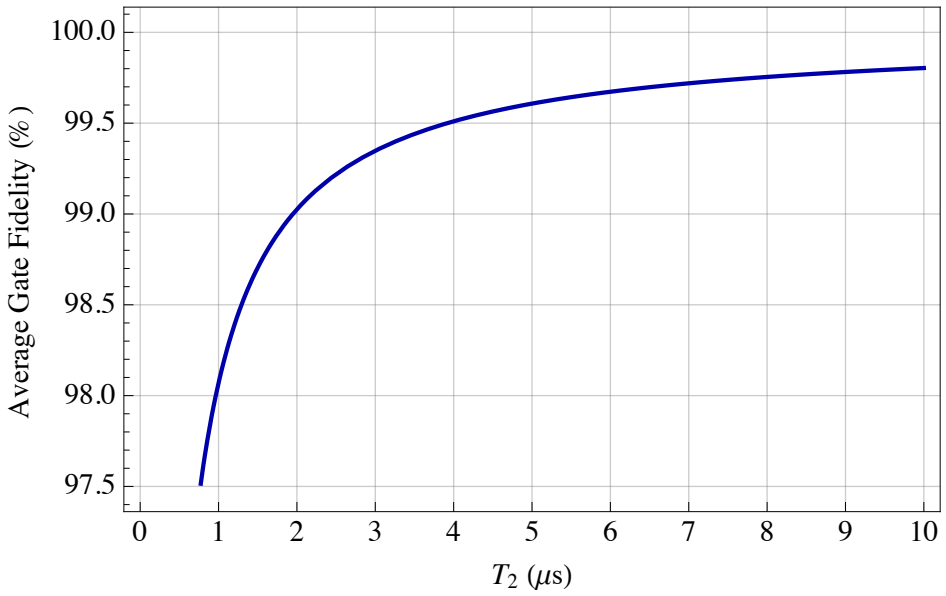

Figure 3.5.: The average gate fidelity and its dependency towards the dephasing time T_2, when the error is entirely caused by dephasing. It provides an upper limit for measurable gate fidelities in the presence of dephasing errors.

errors, which increases for longer dephasing times. In the previous measurement (Figure 3.4(b)), a dephasing time of 7.0847 µs was estimated providing a gate fidelity limit of 99.7229 %. Our determined average gate fidelity of $F_{ave}^{(0)} = 99.614(6)\,\%$ is very close to this limit, which means that the error of our gates is mainly caused by dephasing.

3.4. Interleaved Randomized Benchmarking

With the Clifford method discussed in the Section before (Sec. 3.3) we are able to determine the average gate fidelity or the average gate error of Clifford gates on our device, but, we do not have information about how single gates of the group perform. Since some of the Clifford gates are composed out of three single-qubit pulses, it is assumable that these gates have a higher gate error than others. A method to measure this single gate error was proposed and also demonstrated on a transmon qubit system by Magesan et al. in 2012 [16]. The so called *interleaved randomized benchmarking* is an expansion of the standard Clifford randomized benchmarking. It adopts all advantages the Clifford method brings, such as scalability and the independence of SPAM errors.

The protocol of the interleaved randomized benchmarking consists of two parts, a standard Clifford RB measurement (Section 3.3) and a second Clifford measurement with modified sequences. After extracting the p parameter from a standard RB, the sequences are reused and interleaved with the gate of interest C, as shown in Figure 3.3(b). To get sequences that are equal to the unity gate, the final gate C_{m+1} has to be determined again. Like in the standard case, the sequence fidelity is then determined as a function of sequence length, for which, and this is important, the interleaved gate does not accumulate. In this sense, the gate length is only given by the number of random gates and is not changed by the interleaving process. As a consequence, every interleaved sequence has roughly twice as much gates in an sequence length step, leading to a faster decreasing sequence fidelity. For the sake of avoiding any ambiguity, the obtained p parameter of this fit function (Eq. 3.17 or Eq. 3.18) is written as $p_{\bar{C}}$. With p from the standard RB and $p_{\bar{C}}$ from the interleaved RB, an estimation of the gate error is given by [16]

$$r_{\bar{C}} = \frac{(1-d)(1-\frac{p_{\bar{C}}}{p})}{d} \tag{3.24}$$

To justify this approach conceptually, let us have a look on two different cases. First, assume that the interleaved gate has no error. Then, the measured sequence fidelities lie exactly on the ones from the standard measurement, since only the random gates contribute to the decrease of fidelity. The parameters p and $p_{\bar{C}}$ are therefore equal, which leads to $r_{\bar{C}} = 0$. Second, the error of the interleaved gate is exactly the average gate error of the Clifford group. In this case, $p_{\bar{C}}$ is equal to p^2, because for every sequence length step there are two gates decreasing the sequence fidelity. Putting this relation into Eq. 3.24 yields $r_{\bar{C}} = (d-1)(1-p)/d$ which is the average gate error given by Eq. 3.9.

There is a simple method to test the robustness and the sensitivity of the interleaved randomized benchmarking protocol [16]. An error ϵ in form of an over-rotation in the Bloch sphere is added to a specific gate C. Then, the gate error of this gate and another unmodified gate is measured for increasing over-rotation angles via interleaved RB. If the method works, the error of the modified gate is expected to increase, whereas the error of an non-changed gate stays on the same level. The implemented RB script in our lab was tested with an additional error on the $(\pi/2)_x$ gate. In this case the over-rotation is represented by an additional gate

$$\Lambda(\epsilon) = e^{-i\frac{\epsilon}{2}\sigma^x} \tag{3.25}$$

In Figure 3.6 the results for additional over-rotation angles of roughly $\pi/200$, $\pi/100$, $\pi/40$, $\pi/20$ and $\pi/10$ are shown. For this measurement 30 randomly generated sequences were truncated into lengths up to 44, in consideration that the actual number of Clifford gates in the longest sequence is 88. As expected the error of the non perturbed gate is more or less constant, while the error of the $(\pi/2)_x$ gate visibly increases up to 3.347×10^{-2}. To confirm that the results are in agreement with the theoretical assumptions, the whole process was simulated with manually

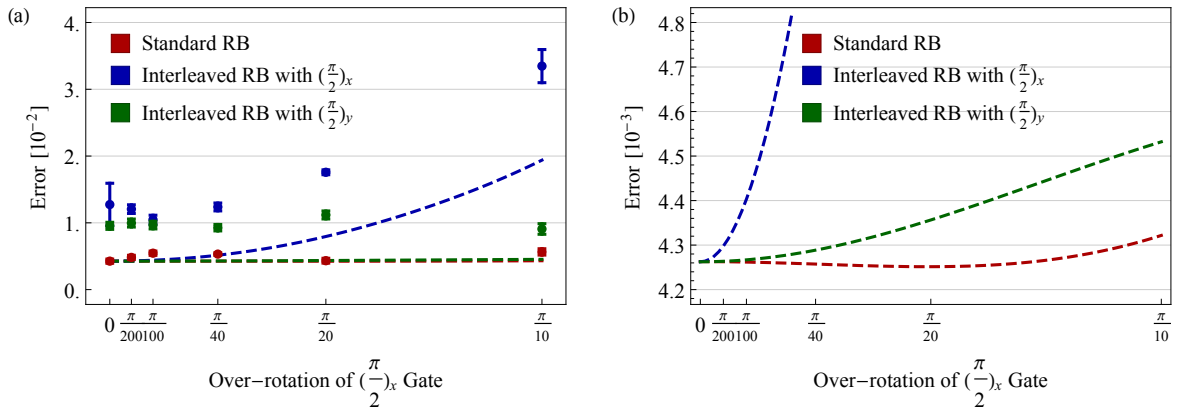

Figure 3.6.: (a) Testing the robustness and sensitivity of the RBClifford protocol for single-qubit gates by adding an additional over-rotation to the $(\pi/2)_x$ gate (blue). In contrast to the unperturbed gate $(\pi/2)_y$ (green) the error of $(\pi/2)_x$ clearly increases. Both error estimations are based on the average gate fidelity of a standard randomized benchmarking measurement (red). The dashed lines represent the simulated measurement assuming a dephasing probability of $p = 0.99794 \cdot e^{-(1.875 \cdot 21ns)/T_2}$ for every gate. **(b)** The development of the simulated measurements zoomed-in.

added dephasing errors. The theoretical expected behaviour of the gate errors for increasing over-rotation error (dashed lines) is shown in Fig. 3.6(a) and in more detail in Fig. 3.6(b). After each gate in the sequence the resulting density matrix was dephased by applying a depolarization gate described by Eq. 3.8 with depolarization probability $p = 0.99794 \cdot e^{-(1.875 \cdot 21ns)/T_2}$ (see Eq. 3.23). In the simulation, a dephasing time of $T_2 \approx 7\mu s$ was used, which was estimated before the actual RB measurements. Beside the main error due to dephasing there are also other sources causing errors, as discussed in Section 3.3. In order to get a reliable theoretical description of the process, an additional, gate-independent error factor of 0.997 94 was introduced such that the simulated average gate error of the standard RB protocol is consistent with the measured value in the case where no additional over-rotation is applied. Although there is an additional offset, the shape of the theoretical fit is in good agreement with the measured curves. This offset probably results from additional, in the simulation not considered, errors of the $(\pi/2)_x$ and $(\pi/2)_y$ gate. However, it is conspicuous that both gates have a bigger error than the average gate error from the standard RB measurement. Since these gates are one of the simplest in the single-qubit Clifford group, the error should lie below the average. Unfortunately, solving this open question was not possible within the time frame of the present thesis. Nevertheless, to get comparable error estimations of different single Clifford gates, we interleave a set of randomized sequences with every element of the group resulting in 24 interleaved RBClifford measurements.

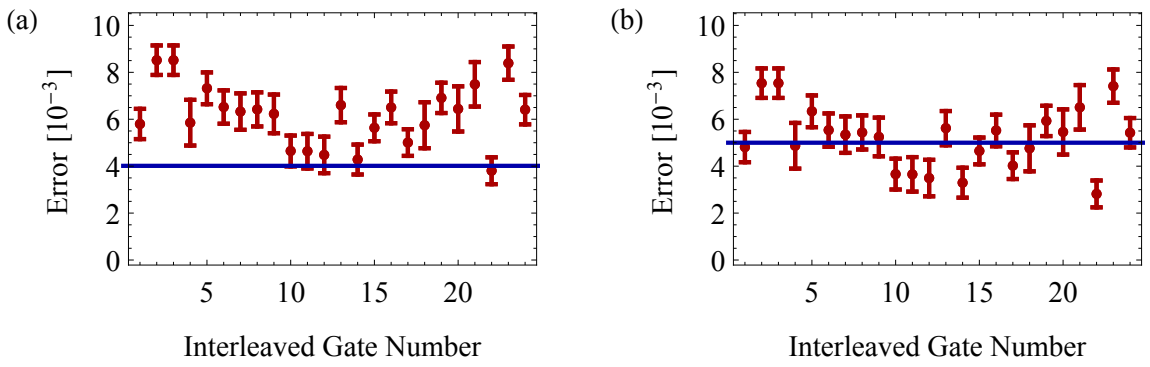

Figure 3.7.: (a) Average gate errors of all gates in the Clifford group estimated with interleaved randomized benchmarking (red). All errors where determined from the average gate error of a single standard RB measurement (blue). **(b)** By changing the estimated average gate error of the standard measurement to about 0.98×10^{-3}, all specific gate errors get slightly shifted such that the average is close to the line of the error from the standard randomized benchmarking

The first set of measurements was with 30 randomized sequences with lengths up to 35 Clifford gates. This maximal length was chosen, because four of the single Clifford gates are composed from three microwave pulses and a interleaved sequence with one of those gates had to fit in the operation time window. Results from this measurement are shown in Figure 3.7(a). Clearly visible, almost all specific gate errors are above the blue line representing the estimated error of the standard measurement. A possible explanation is given by the determination of the specific gate error (Equation 3.24). Then, according to this equation, the gate error is strongly dependent on the parameter p from the standard measurement. Since we had fluctuations in the average gate fidelity of roughly 0.1 %, the specific gate errors might fluctuate even stronger. Assuming only an average gate fidelity of 99.5 % instead of the measured 99.598(47) %, the error line lies closer to the average gate error of all specific gates (Figure 3.7(b)). Despite this error distribution problem, there are still unexplained high errors for single pulse Clifford gates compared to gates based on multiple pulses. Therefore, the fixpoint was again increased to 10.1 µs and the sequences expanded to a maximum sequence length of 84 Clifford gates. Additionally, between each measurement, the qubit transition frequency was rebiased to the parking position. This is necessary, in order to create the same circumstances for every measurement as during the calibration of the single-qubit pulses. The resulting measurements are shown in Figure 3.8 and Figure 3.9. In the first figure, the fitted curves for all measurements are plotted. At the first sight, all interleaved measurements lie close together, which also reveals itself in the closely distributed estimated gate errors of the second figure. A closer look shows that four of the fits are separated by a small gap from the others. As indicated in the figure, these correspond to

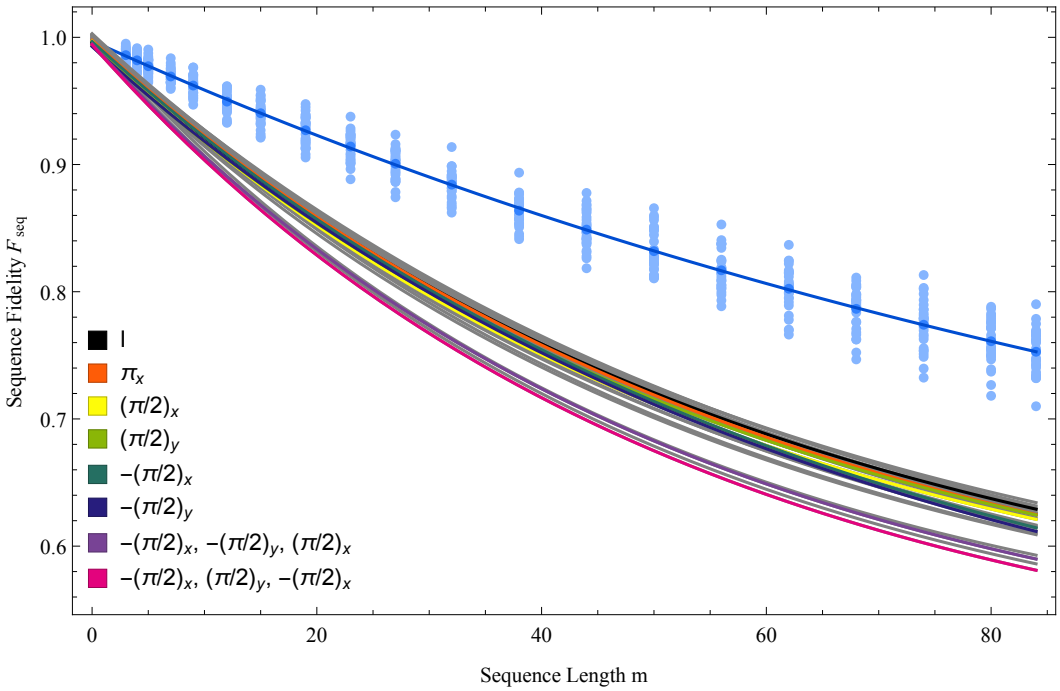

Figure 3.8.: Fitted curves ($F_{seq}(m) = A_0 p^m + B_0$) for 24 interleaved randomized benchmarking measurements, one for every gate in the single Clifford group. The reference measurement (blue) lies clearly above the fidelity fits of the interleaved sequences (gray), of which the ones interleaved with simpler gates such as I, π_x or $(\pi/2)_x$ are closer to the reference curve than more complex ones.

the four Clifford gates consisting of three microwave pulses. Hence, their errors are also higher compared to the other gates in the single-qubit Clifford group. Moreover, gates with just one pulse or less such as the identity operation or the π_x pulse, lie, as expected, below the average gate error. However, since the $-(\pi/2)_x$ and $(\pi/2)_x$, or the $-(\pi/2)_y$ and $(\pi/2)_y$, rotations only differ by a phase shift in the microwave drive pulse, their gate error is expected to be similar.

In a second set of measurements, which took about 10 hours, all errors were estimated again, based on 30 new random sequences, where the order of measurements was reversed such that the interleaved RB measurement with the last gate of the Clifford group was conducted first. The results are shown in Figure 3.10. In contrast to the first set of measurements, all errors are now distributed over a wider range. Moreover, the $-(\pi/2)_x$ and $-(\pi/2)_y$ rotations have the highest error in comparison to the first set of measurements, where they had the smallest error relative to other Clifford group elements. Altogether, all errors are distributed in another fashion. The reasons for this different behavior might lie in fluctuations of the qubit transition frequency, although the qubit transition frequency was set back to the value during calibration after each single measurement. Thus, also systematic errors have to be taken into consideration.

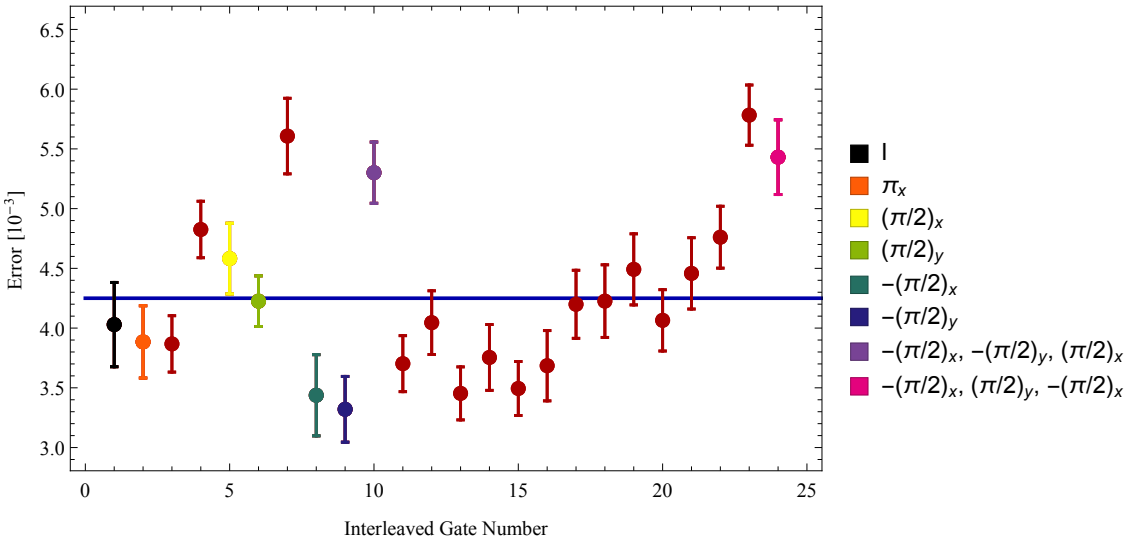

Figure 3.9.: Errors of single-qubit Clifford gates. In the first set of measurements an average gate error of $\epsilon_{ave}^{(0)} = 4.25(12) \times 10^{-3}$ was estimated (blue line). As expected, Clifford gates composed out of three single pulses have an error higher than the single pulses themselves. Nevertheless, also a theoretically unexplained difference between $\pm(\pi/2)_x$ or $\pm(\pi/2)_y$ is observable.

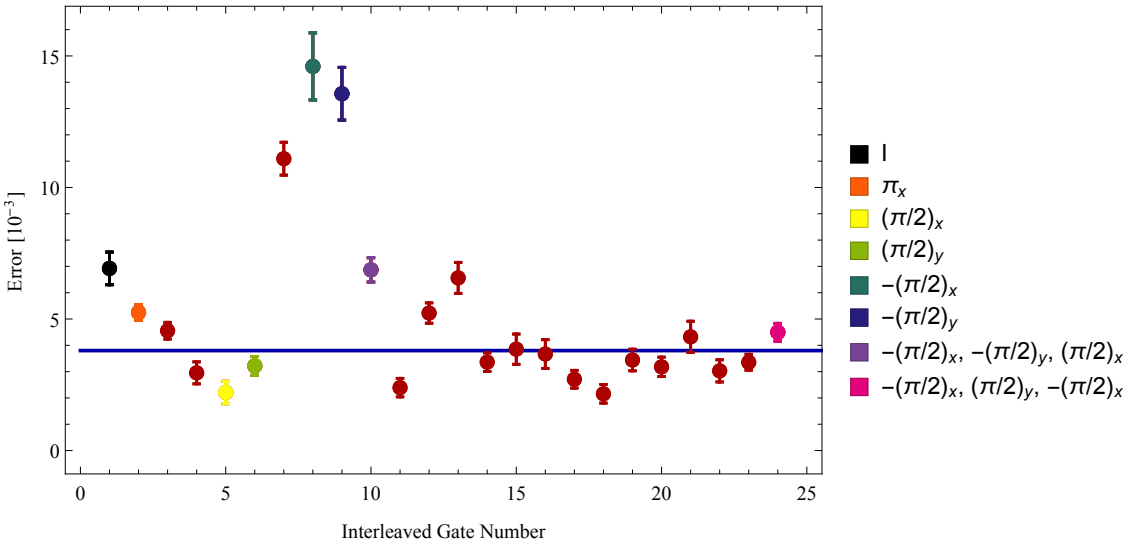

Figure 3.10.: The resulting errors of the single-qubit Clifford group from the second set of measurements are distributed in a different manner than the ones from the first set. Here, especially the $-(\pi/2)_x$ and $-(\pi/2)_y$ gates, whose errors are now unexpected high compared to other errors, achieved a completely different placement among other Clifford gates. The average gate error (blue) was $\epsilon_{ave}^{(0)} = 3.79(17) \times 10^{-3}$

4. Two-Qubit Gates and their Errors

In the interest of performing complex quantum algorithms such as the Shor's algorithms or Lov Grover's search algorithm mentioned in the introduction, the ability to conduct two-qubit gates is a necessary requirement. It is also of great importance that the two-qubit gates are scalable and have low error rates. The goal is to have well calibrated gate blocks, which lead to the same result under any circumstances and do not depend on gates before or after each individual gate. Therefore, QPT is an inefficient tool to characterize the gate errors. By expanding the randomized benchmarking protocol discussed in the previous chapter, we have a scalable method to estimate two-qubit gate fidelities without dependence on SPAM errors.

In the first Section 4.1, we will show how two-qubit gates are realized on superconducting circuits and what kind of possibilities we have. Second, the Clifford group $\mathcal{C}_2$ is introduced in order to expand the randomized benchmarking to two qubits (Sec. 4.2). Before we then come to the actual implementation of the two-qubit controlled-phase gate (Sec. 4.4) and the iSWAP gate (Sec. 4.5) and their errors, the concept of multiplexed and partially tomographic readout is discussed (Sec. 4.3).

4.1. Coupling Superconducting Qubits

Performing two-qubit gates requires an exchange of information between two qubits. For superconducting circuits this is reached by coupling the qubits to a *quantum bus* that allows an energy exchange between them. As we have seen for the dispersive readout, a qubit can be dispersively coupled to a transmission line resonator. It is reasonable to use this coupling to perform gates between two qubits by connecting both to the same resonator. That way, there are two main methods to realize two-qubit gates on transmon qubits. First, by using *sideband transitions* the qubits are allowed to exchange a single photon through the resonator. Second, by tuning qubits into resonance with each other they can exchange a virtual photon. The first one will be briefly discussed in this section followed by a more detailed discussion of the second method, since it is the method that was used to perform two-qubit gates throughout this thesis.

Exchanging quantum information via sideband transitions in circuit QED was first demonstrated experimentally on a flux qubit coupled to a harmonic LC oscillator resonator by Chiorescu et

al. in 2004 [47]. Then it was demonstrated on a CPB qubit coupled to a coplanar waveguide resonator by Wallraff et al. in 2007 [48]. The main idea is to drive the qubit and resonator system at once to reach either simultaneous excitation of qubit and resonator, called *blue sideband*, or an exchange of energy between qubit and resonator (*red sideband*). But, since we are working in the dispersive regime, where the qubits are far detuned from the resonator, such direct transitions are suppressed. However, it is allowed to drive the resonator and the qubit individually with a photon each. Both photons carry the same energy, which is in total equal to the desired sideband transition energy. By applying a pulse first on the red sideband between the first qubit and the resonator followed by a pulse on the sideband between the second qubit and the resonator, it is possible to successfully transmit a photon between two qubits, given a long enough photon lifetime. Unfortunately, a system with such a high Q factor resonator would yield bad readout results, because readout requires relatively short photon lifetimes [49]. Hence, a resonator with different Q factors on different modes is necessary to perform accurate state transitions [39, Chpt. 6.1]. This method brings a few advantages, but also some drawbacks. On one side, the qubits do not need to be tuned out of their parking positions, which are chosen to be optimal in the sense of offering maximal coherence. Also, since there is no need for flux pulses, the qubits are more stable. On the other side, because the two-qubit gates are just controlled by microwave pulses, strong qubit drives are essential. Moreover, in view of the limited operational time due to decoherence, the time required to achieve high-fidelity gates is too long [39, Chpt. 6.1].

Another, much faster, method to implement two-qubit gates is to use magnetic flux pulses. Due to the superconducting loop in the transmon circuit design we are able to tune the transition frequencies of the qubits with the magnetic flux through the loop according to Equation 2.17. Two-qubit gates are then performed by tuning different qubit transition frequencies to a common frequency such that the qubits can exchange virtual photons through the dispersively coupled resonator. To get a mathematical description of this so called *dispersive J-coupling*, consider the Jaynes-Cummings Hamiltonian Eq. 2.21 for the two qubits A and B,

$$\hat{H}_{TC} = \hbar\frac{\omega_A}{2}\sigma_A^z + \hbar\frac{\omega_B}{2}\sigma_B^z + \hbar\omega_r\hat{a}^\dagger\hat{a} + \hbar g_A\left(\hat{a}\sigma_A^+ + \hat{a}^\dagger\sigma_A^-\right) + \hbar g_B\left(\hat{a}\sigma_B^+ + \hat{a}^\dagger\sigma_B^-\right), \tag{4.1}$$

which is often referred to as the *Tavis-Cummings Hamiltonian*. Since the qubits are not directly coupled to each other, there is no qubit-qubit term, solely the coupling term to the resonator of each qubit. Using $e^{\hat{S}}\hat{H}e^{-\hat{S}}$ with $\hat{S} = g_A/\Delta_A(\hat{a}^\dagger\sigma_A^- - \hat{a}\sigma_A^+) + g_B/\Delta_B(\hat{a}^\dagger\sigma_B^- - \hat{a}\sigma_B^+)$, the Hamiltonian is moved into the dispersive regime where $\Delta_A \gg g_A$ and $\Delta_B \gg g_B$. Assuming that the resonator is in the vacuum state and expanding this term up to second order in the small parameter g_i/Δ_i, eliminates all direct excitations between qubit and resonator and yields [35]

$$\hat{H}_{TC,disp} = \hbar\frac{\tilde{\omega_A}}{2}\sigma_A^z + \hbar\frac{\tilde{\omega_B}}{2}\sigma_B^z + \hbar\omega_r\hat{a}^\dagger\hat{a} + J\left(\sigma_A^+\sigma_B^- + \sigma_A^-\sigma_B^+\right) \tag{4.2}$$

where $\tilde{\omega_i} = \omega_i + \chi_i$ is the shifted qubit transition frequency and $J = g_A g_B(\Delta_A + \Delta_B)/(2\Delta_A\Delta_B)$ the J-coupling strength. In a regime where both qubits are far detuned from each other $|\omega_A - \omega_B| \gg J$ the coupling term is not energy conserving. This allows us to turn the interaction on and off by moving in and out of resonance on a nanosecond timescale. Furthermore, using virtual instead of real photons for the coupling results in smaller errors due to avoided cavity-induced losses [50].

With the dispersive J-coupling we are able to implement different two-qubit gates such as the *controlled phase gate (*CPHASE*)* and the *i*SWAP gate (Appendix A.2), whose implementations will be explained in more detail in Section 4.4.1 and 4.5.1. Combining CPHASE, *i*SWAP and single-qubit gates in different ways leads to other useful two-qubit gates like the *controlled NOT gate (*CNOT*)* or the SWAP *gate* (Appendix A.2). In order to estimate the gate errors of those gates, the randomized benchmarking protocol from Section 3.3 has to be expanded to the Clifford group $\mathcal{C}_2$, which contains the CNOT, *i*SWAP and SWAP gate. In 2013 the two-qubit randomized benchmarking was demonstrated on transmon qubits by Córcoles et al. [51], where they have used *cross-resonance* two-qubit interactions to implement all other two-qubit gates. The same approach was also chosen by Barends et al. in 2014 [52] to implement a randomized benchmarking with the CPHASE gate on Xmon qubits. In this thesis we will focus on the two-qubit randomized benchmarking using the CPHASE and the *i*SWAP gate realized with fast magnetic flux pulses.

4.2. The Clifford group $\mathcal{C}_2$

Compared to the single-qubit Clifford group $\mathcal{C}_1$ with 24 elements, the two-qubit Clifford group $\mathcal{C}_2$ contains a larger number of exactly 11 520 elements [51, Suppl.] [52, Suppl.]. For the sake of simplicity, the group is therefore divided into four classes. The *single-qubit class* shown in Figure 4.1(a) is built only out of elements of the single-qubit Clifford group $\mathcal{C}_1$ applied on qubit A and B separately. Thus, this class has $24^2 = 576$ elements. Second, the CNOT*-like class* is created with help of the group $\mathcal{S}_1 = I, R_S, R_S^2$ where R_S is the Pauli transfer matrix of the operator $S = exp[-i(X + Y + Z)\pi/\sqrt{3}3]$ [51, Suppl.]. By implementing these three gates with the single-qubit identity operator and $\pi/2$ pulses around the x and y axis of the Bloch sphere,

$$\begin{aligned} I &\rightarrow I \\ R_S &\rightarrow \left(\frac{\pi}{2}\right)_Y, \left(\frac{\pi}{2}\right)_X \\ R_S^2 &\rightarrow -\left(\frac{\pi}{2}\right)_X, -\left(\frac{\pi}{2}\right)_Y, \end{aligned} \tag{4.3}$$

it is clearly visible that this group simply rotates all three axes of the Bloch sphere. The CNOT-like class is then given by a combination of the single-qubit class, a CNOT gate and the group

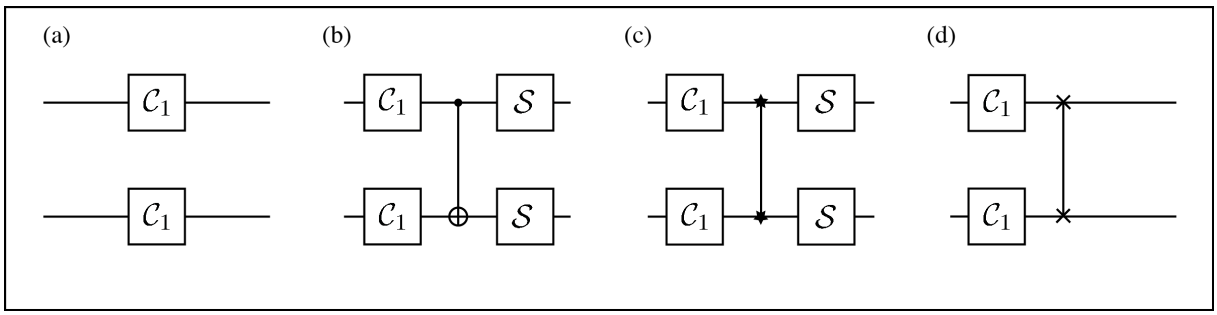

Figure 4.1.: The different classes of the second Clifford group $\mathcal{C}_2$. **(a)** single-qubit class. **(b)** CNOT-like class. **(c)** iSWAP-like class. **(d)** SWAP-like class.

S_1 applied on both qubits (Figure 4.1(b)). With all possible combinations this class counts $24^2 \cdot 3^2 = 5184$ elements. The third class is the iSWAP-*like class* and it is in principle just the CNOT-like class with an iSWAP gate instead of a CNOT gate (Figure 4.1(c)). Hence, it also contains 5184 elements. Last, the SWAP-*like class* has $24^2 = 576$ elements. It is a combination of the single-qubit class with a SWAP gate (Figure 4.1(d)).

As we have seen, the basic two-qubit gates of $\mathcal{C}_2$ are the CNOT, the iSWAP and the SWAP gate. There are many ways how to realize these gates. Either direct or out of a combination of single-qubit pulses and physically realizable two-qubit gates. In the end, it is desirable to have a low average gate number per Clifford gate. Then in such a case, the gate fidelity will also be lower, since every additional gate degrades the overall gate error. In this sense, it is also obvious that the expected average gate fidelity of two-qubit gates is lower than the average gate fidelity of single-qubit gates. Choosing our generating set, for example, to be the CPHASE gate and the single-qubit gates from the group $\{I, \pm(\pi/2)_X, \pm(\pi/2)_Y, \pm\pi_X, \pm\pi_Y\}$, the CNOT, iSWAP and SWAP gates are constructed from 1, 2 and 3 CPHASE gates respectively, resulting in an average number of 1.5 CPHASE gates per Clifford gate.

Before we now further discuss the CPHASE and iSWAP gate and randomized benchmarking with them, the concept of multiplexed and tomographic readout has to be understood. These methods are necessary to properly estimate the fidelity of sequences with two-qubit gates, as we will see in the next section.

4.3. Multiplexed and Partially Tomographic Readout

A non-demolition readout of qubit states is possible due to the dispersive shift of the resonator frequency, as we have seen earlier. In case of two or multiple qubits the resonator is shifted depending on the state of each qubit i by a frequency difference $\pm\chi_i$ allowing multiqubit read-

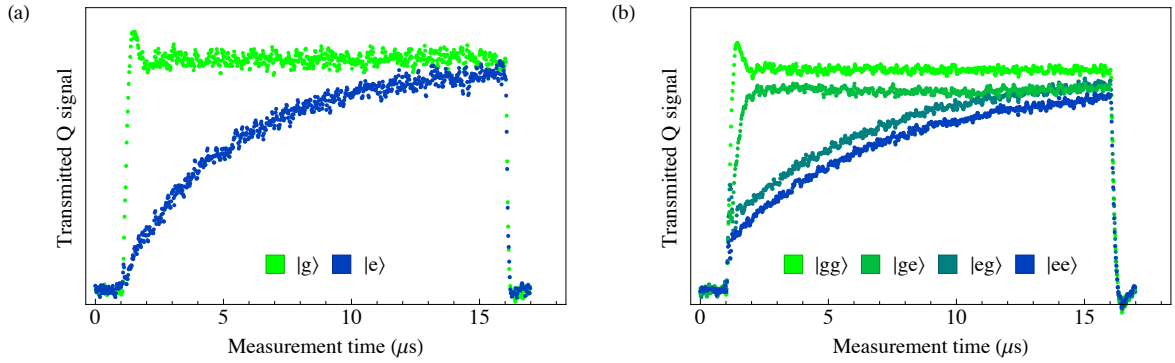

Figure 4.2.: (a) Quadrature of the resonator response measured in transmission when one qubit is prepared in the ground (green dots) and excited (blue dots) states for a measurement tone switched on at t =1 ns for 15 µs. **(b)** As in panel (a) but when preparing all computational two-qubit states $|gg\rangle, |ge\rangle, |eg\rangle$ and $|ee\rangle$.

out [50]. In this thesis we will focus on two qubits and a resonator frequency of $\omega_r - \chi_A - \chi_B$, which corresponds to a state where both qubits are in the ground state. After all operations on the qubits are finished and the qubits are ready for readout, a measurement tone with this frequency is switched on. According to the general measurement process explained in Section 2.6, the transmitted signal is decomposed in time-dependent in-phase I and quadrature Q components, where the phase is chosen such that the Q quadrature carries most of the signal. Because both quadratures depend non-linearly on the dispersive shift operator $\hat{\chi} = \chi\hat{\sigma}^z$, they behave differently over time for qubits in the ground or excited state [39, Chpt. 3.2]. In Figure 4.2, typical measurement resonator responses for single-qubit (a) and a two-qubit (b) readout are shown. For each trace, the qubits were prepared in another combination of ground and excited state leading to $|g\rangle$ and $|e\rangle$ state traces and $|gg\rangle, |ge\rangle, |eg\rangle$ and $|ee\rangle$ traces in the two-qubit case. When the qubits are in the ground state and the system is on resonance with the measurement tone, an instant exponential rise of the transmitted Q quadrature is observable. In the other case, when the qubits are in the excited states, the resonator is driven off-resonantly resulting in a damped signal. Over time, this signal convergences towards the ground state signal due to relaxation. Note that the smooth shape of the trace is obtained by averaging over 18×10^3 measurements. A single measurement usually contains abrupt jumps, since the qubit states relax by spontaneous emission [53].

Theoretically, the measurement process is represented by the two measurement operators $\hat{M}_I$ and $\hat{M}_Q$ by

$$I(t), Q(t) = \langle \hat{M}_{I,Q} \rangle = Tr[\rho \hat{M}_{I,Q}] \tag{4.4}$$

where ρ is the prepared qubit state. Both operators can be predicted by the *Lindblad master equation*, which describes the dynamics of the qubit-resonator system under consideration of

dissipation and dephasing [54]. For simplicity, we focus on the Q quadrature term in further calculations, since, in our convention, it does contain more information than the I quadrature. By reason of the non-demolition property of the dispersive readout, these two operators are diagonal:

$$\hat{M} = \alpha_{gg} |gg\rangle \langle g| + \alpha_{ge} |ge\rangle \langle ge| + \alpha_{eg} |eg\rangle \langle eg| + \alpha_{ee} |ee\rangle \langle ee| , \tag{4.5}$$

with α_{ij} denoting the state-dependent quadrature amplitudes. They are estimated by adding four calibration sequences, prepearing the states $|gg\rangle, |ge\rangle, |eg\rangle, |ee\rangle$, after each measurement. The parameter α is replaced with the difference of the response for the qubit state $|ij\rangle \langle ij|$ to the ground state response integrated from $t = 0$ to the final time T [55]

$$\alpha_{ij} = \frac{1}{N} \int_0^T \left(Tr \left[|ij\rangle \langle ij| \hat{M} \right] - Tr \left[|gg\rangle \langle gg| \hat{M} \right] \right) \mathrm{d}t \tag{4.6}$$

Furthermore, if the normalization constant is chosen such that $\alpha_{ee} = 1$, the efficient measurement operator is represented by

$$\hat{M} = \begin{pmatrix} 0 & 0 & 0 & 0 \\ 0 & \alpha_{ge} & 0 & 0 \\ 0 & 0 & \alpha_{eg} & 0 \\ 0 & 0 & 0 & 1 \end{pmatrix} \tag{4.7}$$

In this convention, a measurement of a state ρ yields

$$\langle \hat{M} \rangle = Tr[\rho \hat{M}] = \alpha_{ge} \langle ge| \rho |ge\rangle + \alpha_{eg} \langle eg| \rho |eg\rangle + \langle ee| \rho |ee\rangle \tag{4.8}$$

where $\langle ij| \rho |ij\rangle$ is the probability that the system described by ρ is in the $|ij\rangle$ state. Considering only one qubit, the measurement operator reduces to a projective measurement of whether the qubit is in the excited state described by the operator $\hat{M} = |e\rangle \langle e|$. Hence, it directly returns the probability of being in the excited state. After applying single-qubit randomized benchmarking sequences to a qubit initially prepared in the ground state, the probability of being in the ground state is then easily estimated by one minus the probability to be in the excited state. As we can see from Equation 4.8, estimating the probability of returning to the ground state for the two-qubit case is not trivial.

A method to estimate the ground state population of a two-qubit state is to perform a partial tomography measurement. It is based on the principle that every quantum state can be written as a linear combination of a complete set of basis states. Because every two-qubit quantum state can be expressed by a complex 4×4 positive semidefinite and hermitian density matrix with trace one, there are at least 16 linear independent basis states. Thus, a complete tomography measurement rotates the state before measurement into 16 different states to estimate every coefficient of the linear combination leading to the exact description of the state. In our case, we are only interested in the diagonal states $|gg\rangle, |ge\rangle, |eg\rangle$ and $|ee\rangle$ of the unknown state. By

choosing $\{\mathbb{1}\otimes\mathbb{1},\ \mathbb{1}\otimes\sigma^x,\ \sigma^x\otimes\mathbb{1},\ \sigma^x\otimes\sigma^x\}$ as a set of rotations and measuring the state after each rotation results in four equations with four unknown parameters

$$\begin{aligned}
\langle\hat{M}_{\mathbb{1}\otimes\mathbb{1}}\rangle &= \alpha_{gg}\langle gg|\,\rho\,|gg\rangle + \alpha_{ge}\langle ge|\,\rho\,|ge\rangle + \alpha_{eg}\langle eg|\,\rho\,|eg\rangle + \alpha_{ee}\langle ee|\,\rho\,|ee\rangle \\
\langle\hat{M}_{\mathbb{1}\otimes\sigma^x}\rangle &= \alpha_{ge}\langle gg|\,\rho\,|gg\rangle + \alpha_{gg}\langle ge|\,\rho\,|ge\rangle + \alpha_{ee}\langle eg|\,\rho\,|eg\rangle + \alpha_{eg}\langle ee|\,\rho\,|ee\rangle \\
\langle\hat{M}_{\sigma^x\otimes\mathbb{1}}\rangle &= \alpha_{eg}\langle gg|\,\rho\,|gg\rangle + \alpha_{ee}\langle ge|\,\rho\,|ge\rangle + \alpha_{gg}\langle eg|\,\rho\,|eg\rangle + \alpha_{ge}\langle ee|\,\rho\,|ee\rangle \\
\langle\hat{M}_{\sigma^x\otimes\sigma^x}\rangle &= \alpha_{ee}\langle gg|\,\rho\,|gg\rangle + \alpha_{eg}\langle ge|\,\rho\,|ge\rangle + \alpha_{ge}\langle eg|\,\rho\,|eg\rangle + \alpha_{gg}\langle ee|\,\rho\,|ee\rangle
\end{aligned} \tag{4.9}$$

Here, instead of the unknown state we rotated the measurement operator according to

$$Tr[U\rho U^\dagger\hat{M}] = Tr[\rho U^\dagger\hat{M}U] = \langle\hat{M}_U\rangle \tag{4.10}$$

Solving for all diagonal elements of the unknown density operator, the desired ground state population $\langle gg|\,\rho\,|gg\rangle$ is extracted. A more detailed discussion of two-qubit state tomography based on joint dispersive readout can be found in Ref. [55].

4.4. CPHASE Gate

One of the main purposes of this thesis is to deliver a tool to estimate the error of the CPHASE gate implemented by using fast magnetic flux pulses. Before we start discussing randomized benchmarking with the CPHASE gate (Section 4.4.4), it is important to understand the realization of the gate itself. In this sense, we will first explain how the previous discussed J coupling is used to create a CPHASE gate (Section 4.4.1). Additionally, before starting error estimations of a gate, one has to deal with its proper calibration (Section 4.4.2 and 4.4.3). Otherwise, the outcome of a randomized benchmarking experiment (Sec. 4.4.4) would lead to no reliable approximation of the real error. Finally, Section 4.4.5 presents the interleaved randomized benchmarking with the CPHASE gate.

4.4.1. Coupling to Second Excited State

The previously derived Tavis-Cummings Hamiltonain in the dispersive limit given by Eq. 4.2 is restricted to a two level system. This makes perfect sense, since our computational qubit space has also just two levels. Yet, it is still a physical system and other levels may be considered as well in order to achieve more complex quantum gates. This is exactly the case for the CPHASE gate that was theoretically proposed by Strauch et al. in 2003 [56]. Considering an energy level

$|f\rangle$ outside the computational basis of $|g\rangle$ and $|e\rangle$, the coupling term in Eq. 4.2 expands to

$$\begin{aligned} &J_{gg}(|g\rangle\langle e|_A|e\rangle\langle g|_B + |e\rangle\langle g|_A|g\rangle\langle e|_B) \\ +&J_{ge}(|g\rangle\langle e|_A|f\rangle\langle e|_B + |e\rangle\langle g|_A|e\rangle\langle f|_B) \\ +&J_{eg}(|e\rangle\langle f|_A|e\rangle\langle g|_B + |f\rangle\langle e|_A|g\rangle\langle e|_B) \\ +&J_{ee}(|e\rangle\langle f|_A|f\rangle\langle e|_B + |f\rangle\langle e|_A|e\rangle\langle f|_B) \end{aligned} \tag{4.11}$$

where the first line corresponds to the coupling in the two-level case. What is now visible in this representation, the two terms with coupling strengths J_{ge} and J_{eg} allow a coupling of the $|ee\rangle$ state to the $|gf\rangle$ or $|fg\rangle$ states. Assuming that the system is well isolated from environment, this transition is only possible when the $g \leftrightarrow e$ transition frequency of one qubit is equal to the $e \leftrightarrow f$ transition frequency of the other qubit. In that case, the gained energy quantum from the $e \leftrightarrow g$ transition is absorbed by the second qubit to transfer to the $|f\rangle$ state. Due to the second terms of the coupling J_{ge} and J_{eg} in Eq. 4.11, the coupling is symmetric. Hence, we can focus on one case and all results will also apply vice versa. Sweeping the $g \leftrightarrow e$ transition frequency of an excited qubit A to the $e \leftrightarrow f$ frequency of an excited qubit B, reveals an avoided crossing between the states [57]. At this point, the degeneracy is shifted by a frequency proportional to the J_{ge} coupling strength. As soon as the states are tuned to the same frequency, the system starts to oscillate between those states according to [56]

$$|\Phi(t)\rangle = e^{-itH}|\Phi\rangle = \cos(J_{ge}t)|ee\rangle + i\sin(J_{ge}t)|fg\rangle \tag{4.12}$$

After a time of $t = \pi/J_{ge}$ the system returns back to the $|ee\rangle$ state with an additional phase π. Due to this process, the $|ee\rangle$ state is multiplied with a factor of -1, where, at the same time, all other states are left unchanged. This corresponds to the CPHASE gate

$$U_{\text{CPHASE}} = \begin{pmatrix} 1 & 0 & 0 & 0 \\ 0 & 1 & 0 & 0 \\ 0 & 0 & 1 & 0 \\ 0 & 0 & 0 & -1 \end{pmatrix}. \tag{4.13}$$

In practice, there are a few additional points one has to consider. Once, a qubit is tuned out of its rotating reference frame, its frequency has changed. When the qubit is then tuned back, the rotation of the qubit is phase-shifted compared to the initial rotating reference frame. However, this phase shift is only collected by a qubit in the excited state. Therefore, the process is described by the *phase gate* operator

$$R_\phi = \begin{pmatrix} 1 & 0 \\ 0 & e^{i\phi} \end{pmatrix} \tag{4.14}$$

where the phase shift ϕ is given by the integrated detuning in frequency space over time $\phi = \int \Delta\omega(t)\,\mathrm{d}t$. Even in the case when the $g \leftrightarrow e$ and $e \leftrightarrow f$ transition frequencies of the two qubits

differ from each other, the time-dependent qubit frequency $\omega(t)$ is influenced by the frequency shift from the avoided crossing. Denoting this frequency shift by ζ, the actual introduced phase is given by $\phi = \phi_A - \int\zeta(t)\,\mathrm{d}t$, where ϕ_A is the phase created by the detuning assuming no avoided crossing. Additionally, due to flux crosstalk, a detuning of one qubit causes a small detuning on the second qubit, represented by ϕ_B. Taking all considerations together, the actual CPHASE operator between qubit A and B is given by [57]

$$U_{\text{CPHASE},\,eff} = \begin{pmatrix} 1 & 0 & 0 & 0 \\ 0 & e^{i\phi_B} & 0 & 0 \\ 0 & 0 & e^{i\phi_A} & 0 \\ 0 & 0 & 0 & e^{i\phi_{AB}} \end{pmatrix} \tag{4.15}$$

where $\phi_{AB} = \phi_A + \phi_B - \int\zeta(t)\,\mathrm{d}t$. The CPHASE gate Eq. 4.13 is achieved by a qubit detuning such that $\int\zeta(t)\,\mathrm{d}t = (2n+1)\pi$ and $\phi_A,\ \phi_B = 2\pi n$. It therefore plays an important role, how the qubit detuning or the amplitude of the flux pulse proceeds over time. To accomplish a CPHASE gate with a high fidelity, the optimal shape of the flux pulse has to be approximated by several calibration measurements.

4.4.2. Interaction Position and Timing

A first step in finding the optimal flux pulse shape for the CPHASE gate, is to estimate the right amplitude and duration of the pulse. The so called *interaction amplitude* of the flux pulse corresponds to the voltage that the AWG applies to the magnetic flux line of qubit A which detunes the $g \leftrightarrow e$ transition frequency to the $e \leftrightarrow f$ transition frequency of another qubit B. The *interaction length* is the time the pulse stays at the interaction amplitude before it decreases again. Theoretically, this corresponds to a time $t = \pi/J_{ge}$, as mentioned in Section 4.4.1.

The rough approximation of the optimal combination of interaction amplitude and length is estimated with a simple calibration measurement (Fig. 4.3). By applying a π_x microwave pulse on each qubit, the system is excited to the $|ee\rangle$ state. With a subsequent squared flux pulse of varying amplitude and length an oscillation between the excited qubit state and the $|gf\rangle$ state is produced. Afterwards, another $\pi_x \otimes \pi_x$ gate is applied on the qubits. If a flux pulse with the correct amplitude and length is chosen, the qubits will end up, as expected from the CPHASE, in the ground state

$$\begin{pmatrix} 1 \\ 0 \\ 0 \\ 0 \end{pmatrix} \xrightarrow{\pi_x \otimes \pi_x} \begin{pmatrix} 0 \\ 0 \\ 0 \\ -1 \end{pmatrix} \xrightarrow{U_{\text{CPHASE},eff}} \begin{pmatrix} 0 \\ 0 \\ 0 \\ -e^{i\phi_{AB}} \end{pmatrix} \xrightarrow{\pi_x \otimes \pi_x} \begin{pmatrix} e^{i\phi_{AB}} \\ 0 \\ 0 \\ 0 \end{pmatrix} \tag{4.16}$$

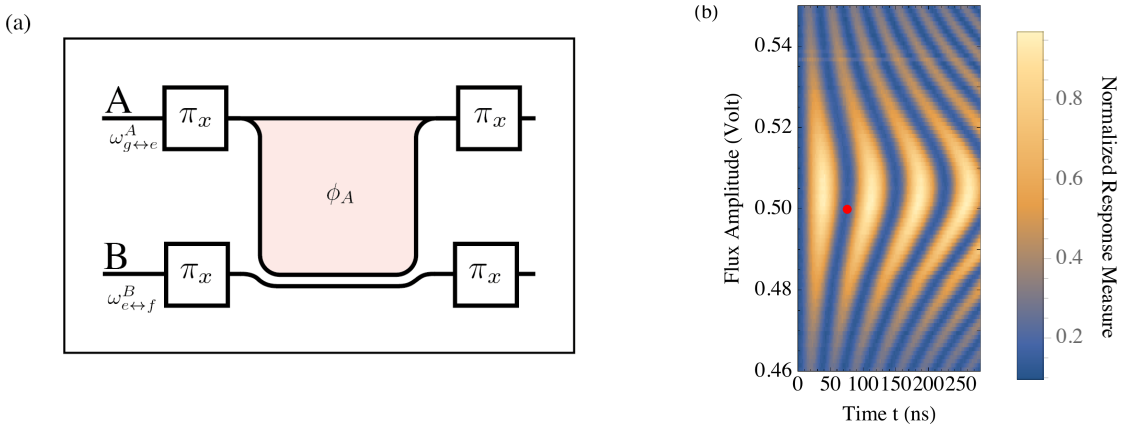

Figure 4.3.: (a) A CPHASE gate is implemented by tuning the $\omega^A_{g\leftrightarrow e}$ transition frequency of qubit A to the $\omega^B_{e\leftrightarrow f}$ frequency of qubit B, where A picks up a phase ϕ_A. By applying a pulse scheme, consisting of a $\pi_x \otimes \pi_x$ gate before and after the flux pulse, on the ground state $|gg\rangle$, different populations are expected for varying amplitude and length of the flux pulse. **(b)** Here, the closeness of the measured resonator response to the ground $|gg\rangle = 0$ and excited state $|ee\rangle = 1$ response is shown (see text). An ideal combination in the sense of achieving a CPHASE gate leads back to the $|gg\rangle$ state. The used combination is indicated by a red point.

The more the amplitude and length of the pulse deviate from the optimal values, the more of the qubit population will be lost in the $|gf\rangle$ state. A typical outcome of such a calibration measurement is shown in Figure 4.3(a), where the flux pulse amplitude and length applied on qubit 1 were swept from 0.46 V to 0.55 V and 0 ns to 280 ns respectively, in order to achieve a CPHASE gate between qubits 1 and 2. To distinguish between the $|gg\rangle$ and $|ee\rangle$ states, we take the difference between each observed readout trace $\langle M(t)\rangle$ and the reference readout trace when the qubits are in the ground state $\langle M_{gg}(t)\rangle$ and compute the normalized inner product with the difference $\langle M_{ee}(t) - M_{gg}(t)\rangle$ between the reference responses for the $|ee\rangle$ and $|gg\rangle$ states respectively. In this measure, a value of one corresponds to a qubit population in the excited state $|ee\rangle$. One speaks of the resulting landscape as *Chevron pattern*. In the Chevron pattern obtained in our lab Fig. 4.3(b) the optimal point for the CPHASE lies in the second "valley" from the right, indicated by the red point. The restriction to the second "valley" is in no way arbitrary. To achieve an additional phase factor of -1 the qubit population has to be moved to the $|gf\rangle$ state and back, which excludes the first "valley". Hence, in the interest of possessing as short gates as possible, the optimal values lie in the second "valley". However, this method only delivers a rough guess of the interaction amplitude and length, since it does not provide a calibration of the phase ϕ_{AB}.

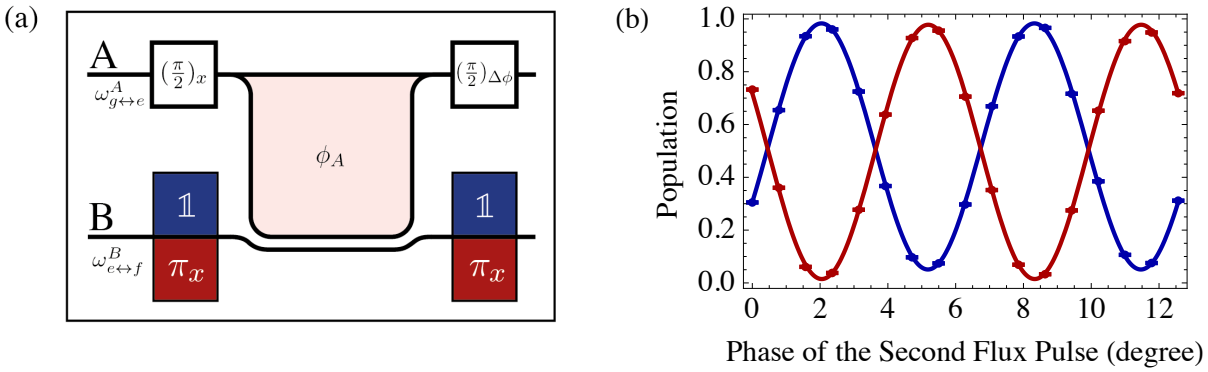

Figure 4.4.: (a) Pulse scheme for the RelPhase calibration, where we apply a $(\pi/2)_x$ pulse before and a phase shifted $(\pi/2)_{\Delta\phi}$ pulse after a CPHASE flux pulse, similar to Fig. 4.3(a), on qubit A. At the same time qubit B is either left in the ground state (unity $\mathbb{1}$)(blue box) or brought to the excited state with a π_x pulse (red box). **(b)** Resulting oscillations between the $|gg\rangle$ and $|eg\rangle$ state for increasing phase difference $\Delta\phi$ with a phase shift dependent on whether qubit B is in the excited state (red) or not (blue). If the optimal flux amplitude and length for a CPHASE is reached, the relative phase shift is $\pi/2$. In this measurement the relative phase offset was 0.55°.

A more accurate estimation of the interaction amplitude and length is offered by the *relative phase (RelPhase)* measurement (Fig. 4.4). In contrast to the Chevron pattern measurement, the Relphase protocol also takes the phase ϕ_{AB} into account. It is a Ramsey-type measurement, consisting of two parts. In the first part the gate $(\pi/2)_x \otimes \mathbb{1}$ is applied before the CPHASE pulse and the $(\pi/2)_{\Delta\phi} \otimes \mathbb{1}$ gate afterwards, where the second $\pi/2$ pulse on qubit A is shifted by a phase $\Delta\phi$ compared to the first (Fig. 4.4(a)). Since during this pulse sequence, qubit B is always in the ground state, no conditional phase shift is observable. Moreover, the resulting two-qubit state is dependent on $\Delta\phi$ and oscillates between the $|gg\rangle$ and $|eg\rangle$ (blue points in Fig. 4.4(b)). In the second part, with the rotation $(\pi/2)_x \otimes \pi_x$ qubit B is brought to the excited state before the CPHASE gate is applied and afterwards back to the ground state by $(\pi/2)_{\Delta\phi} \otimes \pi_x$ (Fig. 4.4(a)). Similar to the first part, an oscillation between $|gg\rangle$ and $|eg\rangle$ for varying $\Delta\phi$ is detectable (red points in Fig 4.4(b)). However, due to the CPHASE gate and its conditional phase shift of the $|ee\rangle$ state, the two sinusoidal oscillations are in the ideal case phase shifted by $\pi/2$. To estimate the optimal interaction amplitude and length, this Ramsey-type experiment is conducted several times, where each time the amplitude or length of the flux pulse is changed. In contrast to the Chevron measurement, the parameters are swept over a much smaller range. The specific measurement shown in Fig 4.4(b) corresponds to a relative phase offset of 0.55°. It is one of 16 measurement where the pulse amplitude and length were varied 5 times between $-0.004\,\mathrm{V}$ and

0.004 V and 11 times between −5 ns and 5 ns respectively. By the use of the RelPhase method ideal pulse parameters of 0.507 V and 74.97 ns could be determined (indicated by the red dot in Fig. 4.3(b)).

4.4.3. Dynamic Phase Correction

Up to now, the interaction amplitude and length of the CPHASE gate is calibrated such that we gain an additional phase factor of −1 when the qubits are in the $|ee\rangle$ state. Thus, the CPHASE gate after a RelPhase calibration takes the form

$$U'_{\text{CPHASE}} = \begin{pmatrix} 1 & 0 & 0 & 0 \\ 0 & e^{i\phi_B} & 0 & 0 \\ 0 & 0 & e^{i\phi_A} & 0 \\ 0 & 0 & 0 & -e^{i\phi_A + i\phi_B} \end{pmatrix} \tag{4.17}$$

Since the dynamic phase ϕ_B qubit B picks up during a detuning of qubit A is very small compared to ϕ_A, it can, for the moment, be neglected. Therefore, the next calibration step includes determination and optimization of the dynamic phase ϕ_A.

An adjustment of the dynamic phase is accomplished by applying an additional phase gate given by Eq. 4.14 to the qubit. As mentioned, this is simply done by tuning the qubit out of its reference frequency with a flux pulse. For that reason, the initial, squared flux pulse shape is expanded by two *buffers* at the rising and falling edge of the pulse (Fig. 4.5(a)). The new shape allows a modification of the integrated area of the detuning without changing the amplitude and length of the interaction. Moreover, the buffers help to suppress an over and undershoot of the flux pulse amplitude, since the intermediate step prevents a rapid change of the amplitude.

With the new introduced buffers, there are four possibilities to tune the area of the flux pulse, because each buffer has its own amplitude and length. Nonetheless, we are only interested in the final dynamic phase of qubit A, which only requires calibration of one parameter. In our case, we kept the length of both buffers fixed at 10 ns as well as the amplitude of the buffer in the falling edge, called "buffer after", at roughly 50 % of the interaction amplitude. The only sweeping parameter is therefore the amplitude of the buffer in the rising edge ("buffer before"). With the pulse scheme illustrated in Fig. 4.5(a), where we rotate qubit A from the ground state to the XY plane, apply a CPHASE gate and rotate it back to the ground state, the "buffer before" amplitude can be calibrated. Assuming that the CPHASE gate is given by U'_{CPHASE} the resulting

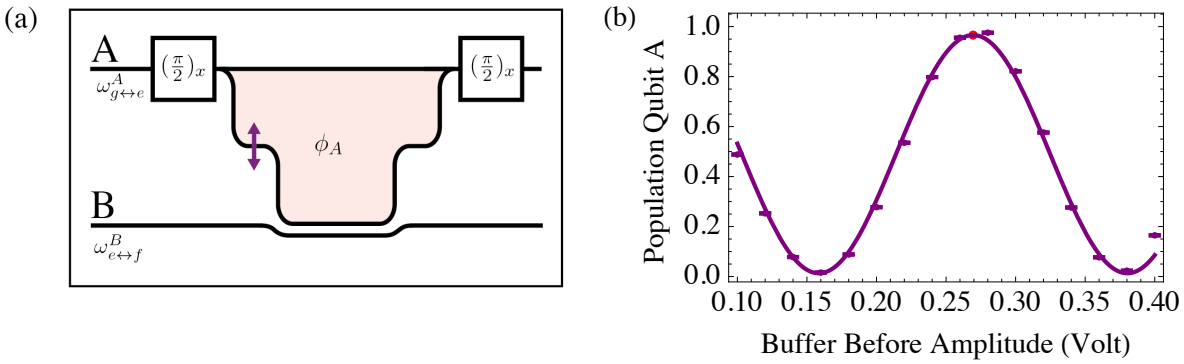

Figure 4.5.: Dynamic phase calibration of the CPHASE gate. **(a)** Two $(\pi/2)_x$ gates are applied to the qubit, on which a flux pulse with a buffer at the rising and falling edge is performed in between. The flux pulse detunes the $\omega^A_{g\leftrightarrow e}$ transition frequency of qubit A to the $\omega^B_{e\leftrightarrow f}$ transition frequency of qubit B. **(b)** Varying the amplitude of the "buffer before", the interaction yields an oscillation of the qubit state between the $|gg\rangle$ and $|eg\rangle$ state. An optimal CPHASE is achieved when the qubit ends up in the $|eg\rangle$ state, here indicated by the red dot.

qubit state is then

$$\begin{pmatrix} 1 \\ 0 \\ 0 \\ 0 \end{pmatrix} \xrightarrow{(\pi/2)_x \otimes \mathbb{1}} \frac{1}{\sqrt{2}} \begin{pmatrix} 1 \\ 0 \\ -i \\ 0 \end{pmatrix} \xrightarrow{U'_{\text{CPHASE}}} \frac{1}{\sqrt{2}} \begin{pmatrix} 1 \\ 0 \\ -ie^{i\phi_A} \\ 0 \end{pmatrix} \xrightarrow{(\pi/2)_x \otimes \mathbb{1}} \frac{1}{2} \begin{pmatrix} 1 - e^{i\phi_A} \\ 0 \\ -i(1 + e^{i\phi_A}) \\ 0 \end{pmatrix} \tag{4.18}$$

Clearly visible from this derivation, an oscillation between the $|gg\rangle$ and the $|eg\rangle$ state is expected when sweeping the phase ϕ_A. By identifying the buffer amplitude which leads to an $|eg\rangle$ state, gives us a well calibrated CPHASE pulse, since then the phase factor is one ($e^{i\phi_A} = 1$).

4.4.4. Randomized Benchmarking with the CPHASE

The goal behind a randomized benchmarking with the CPHASE gate is primarily to estimate the error of the CPHASE itself. It is therefore consistent to express the whole Clifford group in terms of the CPHASE gate (Fig. 4.6). The same approach was also used in research to estimate the fidelity of the cross-resonance two-qubit gate [51] or the fidelity of the CPHASE gate on Xmon qubits [52]. In comparison to the single-qubit Clifford group, where individual gate lengths varied between 21 ns to 63 ns, a Clifford gate from the two-qubit group may have lengths in between 21 ns and $\approx$ 580 ns assuming a CPHASE gate length of $\approx$ 130 ns. In the worst case, a sequence of 10 gates is already longer than the set fixed point of 4.1 µs (see Section 3.3). Hence, as in the single-qubit

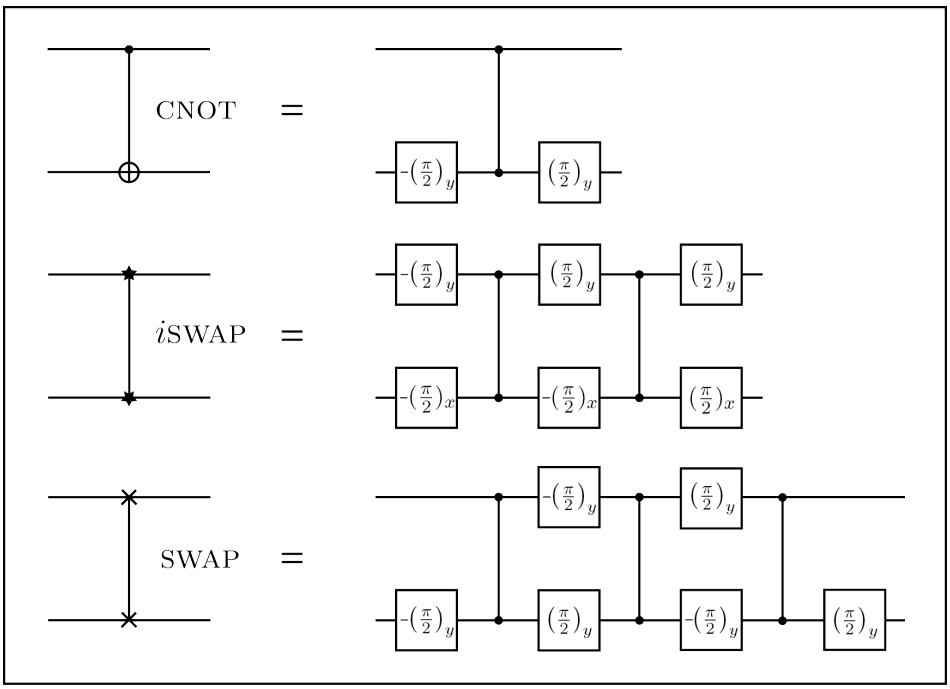

Figure 4.6.: Expressing important elements in the Clifford group C_2, such as the CNOT, the iSWAP and the SWAP, in terms of the two-qubit CPHASE gate and single-qubit unitarities. The gates are applied from left to right.

case, the fixed point is set to 10.1 µs, which allows even in the worst case sequences of more than 15 Clifford gates. A limitation of the two-qubit RB is also given by the total number of sequences. In order to get a reliable readout of the ground state population, the resulting qubit state has to be rotated with one of the four pulses $\{\mathbb{1} \otimes \mathbb{1},\ \mathbb{1} \otimes \sigma^x,\ \sigma^x \otimes \mathbb{1},\ \sigma^x \otimes \sigma^x\}$ after each sequence separately (Section 4.3). With the usual number of 850 sample points per sequence, the maximal allowed number of sequences is 153, which restricts the amount of truncation lengths to 5 when we want to generate 30 randomized sequences. Thus, the measurement time was shortened to 5 µs to increase the maximal number of sequences to $2^{19}/500 = 1048$. Unfortunately, creating such an amount of long sequences exceeds the memory of the AWGs. A good trade-off was found with 25 randomized sequences truncated to smaller sequences with lenghts of 1, 2, 3, 4, 5, 6, 8 and 10 gates.

In Figure 4.7(a), the resulting sequence fidelities of a randomized benchmarking with the CPHASE gate are shown. Clearly visible, the sequence fidelities are distributed over a larger range as in the singe-qubit case. This is not surprising, since some of the Clifford gates, like gates from the SWAP class, are composed out of three CPHASE pulses and some simply out of a few single microwave pulses. Assuming a CPHASE gate fidelity of $\approx 90\,\%$, already a combination of two SWAP-like gates will roughly lead to a sequence fidelity of $0.9^6 \approx 0.53$ excluding single-qubit

gate errors. Furthermore, a convergence of the sequence fidelities towards 25 % is observable. In contrast to the single-qubit case, where the completely mixed state is either projected as $|g\rangle$ or $|e\rangle$ state when measured, the measured two-qubit completely mixed state can be projected onto the $|gg\rangle, |ge\rangle, |eg\rangle$ or $|ee\rangle$ state. Thus, there is a 25 % probability that the dephasing error brings the state back to the $|gg\rangle$ state. By fitting a model considering gate and time-independent errors Eq. 3.17 to the estimated mean points for every sequence length, leads to an average gate fidelity of $F_{ave}^{(0)} = 90.91(193)\,\%$. At this point it makes no sense to compare gate and time-dependence of the errors, since the fit of five parameters to a set of 8 points does not provide a reliable estimation of the fidelity. With regard to common used values of 40 [51] or even 100 [52] randomized sequences, the experiment was conducted several times to receive more data points for every sequence length. Through this repeated measurements an interesting property of our implemented CPHASE gate was revealed (Fig. 4.7(b)). Measuring the average gate fidelity of the CPHASE gate right after the standard calibration process yields higher values than after a few minutes. Here, the standard calibration measurement includes three RelPhase measurements with 9×10^3 averages each and a calibration of the "buffer before" (DynPhase) with 18×10^3 averages repeated twice. It seems that the calibration of the CPHASE gets lost over time, even though both qubit frequencies were rebiased to their initial values after each RB measurement of ≈ 30 min. Therefore, only data points from the three measurements right after calibration were taken to determine more averaged mean points for every sequence length (Fig. 4.7(c)). In total, this gives us 75 data points per length and leads to an average gate fidelity of $F_{ave}^{(0)} = 92.089(1484)\,\%$. Note that with this representation of the Clifford group we have 1.5 CPHASE gates on average for every Clifford gate. Therefore, the fidelity of the CPHASE gate is expected to be above 92 %.

To further examine the error of the CPHASE gate, there is an additional method to restrict its fidelity. If we, during sequence generation, only take two-qubit gates from the CNOT class of the Clifford group, the RB method will give us the average fidelity of gates containing only one CPHASE gate. However, the CNOT class is not a group by itself and therefore the final gate does not have to be an element of this class. The average gate fidelity then just provides a lower limit of the CPHASE fidelity, because most of the excluded gates consist of more than one CPHASE gate. Such a restricted measurement is shown in Figure 4.8(a). The estimated average sequence fidelity of $F_{ave}^{(0)} = 94.28(155)\,\%$ is, as assumed, higher than the same average over the whole Clifford group. Thus, we carefully increase the expected CPHASE fidelity to above 94 %.

To demonstrate the approach of restricting the pool of chosen Clifford gates once more, we restrict the set of gates to the single-qubit and CNOT class together. As the single-qubit gates have fidelities in the 99 % regime, the new restricted set should reach an even higher average gate fidelity. As predicted, the fitted curve in Figure 4.8(b) leads to a average gate fidelity of $F_{ave}^{(0)} = 96.26(84)\,\%$.

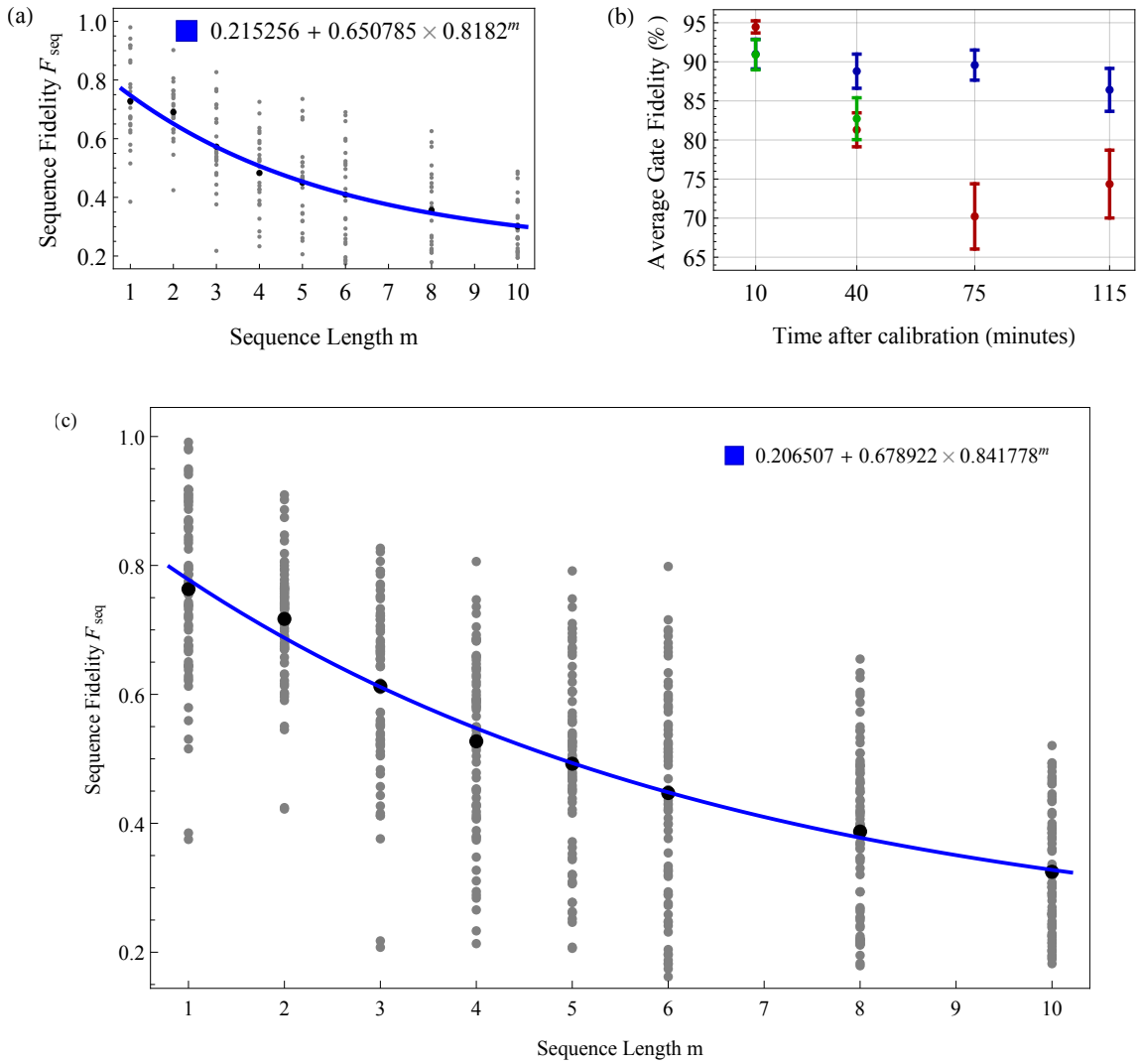

Figure 4.7.: Standard randomized benchmarking of two-qubit gates with the Clifford group in terms of the CPHASE gate. **(a)** Single set of RB measurements with 25 sequence fidelity points at each length. The points are spread over a large range due to the different compositions of the Clifford gates. With the fitted parameter $p = 0.8182$, an average gate fidelity of $F_{ave}^{(0)} = 90.91(193)\,\%$ was reached. **(b)** Conducting several sets of RB measurements after a calibration of the CPHASE gate (RelPhase, DynPhase) a decreasing tendency of the average gate fidelity is observable. During all measurements with the same color the same set of random sequences was used. **(c)** Using the sequence fidelities of the three RB measurements directly after calibration, where each time another set of randomized sequences was used, a more accurate estimation of the average sequence fidelity was achieved. According to the time and gate-dependent fit function the Clifford group has an average gate fidelity of $F_{ave}^{(0)} = 92.089(1484)\,\%$.

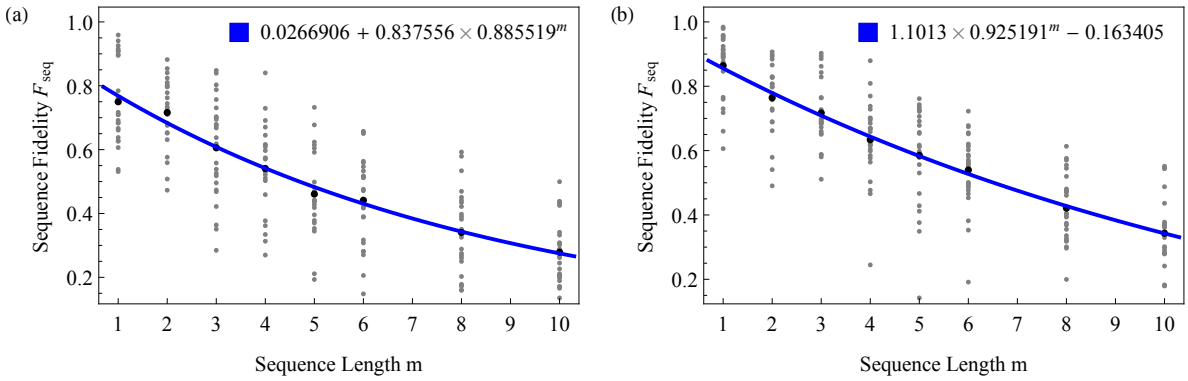

Figure 4.8.: If the pool of gates for the generation of random sequences is restricted to the CNOT class **(a)** or the single-qubit and CNOT class together **(b)**, higher average gate fidelities are expected. Despite the fact that it is not a proper estimation of the average gate errors, since the final gate might still be in another Clifford class, the measured values of $F_{ave}^{(0)} = 94.28(155)\,\%$ and $F_{ave}^{(0)} = 96.26(84)\,\%$ respectively are consistent with the assumptions.

Even though these results must be interpreted with caution, they in some sense prove our theoretical assumptions about the errors of different Clifford classes. A more reliable estimation of the CPHASE gate fidelity is made with the interleaved randomized benchmarking protocol shown in the next section.

4.4.5. Interleaved Randomized Benchmarking with the CPHASE

The Interleaved randomized benchmarking (Section 3.4) provides a helpful tool to estimate the specific error of the CPHASE gate. In order to check if the method works, the sequences were first interleaved with the $\pi_x \otimes \pi_x$ gate from the single-qubit class. Compared to the average gate fidelity of the second Clifford group, the single Clifford gates have higher expected average fidelity (Section 3.3). This should therefore lead to a gate fidelity clearly above the average value. To get an a reliable estimation, the same interleaved sequences were measured five times each after a standard calibration process as described in Section 4.4.4. The different determined gate fidelities are shown in Figure 4.9(a). They fluctuate in between $97.02(168)\,\%$ and $99.71(177)\,\%$, but are all clearly above the average gate fidelity of the Clifford group $\mathcal{C}_2$. Taking all five measurements together, which gives 125 data points per length, and average over these, brings us to the mean points for every length presented in Figure 4.9(c) (purple). Fitting a time and gate-independent decay model to the new estimated mean points results in a gate fidelity of $98.571(3115)\,\%$. The standard RB measurement, which was taken as a reference, is represented by the blue points and fit.

In the next step, the same set of sequences was interleaved with a single CNOT gate. It is the most comparable gate to the CPHASE gate, since it only includes two additional singe-qubit pulses (Fig. 4.6). As well as the $\pi_x \otimes \pi_x$ gate the CNOT gate belongs to the simpler gates of the Clifford group in terms of the CPHASE, and should lead to a fidelity slightly above the average gate fidelity. However, the resulting fidelities, shown in Figure 4.9(b), fluctuate in a large range between fidelities of 61.71(47) % and 89.09(139) %, of which all values are below the average gate fidelity. Adding data points together, where a fidelity of over 75 % was reached to exclude possible systematic errors, a measurement-averaged gate fidelity is extracted, as in the case before. Through this method, a fidelity of 85.644(3115) % for the CNOT gate was determined. Against expectation, this result does not coincide with the approximated lower limit. Moreover, with the same calibration methods used, several quantum process tomography measurements lead to a fidelity over 89.51 %. Possible reasons for the observed fluctuations during the single measurements and the low fidelity can be explained with qubit frequency fluctuations, despite the fact that the qubits were still rebiased after each measurement. The effect might also be caused by the fast decrease of the sequence fidelity, since the base of the exponential fit is more or less just estimated from the first few sequence lengths and is therefore more sensitive to fluctuations.

In a first approximation, we have neglected the additional phase ϕ_B on qubit B. Aiming towards two-qubit gates with high fidelity, it is also worth taking this phase into consideration. The phase of the second qubit B can be compensated by introducing a phase gate on qubit B. If the length of this flux pulse is fixed, the amplitude can be swept until the phase disappears $\phi_B = 2\pi n$. It is, however, important that the flux pulse on the second qubit is not conducted during the interaction time of the initial CPHASE pulse, since it affects the frequency of qubit B and shifts the interaction position. The calibration process can be realized by applying the pulse $\mathbb{1} \otimes (\pi/2)_x$ before and $\mathbb{1} \otimes -(\pi/2)_x$ after the flux pulses. According to the consequent oscillations between the $|gg\rangle$ and $|eg\rangle$ states, where an ideal CPHASE leads to the ground state, the optimal amplitude is determined. Sadly, the effects of the additional calibration were not investigated in this thesis, because no flux line was connected to qubit 2 and the unknown malfunctioning of the CPHASE gate between other qubits. It might be an interesting topic for further studies of the CPHASE gate.

4.5. iSWAP Gate

Let us now come to the last part of this thesis, the error estimation of the *i*SWAP gate with randomized benchmarking. Like the CPHASE gate it is implemented with fast magnetic flux pulses. How this works will be explained in the first Section 4.5.1. Then, we give an overview of the calibration of the *i*SWAP gate in Sections 4.5.2 and 4.5.3. In the last section, we discuss

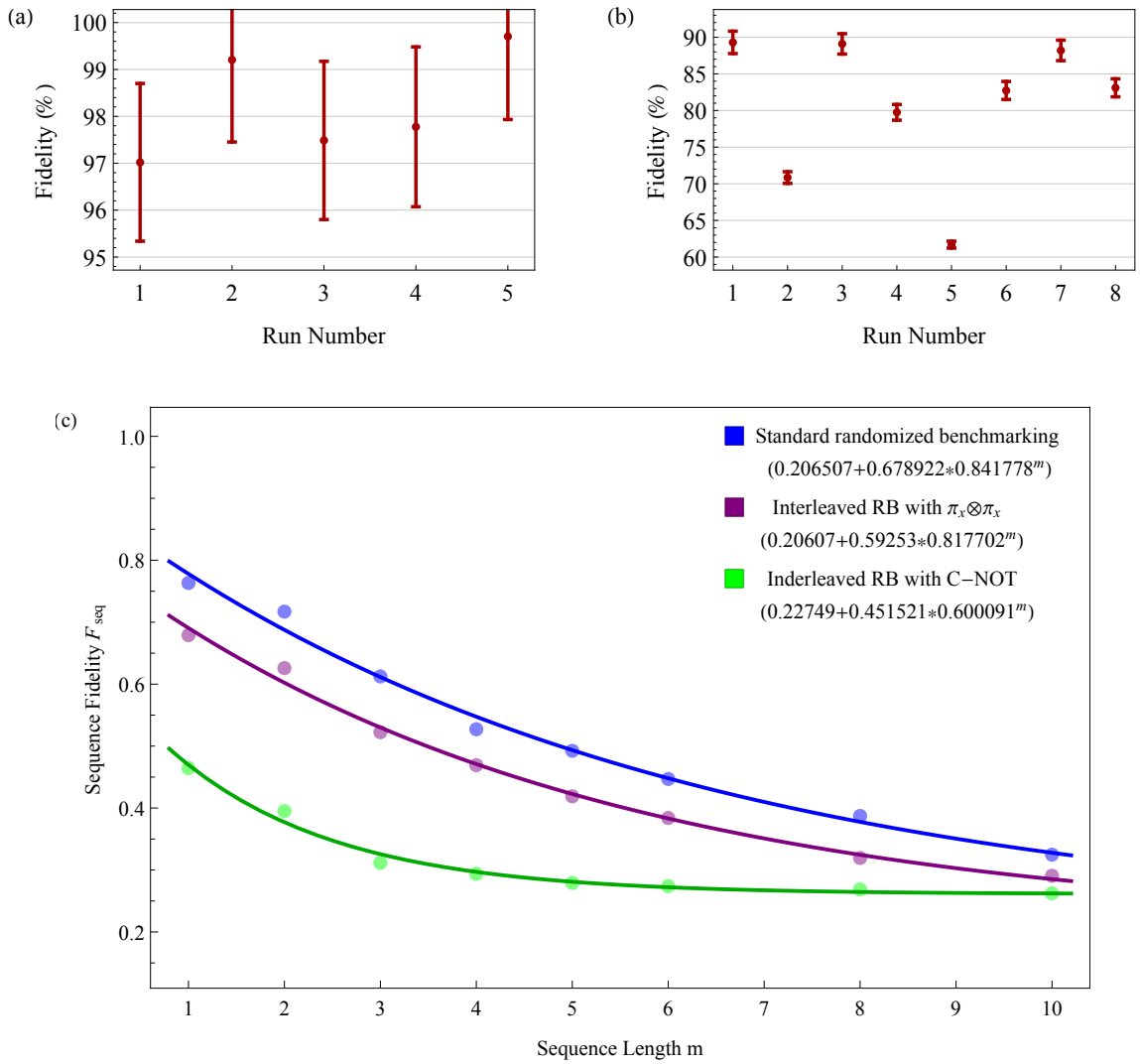

Figure 4.9.: Interleaved randomized benchmarking with the $\pi_x \otimes \pi_x$ and CNOT gate. **(a)** Fluctuations in the fidelity of the $\pi_x \otimes \pi_x$ gate over different interleaved RB measurements. In each run, the same set of sequences was measured right after calibration. **(b)** Heavy fluctuations were observed during different interleaved RB measurements for estimating the fidelity of the CNOT gate, although in every run the same set of sequences was measured directly after calibration. **(c)** Mean sequence fidelities and fit as a function of sequence length for the standard RB (blue) and the two interleaved RBs (purple and green). The points and fit of the standard RB were taken from the assembled measurement shown in Figure 4.7. In the same way the mean sequence fidelities of the interleaved RBs were accumulated. The determined gate fidelities are 98.571(3115) % for the $\pi_x \otimes \pi_x$ gate and 85.644(3115) % for the CNOT gate.

the implementation of randomized benchmarking with the *i*SWAP and the obtained unexpected low average gate fidelities.

4.5.1. XY Coupling

Beside the coupling to the second excited states, the Travis-Cummings Hamiltonian in the dispersive limit Eq. 4.2 has another interesting coupling term, the *XY coupling*. Rewriting the coupling from Eq. 4.2 in terms of qubit states $|g\rangle$ and $|e\rangle$ yields

$$J_{gg}(|g\rangle\langle e|_A |e\rangle\langle g|_B + |e\rangle\langle g|_A |g\rangle\langle e|_B) \tag{4.19}$$

Through this term, the Hamiltonian allows an exchange of virtual photons between two qubits, when the transition frequencies of both qubits are equal. By tuning the $\omega^A_{g\leftrightarrow e}$ transition frequency of a qubit A to the one of a second qubit B such that $\left|\omega^A_{g\leftrightarrow e} - \omega^B_{g\leftrightarrow e}\right| = 0$, the time dependent interaction Hamiltonian is represented by [56]

$$\mathcal{H}_{int}(t) = e^{-it\mathcal{H}_{int}} = \begin{pmatrix} 1 & 0 & 0 & 0 \\ 0 & \cos(J_{gg}t) & i\sin(J_{gg}t) & \\ 0 & i\sin(J_{gg}t) & \cos(J_{gg}t) & 0 \\ 0 & 0 & 0 & 1 \end{pmatrix} \tag{4.20}$$

Due to this term, the system then starts to oscillate between the $|ge\rangle$ and $|eg\rangle$ state. A complete swapping of those states such that both pick up a phase factor i is achieved when the qubits are in resonance over a time of $t = \pi/2J_{gg}$. In this case, the resulting action corresponds to the one described by the *i*SWAP gate

$$U_{i\text{SWAP}} = \begin{pmatrix} 1 & 0 & 0 & 0 \\ 0 & 0 & i & 0 \\ 0 & i & 0 & 0 \\ 0 & 0 & 0 & 1 \end{pmatrix} \tag{4.21}$$

As simple as it may seem, there are further aspects concerning the implementation of a *i*SWAP gate. First of all, since one of the qubits has to be detuned from its rotating reference frame, it picks up an additional phase. Note that in consideration of the symmetry of the Hamiltonian, it does not matter which of the qubits is detuned. As described in Section 4.4.1, this additional phase is taken into account by a phase gate Eq. 4.14. Second, because the *i*SWAP gate swaps the states $|ge\rangle$ and $|eg\rangle$ and both qubits have different rotating reference frames, the state transferred to qubit A has been in another reference frame before. This means that this state has picked up a phase ϕ_{rel} according to the area between both qubits in frequency space from $t = 0$ until the swapping of states takes place (Fig. 4.10(a)). Due to the same reasons the state which has been swapped from qubit A to qubit B gains also an additional phase ϕ_{rel} corresponding to this

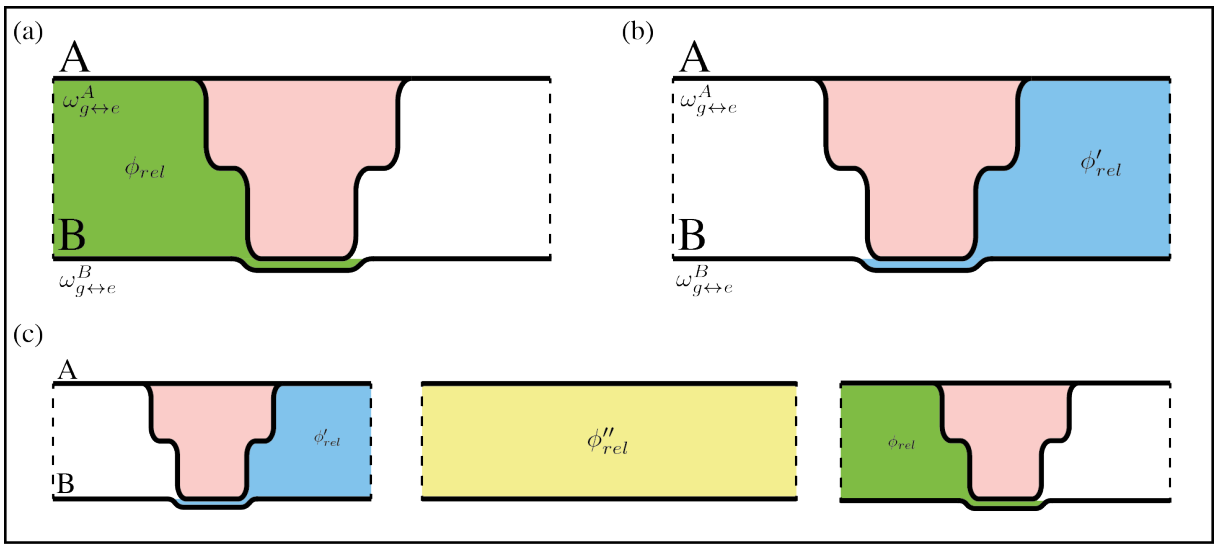

Figure 4.10.: Illustration of the three different dynamical phases that need to be considered when implementing the *i*SWAP gate. **(a)** When the *i*SWAP gate swaps the $|ge\rangle$ and $|eg\rangle$ states, the phase ϕ_{rel} (green area) indicates the phase shift the states pick up in view of the other qubit reference frame. **(b)** In order to achieve well calibrated *i*SWAP blocks, the phase afterwards ϕ'_{rel} (blue area) does already account for the following *i*SWAP gate. **(c)** Additionally, also the time gap in between two *i*SWAP gates does accumulate a phase ϕ''_{rel} (yellow area).

area. Moreover, aiming towards scalable *i*SWAP gates one has to consider the area between the qubit reference frames after the pulse (Fig. 4.10(b)). This area accumulates a phase ϕ'_{rel} for both qubits and is therefore important for the next state swapping by the succeeding *i*SWAP gate. In order to built independent *i*SWAP *blocks* it is important to calibrate the buffers of the *i*SWAP such that for each block from $t = 0$ to $t = T$ we have $\phi_{rel} + \phi'_{rel} = 2\pi n$ for positive integers $n \in \mathbb{N}^+$. In consideration of the first *i*SWAP gate it is also necessary to have $\phi_{rel} = 2\pi m$ where $m \in \mathbb{N}^+$. Finally, as soon as two *i*SWAP gates are not applied directly after each other, a third phase factor appears (Fig. 4.10(c)). This phase ϕ''_{rel} depends on the distance in time of the two *i*SWAP blocks and contributes to the other phases. Hence, we need

$$\phi_{rel} = 2\pi n, \qquad \phi_{rel} + \phi'_{rel} + \phi''_{rel} = 2\pi m \tag{4.22}$$

with $n, m \in \mathbb{N}^+$.

4.5.2. Interaction Position and Timing

Before we start to calibrate the buffers of the flux pulse, the interaction amplitude and length have to be estimated properly. A from the relative phases independent protocol is given by the

one showed in Figure 4.11(a). Here, two π_x gates are applied on qubit A before and after the iSWAP flux pulse. The first microwave pulse brings qubit A to the excited state $|eg\rangle$. After the iSWAP gate has swapped both qubit states $|eg\rangle \rightarrow i\,|ge\rangle$, the second π pulse excites the swapped ground state, $i\,|ge\rangle \rightarrow |ee\rangle$. If the iSWAP does not exchange the states suitably, the second single-qubit gate will bring the remaining excitation back to the ground state. As a consequence, an oscillation between the $|gg\rangle$ and $|ee\rangle$ states is detectable. Hence, sweeping the interaction amplitude and length of the flux pulse will lead to a similar Chevron pattern as for the CPHASE gate shown in Figure 4.3(b). In contrast to the CPHASE gate calibration, we are now interested in the coordinates of the first "summit" of such a landscape. Also different for the calibration of the iSWAP is that there is no need for a second interaction parameter calibration [58]. As soon as a swapping of the qubit states with the above protocol is achieved, the amplitude and the length of the pulse is already well calibrated.

To get an iSWAP gate with high fidelity, the maximum of the Chevron pattern landscape has to be estimated with high accuracy. Instead of decreasing the step-size and estimating the optimal combination of amplitude and length in a time-consuming, detailed sweep, we make use of the gradient-free numeric optimization algorithm called *Nelder-Mead* [59, 60]. It starts with measuring the qubit population of three points on a 2D plain that is spanned by amplitude and length parameters. Then, depending on the reached populations, three new points are determined: the center of gravity of the initial triangle, the reflection of the worst value by the line between the other two points and another point in the same direction but further away. In the next run the values of the new points are estimated and a new triangle is formed out of the best two values from the run before and the best values of the actual run. The Nelder-Mead algorithm is repeated as many times needed so that the difference in population of the triangle points falls below a certain threshold. For the calibration of iSWAP gates throughout this thesis, 15 calibration steps were enough to accurately estimate the interaction amplitude and length of the flux pulse. In each step the measurements were averaged 18×10^3 times. One of those calibrations is shown in Figure 4.11(b-f).

4.5.3. Relative Phase Corrections

After the determination of the correct interaction amplitude and length, the next step is to correct the relative phases ϕ_{rel}, ϕ'_{rel} and ϕ''_{rel}. As mentioned above, the goal is to have calibrated iSWAP blocks, which can be randomly combined with single-qubit gates or other two-qubit gates. It is therefore not convenient to adjust the "buffer before", which is equal to a modulation of the phase ϕ_{rel}, according to $\phi_{rel} + \phi'_{rel} + \phi''_{rel} = 2\pi m$ every time an iSWAP is used. Instead we split this requirement in three smaller conditions

$$\phi_{rel} = 2\pi n, \qquad \phi'_{rel} = 2\pi m \quad \textit{and} \quad \phi''_{rel} = 2\pi k \tag{4.23}$$

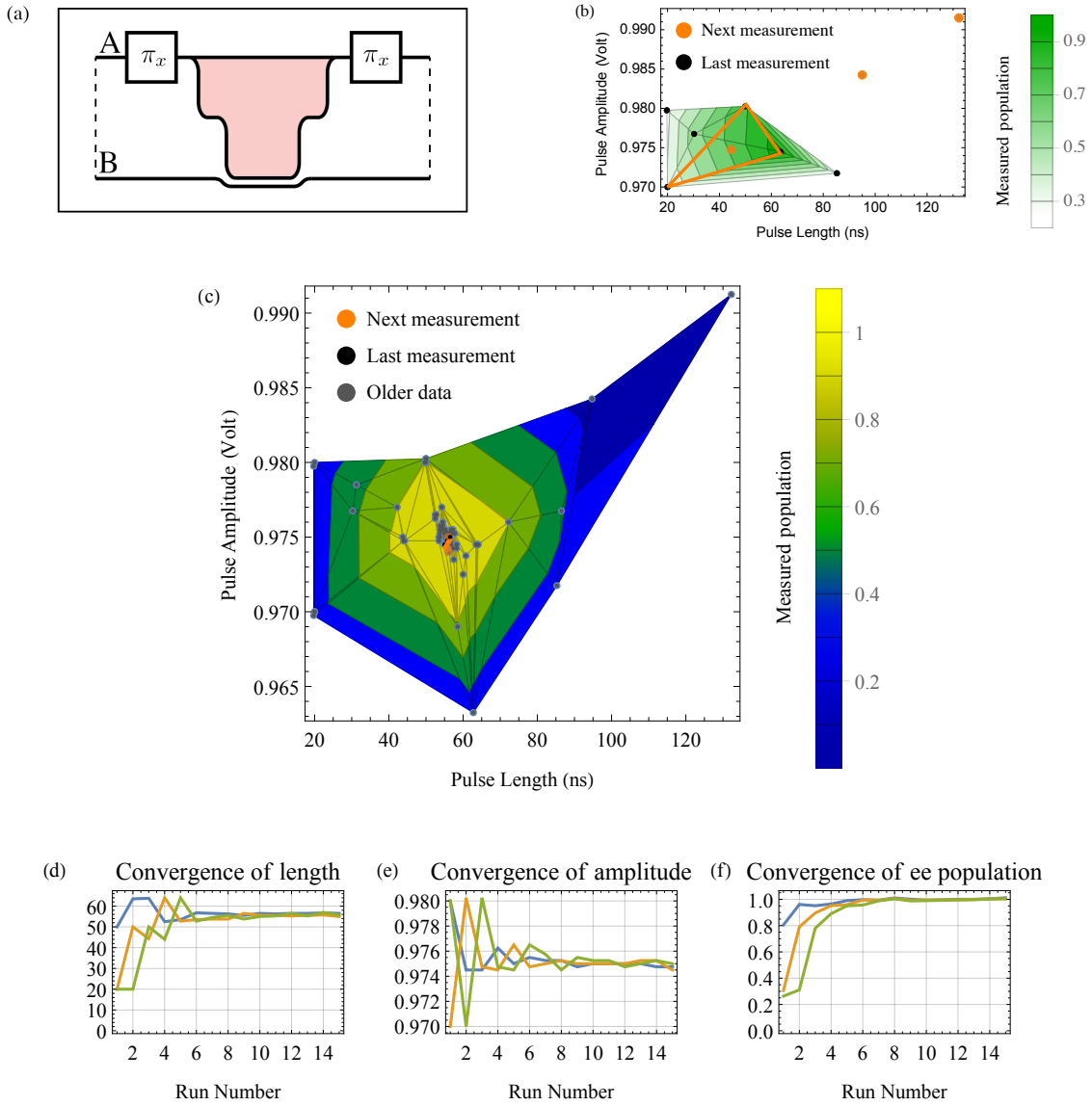

Figure 4.11.: Calibration of the *i*SWAP pulse interaction amplitude and interaction length. **(a)** Pulse scheme for the calibration. This protocol is not influenced by effects of the buffers, therefore the standard value of roughly of 50 % the interaction amplitude was used. **(b)** A single Nelder-Mead algorithm step. The chosen triangle and the calculated coordinate points for the next measurement are highlighted in orange. **(c)** The estimated final contour plot of the Chevron pattern landscape after 15 algorithm steps. The colors indicate the measured excited state population $|ee\rangle$ (yellow) in contrast to the ground state population $|gg\rangle$ (blue). **(d)** History of the length parameters with the resulting convergence in qubit population. **(e)** Evolution of the amplitude parameter. **(f)** Convergence of $|ee\rangle$.

where $n, m, k \in \mathbb{N}^+$. Then, the iSWAP gates can be arbitrarily combined with other gates into sequences under the condition that the length of the other gates is such that the acquired relative phase is a multiple of 2π.

First, we calibrate ϕ_{rel}. This is done by sweeping the amplitude of a buffer with fixed length of 10 ns at the rising edge of the flux pulse. The area between the frequency of qubit A and the steady state frequency of qubit B before the swapping (Fig. 4.10) leads to a phase shift that the state of qubit A receives after the swap. Hence, a well calibrated "buffer before" amplitude eliminates the resulting phase $\phi_{rel} = 2\pi n$ on qubit B. The calibration protocol consists of a $(\pi/2)_x \otimes \mathbb{1}$ and $\mathbb{1} \otimes (\pi/2)_y$ pulse, applied before and after the flux pulse respectively. Through this combination the second part of the superposition state $1/\sqrt{2}(|gg\rangle + |eg\rangle)$ is swapped with an additional phase shift $1/\sqrt{2}(|gg\rangle + i\,|ge\rangle)$, before it gets excited to the $|ge\rangle$ state by the $(\pi/2)_y$ pulse on qubit B. If the iSWAP gate swapping works but the phase is calibrated wrong we end up in the $|gg\rangle$ state. Hence, similar to the calibration of the CPHASE buffer (Fig. 4.5), this protocol leads to an oscillation between the $|gg\rangle$ and the $|ge\rangle$ state depending on the buffer level, where the optimal buffer amplitude corresponds to a maximal population of the state $|ge\rangle$.

Second, the phase ϕ'_{rel} is important to get a proper iSWAP block without any additional phases on qubit A. In the rotating frame of qubit A, the area between the reference frames before the pulse (Fig. 4.10(a)) can also be seen as a accumulated phase of the state it receives after the swap. Since the amplitude of the "buffer before" is now fixed, the shape of the "buffer after" the pulse is the only parameter to correct the resulting phase shift. As before, we keep the buffer at a length of 10 ns and sweep the amplitude. Flipping the $\pi/2$ pulses of the previous protocol such that we have $\mathbb{1} \otimes (\pi/2)_x$ before and $(\pi/2)_x \otimes \mathbb{1}$ afterwards, an oscillation between $|gg\rangle$ and $|eg\rangle$ depending on the second buffer amplitude is accomplished. Here, observing a maximal $|eg\rangle$ state population corresponds to the condition $\phi'_{rel} = 2\pi m$.

Finally, after both buffers are calibrated, we only have to compensate for ϕ''_{rel}. This is only necessary when more than one iSWAP gate is included in the same measurement sequence. Assuming that we just have microwave pulses in between the iSWAP gates, the only parameter to change the area between the two qubit reference frames is the time (Fig. 4.10(c)). When the time is exactly equal to a multiple of the period of the reference frequency

$$k \cdot T_{rel} = \frac{k}{\left| f^A_{g\leftrightarrow e} - f^B_{g\leftrightarrow e} \right|} \tag{4.24}$$

where $f_{g\leftrightarrow e} = \omega_{g\leftrightarrow e}/2\pi$, the condition $\phi''_{rel} = 2\pi k$ is always fulfilled. However, due to the 1 GS/s sampling rate of the AWG, it is just possible to change the amplitude of a flux pulse in nanosecond bins. If the qubit transition frequencies are, for example, 5.359 GHz and 4.823 GHz, the time in between iSWAP gates has to be a multiple of $T_{rel} = 1.865\,671\,642$ ns. In such a case, there are two ways to achieve a disappearing relative phase. Either one expands the duration

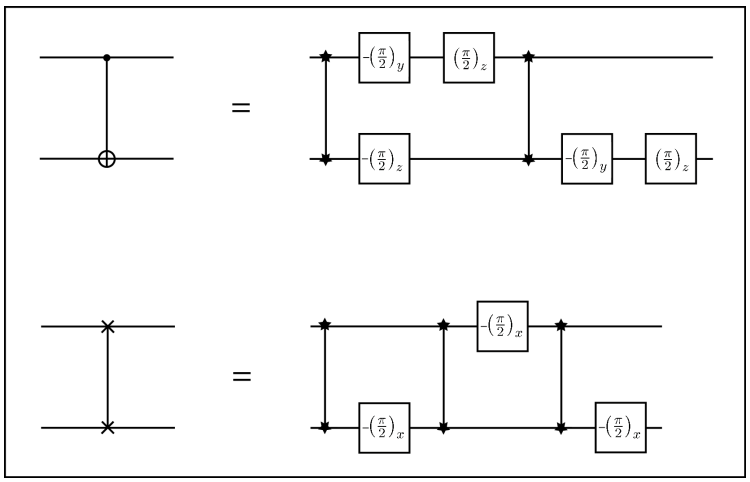

Figure 4.12.: The CNOT gate and the SWAP gate expressed in terms of *i*SWAP gates and single-qubit microwave pulses. In order to conduct a randomized benchmarking with the *i*SWAP the whole Clifford group has to be represented by *i*SWAP gates.

of the sequence between the *i*SWAP pulses such that it is equal to an integer multiple of the T_{rel} time, or the qubit frequencies are changed in a way that the T_{rel} becomes an integer itself.

4.5.4. Randomized Benchmarking with iSWAP

Similar to the randomized benchmarking with the CPHASE gate, we express the CNOT and the SWAP gate in terms of the *i*SWAP gate as illustrated in Figure 4.12 [61]. Through these, we are able to express the two-qubit Clifford group with the *i*SWAP gate. But, in contrast to the CPHASE case, we have to consider the timing between two *i*SWAPs in each Clifford gate, as well as the timing between two Clifford gates including *i*SWAPs. To overcome theses problems, we defined a new *i*SWAP block that contains an additional spacer of a microwave pulse length after the *i*SWAP pulse. By calibrating the buffers of the *i*SWAP gate inside the new gate block, we automatically include the compensation of the acquired relative phase. Thus, the new blocks can be combined independently as before, with the difference that we have the opportunity to also include a single-qubit microwave pulse. This allows us to represent the SWAP gate in terms of three new *i*SWAP blocks (see Fig. 4.12).

However, there is still a timing conflict in the construction of the CNOT gate and for the scalability of gates from the single-qubit class. Both of those problems are solved setting the difference between the frequency of Q1 and Q2 to 531.25 MHz such that T_{rel} =1/531.25 ns. Because 34/531.25 =64 ns, a group of three microwave pulses of 21 ns and a spacer of 1 ns together will exactly have a length such that $\phi''_{rel} = 2\pi \cdot 34$. By extending each single-qubit Clifford gate and each single-qubit gate from the $\mathcal{S}_1$ group to a time of 64 ns, they may be used in any combination

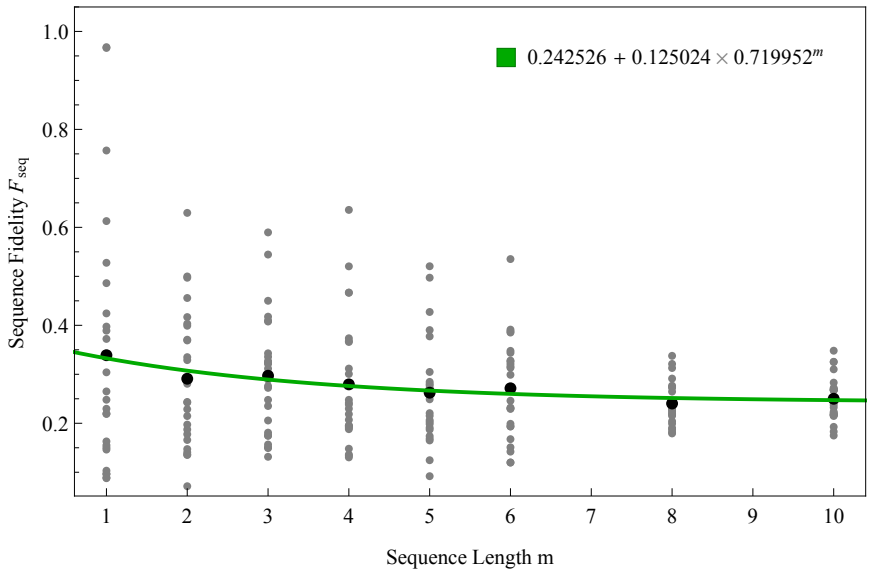

Figure 4.13.: Randomized benchmarking with the *i*SWAP gate. Decay of the sequence fidelity over sequence length m. An average gate fidelity of 85.99(519) % was determined from the fit (green), but since the fidelities are already at the beginning around the 25 %, this value has to be interpreted with caution.

with other two-qubit gates containing an *i*SWAP. The new CNOT gate is achieved by including one of the four pulses between and after the *i*SWAP gates (Fig. 4.12) inside the new *i*SWAP block and add another 1 ns spacer to the others.

This method implements scalable two-qubit Clifford gates containing the *i*SWAP gate. Unfortunately, we could not observe a typical exponentially decreasing sequence fidelity pattern when conducting a randomized benchmarking (Fig. 4.13), due to the achieved low sequence fidelities. A few of the sequence fidelities are higher compared to the others, which is justified by the occurrence of gates from the single-qubit class. Despite the 93.6 % fidelity measured with quantum process tomography, the most estimated sequence fidelities are below 40 %. Therefore, the error must lie in the timing between the different *i*SWAP pulses. A possible reason for these errors is the additional phase we get by the anticrossing of the $|ee\rangle$ state with the $|gf\rangle$ state, which is caused automatically when tuning the $g \leftrightarrow e$ transition frequency of qubit 1 to the $g \leftrightarrow e$ transition frequency of qubit 2. Another reason might be drifts of the relative phase between the two microwave generators used to drive qubit 1 and 2.

5. Conclusion

In this thesis, we have discussed randomized benchmarking for one and two-qubit gates. For single-qubit systems we introduced two different methods, the Pauli group based randomized benchmarking method proposed and demonstrated by Knill et al. [13] and the Clifford method by Magesan et al. [14, 15]. The first method allows an estimation of the average gate fidelity of a subgroup of the Clifford group, in contrast to the latter that offers an estimation over the whole Clifford group. We fitted a gate and time-independent as well as a gate and time-dependent model to the data obtained with the Clifford method. The predictions of both models fit our data well for average gate fidelities of 99.6465(277) % and 99.6871(324) % respectively. Since both models describe our data well, we concluded that the errors are mainly gate and time-independent. Furthermore, by assuming only gate errors due to dephasing, an upper limit of the average gate fidelity was provided in the presence of dephasing errors. With this simple mathematical approximation, we saw that the error is mostly caused by dephasing of the qubits.

In order to estimate the specific error of gates in the Clifford group, the interleaved randomized benchmarking, which is an expansion of the Clifford method was employed. To check the method and its functionality, a sensitivity and robustness test was implemented by adding an additional over-rotation error to the $(\pi/2)_x$ gate. As expected, the error for this gate increased as a function of the over-rotation angle, whereas the error of another gate was not affected. The same behaviour of the curves was also obtained by a simulation of the process. Furthermore, the errors of all individual Clifford gates were estimated. We found fluctuating errors in the 10^{-3} range. Those fluctuations may be explained by fluctuations in qubit frequency or other systematic errors.

The fidelity of two-qubit gates was estimated by using the Clifford group $\mathcal{C}_2$. We focused on the implementation with the controlled phase gate and the iSwap gate. Both of them were realized by tuning two qubit transitions to the same frequency with fast magnetic flux pulses. Besides a theoretical description, also important calibration steps and possible issues for both gates were discussed. An average gate fidelity of 92.089(1484) % of the Clifford group in terms of the cPhase gate was determined. The probability to be in the expected state of a two-qubit system was extracted by using a partially tomographic readout. By investigating the two-qubit interleaved randomized benchmarking with the cPhase we found a stable fidelity of 98.571(3115) % of the $\pi_x \otimes \pi_x$ gate and a heavily fluctuating fidelity outside the expected range of the C-NOT gate.

Acknowledgements

In the first place, I would like to thank Prof. Anderas Wallraff for the opportunity to conduct my Master's thesis in his team. Special thanks go to my supervisor Yves Salathé for the collaboration and his motivating and inspiring support. I would also like to thank Johannes Heinsoo and Markus Oppliger for their time to explain theoretical and practical aspects of the experimental work throughout this thesis. In general, my thanks go to the whole Qudev team and their former members for their technical fundamental framework, which made my thesis possible.

At this point I would also like to thank my parents. My studies would not have been possible, if I had not had their financial support.

A. Convention

A.1. Single Qubit

$$|g\rangle = \begin{pmatrix} 1 \\ 0 \end{pmatrix}, \qquad |e\rangle = \begin{pmatrix} 0 \\ 1 \end{pmatrix} \tag{A.1}$$

$$\sigma^0 = \begin{pmatrix} 1 & 0 \\ 0 & 1 \end{pmatrix}, \quad \sigma^x = \begin{pmatrix} 0 & 1 \\ 1 & 0 \end{pmatrix}, \quad \sigma^y = \begin{pmatrix} 0 & -i \\ i & 0 \end{pmatrix}, \quad \sigma^z = \begin{pmatrix} 1 & 0 \\ 0 & -1 \end{pmatrix} \tag{A.2}$$

A.2. Two Qubits

$$|gg\rangle = \begin{pmatrix} 1 \\ 0 \\ 0 \\ 0 \end{pmatrix}, \quad |ge\rangle = \begin{pmatrix} 0 \\ 1 \\ 0 \\ 0 \end{pmatrix}, \quad |eg\rangle = \begin{pmatrix} 0 \\ 0 \\ 1 \\ 0 \end{pmatrix}, \quad |ee\rangle = \begin{pmatrix} 0 \\ 0 \\ 0 \\ 1 \end{pmatrix}, \tag{A.3}$$

$$\begin{aligned} U_{cPhase} &= \begin{pmatrix} 1 & 0 & 0 & 0 \\ 0 & 1 & 0 & 0 \\ 0 & 0 & 1 & 0 \\ 0 & 0 & 0 & -1 \end{pmatrix} \qquad U_{C-NOT} = \begin{pmatrix} 1 & 0 & 0 & 0 \\ 0 & 1 & 0 & 0 \\ 0 & 0 & 0 & 1 \\ 0 & 0 & 1 & 0 \end{pmatrix} \\ U_{Swap} &= \begin{pmatrix} 1 & 0 & 0 & 0 \\ 0 & 0 & 1 & 0 \\ 0 & 1 & 0 & 0 \\ 0 & 0 & 0 & 1 \end{pmatrix} \qquad U_{iSwap} = \begin{pmatrix} 1 & 0 & 0 & 0 \\ 0 & 0 & i & 0 \\ 0 & i & 0 & 0 \\ 0 & 0 & 0 & 1 \end{pmatrix} \end{aligned} \tag{A.4}$$

B. The Single-Qubit Clifford Group

Pauli gates			
1	$\mathbb{1}$	$e^{-i\mathbb{1}\frac{\pi}{2}}$	$\begin{pmatrix} -i & 0 \\ 0 & -i \end{pmatrix}$
2	X	$e^{-i\sigma^x\frac{\pi}{2}}$	$\begin{pmatrix} 0 & -i \\ -i & 0 \end{pmatrix}$
3	Y	$e^{-i\sigma^y\frac{\pi}{2}}$	$\begin{pmatrix} 0 & -1 \\ 1 & 0 \end{pmatrix}$
4	Z	$e^{-i\sigma^x\frac{\pi}{2}} \cdot e^{-i\sigma^y\frac{\pi}{2}}$	$\begin{pmatrix} -i & 0 \\ 0 & i \end{pmatrix}$
$\pi/2$-Rotations			
5	$X/2$	$e^{-i\sigma^x\frac{\pi}{4}}$	$\frac{1}{\sqrt{2}}\begin{pmatrix} 1 & -i \\ -i & 1 \end{pmatrix}$
6	$Y/2$	$e^{-i\sigma^y\frac{\pi}{4}}$	$\frac{1}{\sqrt{2}}\begin{pmatrix} 1 & -1 \\ 1 & 1 \end{pmatrix}$
7	$Z/2$	$e^{-i\sigma^x\frac{\pi}{4}} \cdot e^{-i\sigma^y\frac{\pi}{4}} \cdot e^{i\sigma^x\frac{\pi}{4}}$	$\frac{1}{\sqrt{2}}\begin{pmatrix} 1-i & 0 \\ 0 & 1+i \end{pmatrix}$
8	$-X/2$	$e^{i\sigma^x\frac{\pi}{4}}$	$\frac{1}{\sqrt{2}}\begin{pmatrix} 1 & i \\ i & 1 \end{pmatrix}$
9	$-Y/2$	$e^{i\sigma^y\frac{\pi}{4}}$	$\frac{1}{\sqrt{2}}\begin{pmatrix} 1 & 1 \\ -1 & 1 \end{pmatrix}$
10	$-Z/2$	$e^{-i\sigma^x\frac{\pi}{4}} \cdot e^{i\sigma^y\frac{\pi}{4}} \cdot e^{i\sigma^x\frac{\pi}{4}}$	$\frac{1}{\sqrt{2}}\begin{pmatrix} 1+i & 0 \\ 0 & 1-i \end{pmatrix}$
$2\pi/3$-Rotations			
11	$X/2, Y/2$	$e^{-i\sigma^y\frac{\pi}{4}} \cdot e^{-i\sigma^x\frac{\pi}{4}}$	$\frac{1}{2}\begin{pmatrix} 1+i & -1-i \\ 1-i & 1-i \end{pmatrix}$
12	$X/2, -Y/2$	$e^{i\sigma^y\frac{\pi}{4}} \cdot e^{-i\sigma^x\frac{\pi}{4}}$	$\frac{1}{2}\begin{pmatrix} 1-i & 1-i \\ -1-i & 1+i \end{pmatrix}$

$2\pi/3$-Rotations			
13	$-X/2, Y/2$	$e^{-i\sigma^y\frac{\pi}{4}}\cdot e^{i\sigma^x\frac{\pi}{4}}$	$\frac{1}{2}\begin{pmatrix} 1-i & -1+i \\ 1+i & 1+i \end{pmatrix}$
14	$-X/2$, $-Y/2$	$e^{i\sigma^y\frac{\pi}{4}}\cdot e^{i\sigma^x\frac{\pi}{4}}$	$\frac{1}{2}\begin{pmatrix} 1+i & 1+i \\ -1+i & 1-i \end{pmatrix}$
15	$Y/2$, $X/2$	$e^{-i\sigma^x\frac{\pi}{4}}\cdot e^{-i\sigma^y\frac{\pi}{4}}$	$\frac{1}{2}\begin{pmatrix} 1-i & -1-i \\ 1-i & 1+i \end{pmatrix}$
16	$Y/2$, $-X/2$	$e^{i\sigma^x\frac{\pi}{4}}\cdot e^{-i\sigma^y\frac{\pi}{4}}$	$\frac{1}{2}\begin{pmatrix} 1+i & -1+i \\ 1+i & 1-i \end{pmatrix}$
17	$-Y/2$, $X/2$	$e^{-i\sigma^x\frac{\pi}{4}}\cdot e^{i\sigma^y\frac{\pi}{4}}$	$\frac{1}{2}\begin{pmatrix} 1+i & 1-i \\ -1-i & 1-i \end{pmatrix}$
18	$-Y/2$, $-X/2$	$e^{i\sigma^x\frac{\pi}{4}}\cdot e^{i\sigma^y\frac{\pi}{4}}$	$\frac{1}{2}\begin{pmatrix} 1-i & 1+i \\ -1+i & 1+i \end{pmatrix}$
Hadamard-Like			
19	X, $Y/2$	$e^{-i\sigma^y\frac{\pi}{4}}\cdot e^{-i\sigma^x\frac{\pi}{2}}$	$\frac{1}{\sqrt{2}}\begin{pmatrix} i & -i \\ -i & -i \end{pmatrix}$
20	X, $-Y/2$	$e^{i\sigma^y\frac{\pi}{4}}\cdot e^{-i\sigma^x\frac{\pi}{2}}$	$\frac{1}{\sqrt{2}}\begin{pmatrix} -i & -i \\ -i & i \end{pmatrix}$
21	Y, $X/2$	$e^{-i\sigma^x\frac{\pi}{4}}\cdot e^{-i\sigma^y\frac{\pi}{2}}$	$\frac{1}{\sqrt{2}}\begin{pmatrix} -i & -1 \\ 1 & i \end{pmatrix}$
22	Y, $-X/2$	$e^{i\sigma^x\frac{\pi}{4}}\cdot e^{-i\sigma^y\frac{\pi}{2}}$	$\frac{1}{\sqrt{2}}\begin{pmatrix} i & -1 \\ 1 & -i \end{pmatrix}$
23	$X/2$, $Y/2$, $X/2$	$e^{-i\sigma^x\frac{\pi}{4}}\cdot e^{-i\sigma^y\frac{\pi}{4}}\cdot e^{-i\sigma^x\frac{\pi}{4}}$	$\frac{1}{\sqrt{2}}\begin{pmatrix} 0 & -1-i \\ 1-i & 0 \end{pmatrix}$
24	$-X/2$, $Y/2$, $-X/2$	$e^{i\sigma^x\frac{\pi}{4}}\cdot e^{-i\sigma^y\frac{\pi}{4}}\cdot e^{i\sigma^x\frac{\pi}{4}}$	$\frac{1}{\sqrt{2}}\begin{pmatrix} 0 & -1+i \\ 1+i & 0 \end{pmatrix}$

C. The Two-Qubit Clifford Group

Clifford group class	Gate number	Gate	
single-qubit class (SQ)	1-24	$\mathcal{C}_1 \otimes \mathcal{C}_i$	$i \in (1, 2, 3, ..., 24)$
	25-48	$\mathcal{C}_2 \otimes \mathcal{C}_i$	$i \in (1, 2, 3, ..., 24)$
	49-72	$\mathcal{C}_3 \otimes \mathcal{C}_i$	$i \in (1, 2, 3, ..., 24)$
	...		...
	553-576	$\mathcal{C}_{24} \otimes \mathcal{C}_i$	$i \in (1, 2, 3, ..., 24)$
CNOT-like class	577-585	SQ 1, CNOT, $\mathcal{S}_i$	$i \in (1, 2, 3, ..., 9)$
	586-594	SQ 2, CNOT, $\mathcal{S}_i$	$i \in (1, 2, 3, ..., 9)$
	...		...
	5752-5760	SQ 576, CNOT, $\mathcal{S}_i$	$i \in (1, 2, 3, ..., 9)$
iSWAP-like class	5761-5769	SQ 1, iSWAP, $\mathcal{S}_i$	$i \in (1, 2, 3, ..., 9)$
	5770-5778	SQ 2, iSWAP, $\mathcal{S}_i$	$i \in (1, 2, 3, ..., 9)$
	...		...
	10936-10944	SQ 576, iSWAP, $\mathcal{S}_i$	$i \in (1, 2, 3, ..., 9)$
SWAP-like class	10945-11520	SQ i, SWAP	$i \in (1, 2, 3, ..., 576)$

List of Figures

Bibliography

[1] Turing, A. M. On Computable Numbers, with an Application to the Entscheidungsproblem. *Proc. London Math. Soc.* **s2-42**, 230–265 (1937). `http://plms.oxfordjournals.org/content/s2-42/1/230.full.pdf+html`. 6

[2] Moore. Cramming more components onto integrated circuits. *Electronics* **38** (1965). 6

[3] Nielsen, M. A. & Chuang, I. L. *Quantum Computation and Quantum Information* (Cambridge University Press, 2000). 6

[4] Wootters, W. K. & Zurek, W. H. A single quantum cannot be cloned. *Nature* **299**, 802–803 (1982). 6

[5] Shor, P. W. Algorithms for Quantum Computation: Discrete Logarithms and Factoring. In *Proceedings, 35th Annual Symposium on Foundations of Computer Science, Santa Fe*, 124 (IEEE Computer Society Press, 1994). 6

[6] Grover, L. K. A fast quantum mechanical algorithm for database search. In *Proceedings of the twenty-eighth annual ACM symposium on Theory of computing*, 212–219 (ACM, Philadelphia, Pennsylvania, United States, 1996). 6

[7] Knill, E. Quantum computing with realistically noisy devices. *Nature* **434**, 39–44 (2005). 7

[8] Chuang, I. L. & Nielsen, M. A. Prescription for experimental determination of the dynamics of a quantum black box. *J. Mod. Opt.* **44**, 2455–2467 (1997). 7

[9] Childs, A. M., Chuang, I. L. & Leung, D. W. Realization of quantum process tomography in NMR. *Phys. Rev. A* **64**, 012314– (2001). 7

[10] O'Brien, J. L. *et al.* Quantum Process Tomography of a Controlled-NOT Gate. *Phys. Rev. Lett.* **93**, 080502– (2004). 7

[11] Riebe, M. *et al.* Process Tomography of Ion Trap Quantum Gates. *Phys. Rev. Lett.* **97**, 220407 (2006). 7

[12] Chow, J. M. *et al.* Randomized Benchmarking and Process Tomography for Gate Errors in a Solid-State Qubit. *Phys. Rev. Lett.* **102**, 090502 (2009). 7, 26, 32

[13] Knill, E. *et al.* Randomized benchmarking of quantum gates. *Phys. Rev. A* **77**, 012307 (2008). 7, 14, 23, 25, 32, 65

[14] Magesan, E., Gambetta, J. M. & Emerson, J. Scalable and Robust Randomized Benchmarking of Quantum Processes. *Phys. Rev. Lett.* **106**, 180504 (2011). 7, 24, 27, 28, 29, 65

[15] Magesan, E., Gambetta, J. M. & Emerson, J. Characterizing quantum gates via randomized benchmarking. *Phys. Rev. A* **85**, 042311 (2012). 7, 27, 28, 29, 65

[16] Magesan, E. *et al.* Efficient Measurement of Quantum Gate Error by Interleaved Randomized Benchmarking. *Phys. Rev. Lett.* **109**, 080505 (2012). 7, 32, 33, 34

[17] Kelly, J. *et al.* Optimal Quantum Control Using Randomized Benchmarking. *Phys. Rev. Lett.* **112**, 240504 (2014). 7

[18] Sheldon, S. *et al.* Characterizing Errors on Qubit Operations via Iterative Randomized Benchmarking. *arXiv 1504.06597v1* (2015). 7

[19] Chasseur, T. & Wilhelm, F. K. A complete Randomized Benchmarking Protocol accounting for Leakage Errors. *ArXiv:1505.00580* (2015). `1505.00580`. 7

[20] Kimmel, S., Low, G. H. & Yoder, T. J. Robust Single-Qubit Process Calibration via Robust Phase Estimation. *arXiv:1502.02677* (2015). 7

[21] Girvin, S. M. Basic Concepts in Quantum Information. *arXiv:1302.5842* (2013). 8, 11, 14

[22] Josephson, B. D. The discovery of tunnelling supercurrents. *Rev. Mod. Phys.* **46**, 251–254 (1974). 10

[23] Bouchiat, V., Vion, D., Joyez, P., Esteve, D. & Devoret, M. H. Quantum coherence with a single Cooper pair. *Phys. Scr.* **T76**, 165–170 (1998). 11, 12

[24] Mooij, J. E. *et al.* Josephson Persistent-Current Qubit. *Science* **285**, 1036–1039 (1999). 11

[25] Martinis, J. M., Nam, S., Aumentado, J. & Urbina, C. Rabi oscillations in a large Josephson-junction qubit. *Phys. Rev. Lett.* **89**, 117901 (2002). 11

[26] Devoret, M. H. & Martinis, J. M. Quantum Entanglement and Information Processing. In Raimond, J.-M., Dalibard, J. & Esteve, D. (eds.) *Les Houches Session LXXIX*, 443–485 (Elsevier, 2003). 12

[27] Koch, J. *et al.* Charge-insensitive qubit design derived from the Cooper pair box. *Phys. Rev. A* **76**, 042319 (2007). 12, 14, 15, 17

[28] Blais, A., Huang, R.-S., Wallraff, A., Girvin, S. M. & Schoelkopf, R. J. Cavity quantum electrodynamics for superconducting electrical circuits: An architecture for quantum

computation. *Phys. Rev. A* **69**, 062320–14 (2004). 13

[29] Wallraff, A. *et al.* Strong coupling of a single photon to a superconducting qubit using circuit quantum electrodynamics. *Nature* **431**, 162–167 (2004). 13, 15

[30] Göppl, M. *et al.* Coplanar Waveguide Resonators for Circuit Quantum Electrodynamics. *J. Appl. Phys.* **104**, 113904 (2008). 14

[31] Jaynes, E. & Cummings, F. Comparison of quantum and semiclassical radiation theories with application to the beam maser. *Proceedings of the IEEE* **51**, 89–109 (1963). 15

[32] Haroche, S. & Raimond, J.-M. *Exploring the Quantum: Atoms, Cavities, and Photons* (Oxford University Press, New York, USA, 2006). 15

[33] Lamb, W. E. & Retherford, R. Fine Structure of the Hydrogen Atom by a Microwave Method. *Phys. Rev.* **72**, 241 (1947). 15

[34] Fragner, A. *et al.* Resolving Vacuum Fluctuations in an Electrical Circuit by Measuring the Lamb Shift. *Science* **322**, 1357–1360 (2008). `http://www.sciencemag.org/cgi/reprint/322/5906/1357.pdf`. 15

[35] Blais, A. *et al.* Quantum-information processing with circuit quantum electrodynamics. *Phys. Rev. A* **75**, 032329–21 (2007). 16, 40

[36] Motzoi, F., Gambetta, J. M., Rebentrost, P. & Wilhelm, F. K. Simple Pulses for Elimination of Leakage in Weakly Nonlinear Qubits. *Phys. Rev. Lett.* **103**, 110501 (2009). 17

[37] Clarke, J. & Wilhelm, F. K. Superconducting quantum bits. *Nature* **453**, 1031–1042 (2008). 17

[38] Salathé, Y. *et al.* Digital Quantum Simulation of Spin Models with Circuit Quantum Electrodynamics. *Phys. Rev. X* **5**, 021027 (2015). 18, 19

[39] Baur, M. *et al.* Benchmarking a Quantum Teleportation Protocol in Superconducting Circuits Using Tomography and an Entanglement Witness. *Phys. Rev. Lett.* **108**, 040502 (2012). 20, 40, 43

[40] Yurke, B. Squeezed-state generation using a Josephson parametric amplifier. *J. Opt. Soc. Am. B* **4**, 1551–1557 (1987). 20

[41] Castellanos-Beltran, M. A. & Lehnert, K. W. Widely tunable parametric amplifier based on a superconducting quantum interference device array resonator. *Appl. Phys. Lett.* **91**, 083509–3 (2007). 20

[42] Emerson, J., Alicki, R. & yczkowski, K. Scalable noise estimation with random unitary operators. *Journal of Optics B: Quantum and Semiclassical Optics* **7**, S347 (2005). 21, 22, 23

[43] Nielsen, M. A. A simple formula for the average gate fidelity of a quantum dynamical operation. *Phys. Lett. A* **303**, 249–252 (2002). 21

[44] Selinger, P. Generators and relations for n-qubit Clifford operators. *Logical Methods in Computer Science* **11** (2015). 23

[45] Steffen, L. *Quantum Teleportation and Efficient Process Verification with Superconducting Circuits*. Ph.D. thesis, ETH Zurich (2013). 26

[46] Ciorciaro, L. *Automatic Single Qubit Routines*. Master's thesis, ETH Zurich (2015). 26

[47] Chiorescu, I. *et al.* Coherent dynamics of a flux qubit coupled to a harmonic oscillator. *Nature* **431**, 159–162 (2004). 40

[48] Wallraff, A. *et al.* Sideband Transitions and Two-Tone Spectroscopy of a Superconducting Qubit Strongly Coupled to an On-Chip Cavity. *Phys. Rev. Lett.* **99**, 050501 (2007). 40

[49] Jeffrey, E. *et al.* Fast Accurate State Measurement with Superconducting Qubits. *Phys. Rev. Lett.* **112**, 190504 (2014). 40

[50] Majer, J. *et al.* Coupling superconducting qubits via a cavity bus. *Nature* **449**, 443–447 (2007). 41, 43

[51] Córcoles, A. D. *et al.* Process verification of two-qubit quantum gates by randomized benchmarking. *Phys. Rev. A* **87**, 030301 (2013). 41, 51, 53

[52] Barends, R. *et al.* Superconducting quantum circuits at the surface code threshold for fault tolerance. *Nature* **508**, 500–503 (2014). 41, 51, 53

[53] Vijay, R., Slichter, D. H. & Siddiqi, I. Observation of Quantum Jumps in a Superconducting Artificial Atom. *Phys. Rev. Lett.* **106**, 110502 (2011). 43

[54] Bianchetti, R. *et al.* Dynamics of dispersive single-qubit readout in circuit quantum electrodynamics. *Phys. Rev. A* **80**, 043840–7 (2009). 44

[55] Filipp, S. *et al.* Two-Qubit State Tomography Using a Joint Dispersive Readout. *Phys. Rev. Lett.* **102**, 200402 (2009). 44, 45

[56] Strauch, F. W. *et al.* Quantum Logic Gates for Coupled Superconducting Phase Qubits. *Phys. Rev. Lett.* **91**, 167005 (2003). 45, 46, 58

[57] DiCarlo, L. *et al.* Demonstration of two-qubit algorithms with a superconducting quantum processor. *Nature* **460**, 240–244 (2009). 46, 47

[58] Heinsoo, J. *Towards high fidelity two-qubit gates with superconducting qubits*. Master's thesis, ETH Zurich (2014). 60

[59] Nelder, J. A. & Mead, R. A Simplex Method for Function Minimization. *The Com-*

puter Journal **7**, 308–313 (1965). http://comjnl.oxfordjournals.org/content/7/4/308.full.pdf+html. 60

[60] Egger, D. J. & Wilhelm, F. K. Adaptive Hybrid Optimal Quantum Control for Imprecisely Characterized Systems. *Phys. Rev. Lett.* **112**, 240503 (2014). 60

[61] Schuch, N. & Siewert, J. Natural two-qubit gate for quantum computation using the XY interaction. *Phys. Rev. A* **67**, 032301 (2003). 63

ETH

Eidgenössische Technische Hochschule Zürich
Swiss Federal Institute of Technology Zurich

Declaration of originality

The signed declaration of originality is a component of every semester paper, Bachelor's thesis, Master's thesis and any other degree paper undertaken during the course of studies, including the respective electronic versions.

Lecturers may also require a declaration of originality for other written papers compiled for their courses.

I hereby confirm that I am the sole author of the written work here enclosed and that I have compiled it in my own words. Parts excepted are corrections of form and content by the supervisor.

Title of work (in block letters):

Randomized Benchmarking of Two-Qubit Gates

Authored by (in block letters):

For papers written by groups the names of all authors are required.

Name(s):	**First name(s):**
Haberthür	Samuel

With my signature I confirm that

- I have committed none of the forms of plagiarism described in the 'Citation etiquette' information sheet.
- I have documented all methods, data and processes truthfully.
- I have not manipulated any data.
- I have mentioned all persons who were significant facilitators of the work.

I am aware that the work may be screened electronically for plagiarism.

Place, date	**Signature(s)**
Zürich, 28.08.15	

For papers written by groups the names of all authors are required. Their signatures collectively guarantee the entire content of the written paper.